



Title	Creation of Plasmonic Energy Transfer Systems Enabling Extreme Light Confinement
Author(s)	及川, 隼平
Citation	北海道大学. 博士(理学) 甲第14456号
Issue Date	2021-03-25
DOI	10.14943/doctoral.k14456
Doc URL	http://hdl.handle.net/2115/84475
Type	theses (doctoral)
File Information	OIKAWA_Shunpei.pdf



[Instructions for use](#)

Creation of Plasmonic Energy Transfer

Systems Enabling Extreme Light

Confinement

極限光集約を可能とするプラズモニックエネルギー移動

システムの創出

Shunpei Oikawa

Graduate School of Chemical Sciences and Engineering

Hokkaido University

2021



Contents

Chapter 1 General introduction 1

- 1.1 Basic Concepts of Surface Plasmon Induced on Metal
 - 1.1.1 Surface Plasmon Polariton (SPP)
 - 1.1.2 Localized Surface Plasmon Resonance (LSPR)
 - 1.1.3 Dynamics of Surface Plasmon Resonance
- 1.2 Gap and Charge Transfer Plasmon of Metal Nanodimer
- 1.3 Enhanced Spontaneous Emission with Plasmon
- 1.4 Strong Light Matter Coupling
 - 1.4.1 Theoretical Description of Exciton Polariton
 - 1.4.2 Determination of Weak and Strong Coupling
 - 1.4.3 Decay Process of Exciton Polariton
- 1.5 Limitation of LSP
- 1.6 Coherent Plasmon Coupling in Periodic Metal Nano Arrays
- 1.7 Stimulated Emission via Plasmonic Crystals
- 1.8 Bose-Einstein Condensation with Strong Coupling Regime
- 1.9 Purpose of This Paper
- 1.10 References

Chapter 2 Improvement of the Light Condensation on Plasmonic Arrays via Low Temperature Annealing 42

- 2.1 Introduction
- 2.2 Experimental Method
 - 2.2.1 Angle-Resolved Nanosphere Lithography (AR-NSL)
 - 2.2.2 Electron Beam Lithography (EBL)
 - 2.2.3 Steady-State Extinction Measurements
 - 2.2.4 Surface Analysis
- 2.3 Results and Discussion
 - 2.3.1 Geometry and Extinction of Annealed Au Nanoprisms
 - 2.3.2 Time Dependent of Low Temperature Annealing
 - 2.3.3 XRD Measurement for Annealed Au Nanoprisms
 - 2.3.4 Cu Under Potential Deposition on Au Nanoprisms
 - 2.3.4 Improvement of Surface Lattice Resonance
- 2.4 Conclusion
- 2.5 References

Chapter 3 Electrochemical Structure Control for

Ultimate Light Confinement 63

- 3.1 Introduction
- 3.2 Experimental Method
 - 3.2.1 Sample Fabrication
 - 3.2.2 Electrochemical Extinction Measurements
 - 3.2.3 Electrochemical Dark-field Spectroscopic Measurements
 - 3.2.4 Electric Field Simulations of the Au Nanodisk Array
- 3.3 Results and Discussion
 - 3.3.1 Nanoscale Control of Au Nanoprisms Gap via Electrochemical Gold Dissolution
 - 3.3.2 Dark field imaging during electrochemical Au dissolution
 - 3.3.3 In situ Observations of Plasmonic Property Changes during Electrochemical
 - 3.3.4 Finite-difference time-domain calculations
 - 3.3.5 Long time excitation of higher order mode
 - 3.3.6 Photoelectron Emission Microscopic (PEEM) Measurement
 - 3.3.7 Monoatomic Control of Au nanodisk Arrays
- 3.4 Conclusion
- 3.5 References

Chapter 4 Enhanced Fluorescence via Bright and Dark SLR Modes

Supported by In- and Out-phase Coherent Coupling ... 96

- 4.1 Introduction
- 4.2 Experimental Method
 - 4.2.1 Sample Fabrication
 - 4.2.2 Angle-Resolved Extinction Measurement
 - 4.2.3 Fluorescence Measurement Set Up
 - 4.2.4 FDTD simulations for SLR modes
 - 4.2.5 Electrogenerated Chemiluminescence (ECL) measurement
- 4.3 Results and Discussion
 - 4.3.1 Confirmation of Surface Lattice Resonance
 - 4.3.2 Fluorescence Behavior Depending on Dye Concentration
 - 4.3.3 Periodic Dependence of Fluorescence via SLR
 - 4.3.4 FDTD Simulation for Dark and Bright SLR Modes
 - 4.3.5 Stimulated Fluorescence via Dark and Bright SLR Modes
 - 4.3.6 ECL through Dark and Bright SLR Modes
- 4.4 Conclusion
- 4.5 References

Chapter 5 Creation of Ultra-strong Light-Matter Coupling Regime

of Cyanine Dye Supported Plasmonic Crystal 120

- 5.1 Introduction
- 5.2 Experimental Method
 - 5.2.1 Preparation and Optical Analysis of Strong Coupling Regime
- 5.3 Results and Discussion
 - 5.3.1 Establishment of Strong Coupling Regime
 - 5.3.2 Ultra-Strong Coupling with Plasmonic Lattice Structure
- 5.4 Conclusion
- 5.5 References

Chapter 6 Energy Condensation into Defect Sites in Plasmonic Arrays

for Efficient Light Utilization 132

- 6.1 Introduction
- 6.2 Experimental Method
 - 6.2.1 Sample Fabrication
- 6.3 Results and Discussion
 - 6.3.1 Fluorescence on Au Nanodisk Arrays with Line Defects
 - 6.3.2 Emission Behavior Depending on Defects Size
 - 6.3.3 Light Condensation into Void Defects
- 6.4 Conclusion
- 6.5 References

General Conclusions 145

Acknowledgment

Chapter 1

General Introduction

Effective utilization of the light energy from sunlight is one of the very important issue for the energy problems. Especially, it can be said that the development of the technology for the effective utilization of the visible light would realize the sustainable society. The photochemical processes in optical devices are driven by the photoexcitation of matter. This excitation process allows us to use the light energy through photo-electron conversion or photon energy transfer process. The efficiency of the photoexcitation process is determined by the absorption cross section of the matters. For example, the absorption cross section of a typical molecule is about $1 \times 10^{-15} \text{ cm}^2$ which is quite small with respect to the size of light. Thus, it can be said that the key point for the effective use of light energy is developing the method to locally concentrate light into the nanospace and apply it to the matters with high efficiency. The plasmon phenomenon induced on metal nanostructures can efficiently concentrate the visible light energy in the nanoregion near the metal surface. Based on such characteristic, it is expected to improve the photoelectric conversion ability via localized light and to develop new optical properties. However, for conventional metal nanostructures, the application is limited due to the light energy loss derived from the structural inhomogeneity, electron bands of metal, and light scattering. In recent years, applications of metal dimers close to the quantum limit region ($<1 \text{ nm}$) and the periodic lattice structures have been proposed as the break through. Ultimate light condensation enabling the efficient light energy transfer to materials is expected by using the specific properties of these structures, such as the extreme light confinement ability, large

absorption cross section, and efficient light propagation ability. However, the visible light condensation efficiency is still insufficient due to restrictions such as the resolution of existing structural control technology and the delocalization of light due to the optical band. Therefore, the novel approach using plasmon materials and experimental guidelines are required to overcome these limitations.

1.1 Basic Concepts of Surface Plasmon

Surface plasmon resonance (SPR) is the collective oscillations of the conduction electrons in the surface of metal.¹ SPR frequency and its intensity strongly depend on the metal-size, shape, arrangement and composition, as well as the dielectric properties of the surrounding mediums.²⁻⁶ These specific optical responses serve as new optical technique such as sensors.

It is well known that SPR have two different forms: propagating surface plasmon polaritons (SPPs) and localized SPR (LSPR). SPPs are the propagating charge oscillations on the metal surface. Under normal incident light condition, SPPs cannot be excited due to the momentum mismatch between the light wavelength and the charge oscillation (the light momentum is reduced on metal due to the different refractive index). Thus, the momentum matching is required for the excitation of the SPPs. In order to do it, the prism or periodic metal nanostructures are often used. In contrast to SPPs, LSPR occurs when the dimensions of a metal nanostructure are less than the wavelength of the incident light, resulting in the collective confined oscillations of free electrons on the structure surface. The excitation of the SPPs or LSPRS can efficiently

concentrate the incident light energy, leading to the generation of the electromagnetic (EM) field, in the vicinity of the nanostructures. These localized EM field can be applied to various optical phenomena. In this chapter 1, the principle and characteristics of plasmons were explained, and then the importance of light confinement into a small space based on the example of light-matter interaction was introduced. Then a new design guideline for confining light could be proposed.

1.1.1 Surface Plasmon Polariton (SPP)

Under the light illumination onto a bulk metal, the free electrons in the metal are oscillated by the time-dependent force opposite to the time-dependent change in the electromagnetic field of the light (Fig. 1a). The electron oscillation is 180° against out of phase for light and dampened by Ohmic losses.⁷ Like all oscillators, this phenomenon can be regarded as a harmonic oscillator, known as the plasma frequency (ω_p) which is described as below;⁷

$$\omega_p = \sqrt{\frac{ne^2}{m_{eff}\epsilon_0}}$$

where the n , m_{eff} , are the density and the effective mass of the electron, respectively. Usually, almost all the free electrons in the bulk of the metal cannot be oscillated by a restoring force, so the mass is not depicted as a simple single spring model. Instead, the such oscillation can be recognized as the mass dragged in a viscous fluid and though as the assumption whether the electrons can respond quickly enough to the driving force of the incident field. If the light frequency is larger than the ω_p , the electrons will not

oscillate and the light will simply be transmitted or absorbed for the interband transitions.⁷ In contrast, when the light frequency is smaller than ω_p , the electrons will oscillate 180° out of phase for the incident light, resulting in a strong reflection.⁷ The combination of plasma frequency and interband transitions leads to the unique color of metal. Theoretically, this behavior is described by the real part of the dielectric constant (ϵ_{metal});⁸

$$\frac{\epsilon_{metal}}{\epsilon_0} = 1 - \left(\frac{\omega_p}{\omega}\right)^2$$

The real part of the dielectric constant become positive, resulting in light transmission in the case for the higher frequency of the incident light than ω_p .⁸ Contrary, the real part of the dielectric constant is negative, giving the light reflection with the case for the lower frequency of the incident light (Fig. 1a). Therefore, it can be said as that the dielectric constant determines the optical property of the bulk metal.

When the metal surface is irradiated with total reflected light using a prism or grating, the charge oscillations is not be induced at the surface, leading to the propagation of the charge waves, which is known as surface plasmon polariton (SPP) (Fig. 1b).^{9,10} The wavevector (depicts resonance condition) of SPP is given by below.^{9,10}

$$k_{SPP} = \frac{\omega}{c} \sqrt{\frac{\epsilon_{metal}\epsilon_{med}}{\epsilon_{metal} + \epsilon_{med}}}$$

which gives the dispersion curve for a SPP. The wavevector or momentum of the charge oscillation are always higher than that of the normal incident light.^{9,10} Therefore, SPP cannot be directly excited under the normal light irradiation without using a prism (Kretschmann system) or a metal grating, leading to the reduction of the momentum.⁹ The above equation gives the specific light irradiation angle for prism or grating to excite the SPP. Since the real part of the dielectric constant of metal is negative under

excitation of charge oscillation, resonance condition is simply depicted as below by cancelling the denominator.^{9,10}

$$\omega_{SPP} = \frac{\omega_p}{\sqrt{(1 + \epsilon_{med})}}$$

The narrow absorption and high angular specificity of the SPP allow excellent signal-to-noise ratio to be obtained for various SPP based sensors.⁹

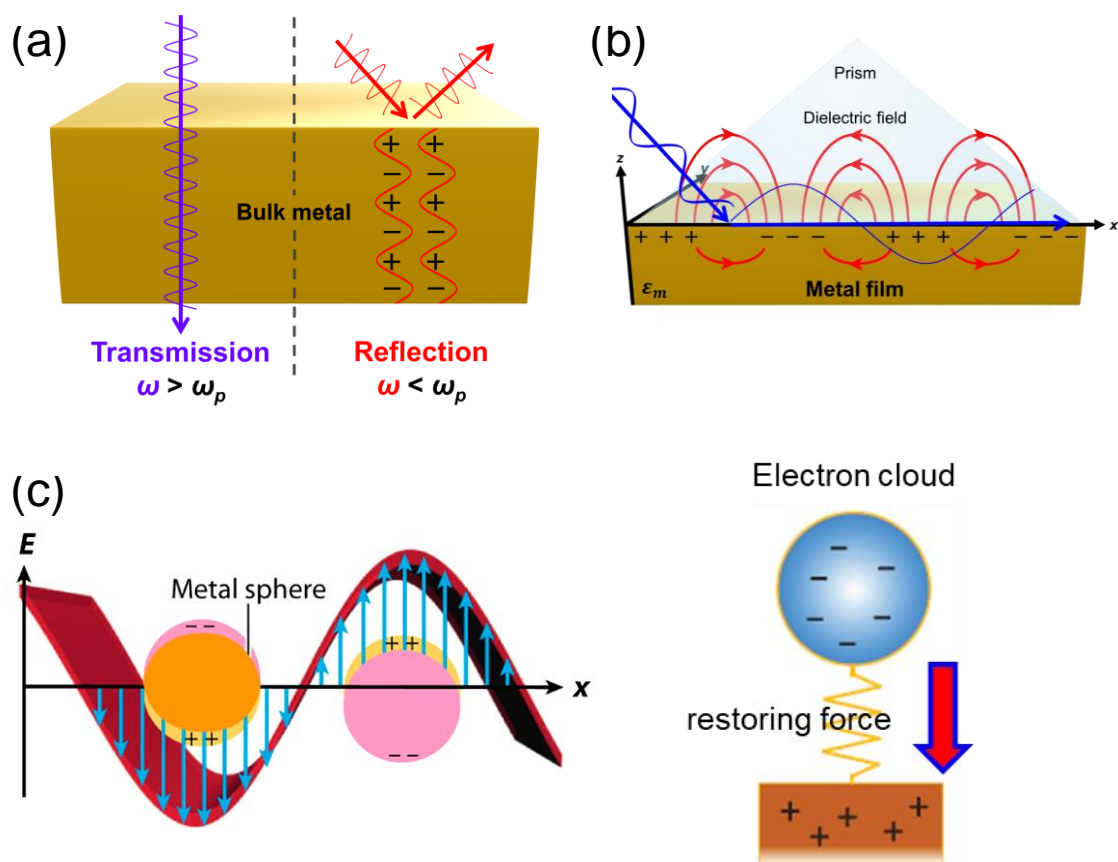


Figure 1-1. Various type of surface plasmon resonance (SPR). (a) The plasma frequency of a metal describes the limitation frequency below which the conduction electrons oscillate in the incident field. Light is transmitted when it is higher than the plasma frequency and scattered when it is lower than the plasma frequency. (b) On a 2D surface, electron oscillations lead to propagating charge waves known as surface plasmon polaritons (SPPs). These oscillations are coupled to an electromagnetic field which propagates along the interface excited by using prism and with amplitude that exponentially decreases away from the interface. (c) Localized surface plasmon resonance exists when the metal nanoparticle is smaller than the incident wavelength, making the electron oscillations in phase.^{9,10}

1.1.2 Localized Surface Plasmon Resonance (LSPR)

The general optical properties of metal nanoparticle (NP) significantly differ from those for bulk metals. When the metal size is much smaller than incident light, generally less than 200 nm, the incident electromagnetic field will be constant for the whole metal nanoparticle. The displacement of the electron density is constant and receives a strong restoring force from the positive ion core background, leading to the harmonic oscillation parallel to the incident polarization of free electrons.¹¹ This phenomenon is known as localized surface plasmon (LSP) because the electron oscillation is distributed over the whole nanoparticle.¹¹ The exact conditions for LSP for a nanosphere can be led by the Mie theory (quasistatic approximation) and simple harmonic oscillation model.¹²⁻¹⁴ The charge distortion of free electrons can be expressed using the metal polarizability^{15,16}

$$\alpha(\lambda) = 3\varepsilon_{med}V_{NP} \frac{\varepsilon_{metal}(\lambda) - \varepsilon_{med}(\lambda)}{\varepsilon_{metal}(\lambda) + \chi\varepsilon_{med}(\lambda)}$$

where λ and ε_{med} are the incident light wavelength and the dielectric constant of the non-absorbing ($\text{Im}[\varepsilon_{med}] = 0$) surrounding medium, respectively while the V_{NP} , χ , and ε_{metal} are the metal nanoparticle volume, the geometrical factor (i.e. $\chi = 2$ in a sphere), and are the dielectric function of metal, respectively. The ε_{metal} is dependent on the wavelength (λ) as described below.^{17,18}

$$\varepsilon_{metal}(\lambda) = \text{Re}[\varepsilon_{metal}(\lambda)] + i \text{Im}[\varepsilon_{metal}(\lambda)]$$

From the above two equations, the extinction (absorption + scattering) cross section is expressed as follow:^{11,37}

$$\sigma_{ext} = \frac{18\pi[\varepsilon_{med}(\lambda)]^{3/2}}{\lambda} V_{NP} \frac{\text{Im}[\varepsilon_{metal}(\lambda)]}{[\text{Re}[\varepsilon_{metal}(\lambda)] + 2\varepsilon_{med}(\lambda)]^2 + \text{Im}[\varepsilon_{metal}(\lambda)]^2}$$

Similar to SPP character, the resonance condition of LSP (LSPR) follows below equation.

$$\omega_{LSPR} = \frac{\omega_P}{\sqrt{(1+2\varepsilon_{med})}}, \quad (\text{Re}[\varepsilon_{metal}(\lambda)] \approx -\chi\varepsilon_{med}(\lambda))$$

which are strongly depending on both the local dielectric environment and nanoparticle geometry. The coherent oscillations of the electrons make the absorption and scattering cross-section at resonance several orders of magnitude larger than the physical size of the nanoparticle given by $V=4/3\pi R^3$.

It is well known that the lifetime of plasmon excitation originates from the various type of energy losses.^{18,19} The real part of dielectric function ($\text{Re}[\varepsilon]$) describes the resonance frequency and absorption of a plasmon resonance wavelength while the imaginary part of that ($\text{Im}[\varepsilon]$) is correlated with its energy loss. A lot of processes are related with the energy loss such as radiative damping, structural imperfection and metal heating losses.^{18,19} In the case for the conventional noble metals such as gold (Au), the dominant energy loss process is derived from the intraband transition ($5d \rightarrow 6s-6p$).^{18,19} Since the LSPR excitation triggers the electron-hole pair generation at the same time, the electron-electron scattering rate is greatly increased, leading to the increase of the dephasing rate. Despite this character, the Au is commonly used because of its higher biocompatibility, chemical stability, and broad absorption especially in the vis–near infrared wavelength region.^{20,21}

1.1.3 Dynamics of Surface Plasmon Resonance

The plasmon bandwidth is associated to the dephasing time of the coherent electron oscillation, with larger bandwidth corresponding to faster damping of coherence and low quality factor.^{15,22,23} Typical electron dephasing time (i.g. metal nanoparticles) is around 2–50 fs depending on the particle geometry and environment.^{15,22,23} The SPR band width is related with a radiative term which is proportional to the radiative decay rate Γ_r (essentially producing scattered radiation) while a non-radiative term depends on the electronic relaxation processes Γ_{nr} (essentially producing heat).^{15,22,24} The total relaxation rate Γ of SPR as a harmonic oscillation can be expressed as¹⁴

$$\Gamma = \Gamma_{nr} + \omega^2 \Gamma_r$$

Since Γ_r is multiplied by the frequency ω^2 , it means that the radiative dephasing effect decreases with lower frequency.

Since the term of Γ_r is associated with dipole radiation, it can be fully explained by the classic electrodynamics theory such as the Mie model. The relative value between the two terms in equation determines the relation between light scattering and absorption. The relative value of the two decay processes strongly depends on the size, shape and/or surrounding environment. The radiative decay contributes significantly with increasing nanoparticle size (over 20 nm).²⁵⁻²⁷

Several groups have investigated the non-radiative processes of SPR using ultrafast spectroscopy measurements.^{22,23,28,29} There are several processes contributing to Γ_{nr} , such as the electron-electron scattering ($1/t_{e-e}$), electron-photon scattering ($1/t_{e-ph}$), electron-defect ($1/t_{e-d}$) scattering and surface effects ($1/t_s$).^{22,23} Note that, when the metal

surface is polycrystalline or highly defective, the dumping frequency also increases, resulting in the broader SPR band.³⁰ According to Matthiessen law, all these contributions can be expressed as^{22,23}

$$\Gamma_{nr} = \frac{1}{t_{e-e}} + \frac{1}{t_{e-ph}} + \frac{1}{t_{e-d}} + \frac{1}{t_s}$$

Each scattering process can be treated as a kind of Landau damping mechanism. In Landau damping mechanism, plasmon energy is transferred into lower-energy single or multiple electron–hole pair excitations with a time scale of 1–100 fs.^{31,32} The electron–hole pairs excitation can be either intraband or interband shown in figure 2a.³²⁻³⁴ In the case for Au NPs, due to the energy overlap between plasmon absorption band and interband transitions, the interband excitation corresponding to the excitation of one electron and hole in the conduction band and in the lower-lying d-band, respectively, has a remarkable contribution to the electron–electron relaxation rate,³⁴ resulting in lower quality factor of Au than that of Ag.^{18,19,35} After the formation of electron–hole pairs by Landau damping, the electron–electron scattering in the conduction band takes place with a time scale of ~500 fs, leading to the electron thermalization.^{22,23,32,34} In this way, electron energies are rearranged from non-equilibrium to the quasi-equilibrium Fermi–Dirac distribution, corresponding to the thermal energy increments and the absorbed photon energy.²² Then, in 1–5 ps scale, electron–phonon scattering leads to the thermalization of the electronic bath with the lattice.^{22,23} The latter process involves phonon–phonon interaction between the lattice and the surrounding medium, with a time scale of hundreds of picoseconds up to nanoseconds.^{22,23} These energy scattering processes are increased by the crystalline boundaries of polycrystals of metals. Therefore, it is known that the structure produced by the top-down method has a large energy dissipation, and an improvement method is required.

1.2 Gap and Charge Transfer Plasmon of Metal Nanodimer

Increasing the localized field beyond the limit of a single particle is very important for the effective use of light. A powerful amplified electromagnetic field for hybrid plasmons can be obtained using a simpler system. The dimer plasmon mode provide the enhanced electromagnetic field formed at the gap, where its enhancement reaches up to $\sim 10^6$ with gap distance of around 1 nm, leading to various optical phenomena. In addition, dimeric plasmons excite various plasmon modes depending on the gap distance. Bonding dipole plasmon (BDP) is induced by the binding of dipoles when there are gaps of several nanometers between the particles. The photoelectric field in the gap formed by BDP is very strong. On the other hand, when the dimer is covered with a conduction path, the charge transfer plasmon (CTP) due to the transfer of electrons is excited. In general, the electromagnetic field strength of CTP mode is several orders smaller than that of BDP, thus it can be expected that BDP have the significant effect against the surrounding matters rather than CTP.⁵⁰

When the interparticle distance down to sub-nanometer scale which allows the electron tunneling, quadrupolar or higher order plasmon modes can be excited by the localized dipole interactions at the local surface area of the particles. A series of BDP transitions to the higher-order plasmons depending on gap distance have been accurately represented by the quantum-corrected model (QCM).⁵³ According to theoretical studies, the higher order plasmon induced on the dimer with sub-nanometer gap is not a highly symmetric quadrupole induced in a single particle, but is a new hybridized mode due to a mixture of dipoles and quadrupoles. This new hybrid plasmon is called as bonding quadrupolar plasmon (BQP).^{38,39,53} Since the average dipole

momentum of whole nanoparticles is quite small, BQP is regarded as the dark mode, leading to dramatically extended plasmon life time due to the suppression of the radiative loss.³⁹ Metal dimer structures with sub-nanometer gaps can increase the light-molecular interaction significantly increase sensor sensitivity due to the formation of enhanced electromagnetic fields as well as BDP mode. Therefore, it can be said that it is a very

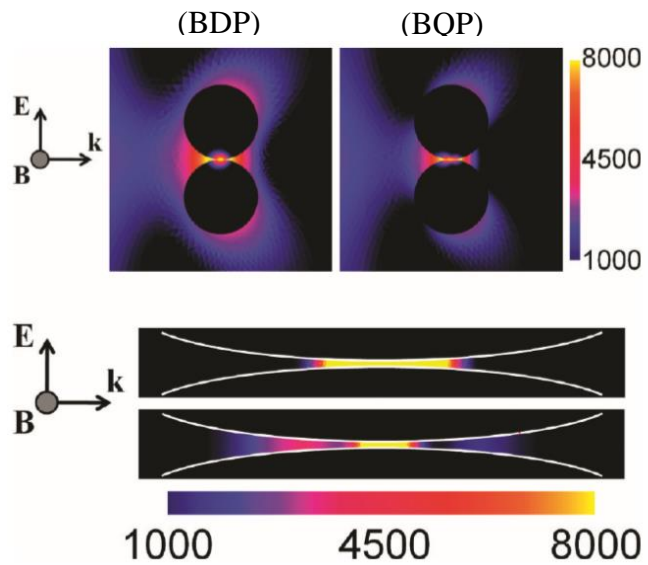


Figure 1-2. (top) FEM calculated $|E|^2/|E_0|^2$ contour profiles at 1.7 eV (714 nm) and 2.1 eV (592 nm) for gold dimers that are 50 nm in diameter with a 0.25 nm separation. (bottom) Contour profiles showing the junction regions of the top figures (the top and bottom enlargements correspond to the left and right images, respectively). The internal fields were set to zero in the lower plots for clarity.³⁹

effective material for effective light usage. However, since it is very difficult to control the gap distance with the sub-nanometer level, there are still few reports on the enhancement of the optical response by BQP. And also, the results in them are not beyond the theory.

1.3 Enhanced Spontaneous Emission with Plasmon

Basically, the enhanced fluorescence of molecule (: fluorophore) via plasmons is occurred from an energy transfer process between metal and fluorophores which is a radiative coherent process at the nearfield. These processes are induced by dipole–dipole interactions at the interface with the specific separation distance.

Firstly, if the distance between metal surface and the fluorophores are within 10 nm, the non-radiative local field of one dipole can excite the other one via dipole-dipole interaction. This is known as Förster resonance energy transfer (FRET) as follows:

$$\text{Efficiency of FRET} = \frac{1}{1 + (R/R_0)^6}$$

The efficiency of energy transfer in FRET is dependent on two factors.⁹⁴ The most obvious factor is the separation distance, R , which decays as $1/R^6$ because each dipole has a $1/R^3$ near field. The distance dependent behavior is scaled by the factor R_0 , which depends on the spectral overlap between the emission of the donor's excited state and the acceptor's ground state absorption. The value of R_0 is usually in the range of 3–8 nm in FRET between plasmon and fluorophore. The FRET process is very efficient, approaching 100% for $R < R_0$ in the presence of plasmon, because of the amplified local field and large absorption cross-section inherent to LSPR. FRET can occur from plasmons to fluorophores or from fluorophores to plasmons, inducing quenching as well as fluorescence enhancement.

Secondly, the strong near field of plasmon can enhance the absorption and/or spontaneous emission rate of the fluorophore through the coherent coupling process.⁹⁵ This process known as the Purcell effect comes from the modulation of vacuum

fluctuations by a defined optical mode. The Purcell effect can be easily understood as follows, if a radiative dipole is placed in a resonant cavity, such as Fabry–Pérot interferometer, the emission intensity will be amplified on-resonance and quenched off-resonance when compared to the case without a resonant cavity. This is because the cavity modifies the local density of optical states (LDOS) and transition rate (Γ) between two states of molecules as follows⁹⁵

$$\rho_{LDOS}(\omega) \sim |E_{loc}(\omega)|^2$$

$$\Gamma = \frac{2\pi}{\hbar} |\vec{\mu}|^2 \rho_{LDOS}(\omega)$$

where $|E_{loc}(\omega)|^2$ is the local electromagnetic field of the cavity normalized by incident intensity, and $\vec{\mu}$ is the transition dipole moment between two states. In air, the LDOS is almost constant and the dipole radiates at all emission energies to random space. In the cavity, the LDOS shows the maximum peak at the resonance wavelength of cavity, and the dipole can emit into this mode with a higher rate than that in air. Then, the cavity can re-radiate the transferred energy, resulting in an overall enhancement of the dipole's emission. As described above, the plasmon has enhanced local field $|E_{loc}(\omega)|^2$ stronger than the light in free space, leading to the amplification of the LDOS compared to vacuum, and acts like a resonant cavity against the fluorophore. If the plasmon's absorption or scattering spectrally overlaps with the fluorophore's emission, the fluorophore's emission rate will be enhanced due to the change in the LDOS. The plasmon can either absorb the transferred energy or re-radiate it as the scatter, resulting in a quenching or enhancement of the fluorophore's emission intensity as a same mean as the FRET. For a plasmonic dipole, the LDOS goes roughly as $1/R^3$,

so the Purcell effect is usually seen outside the FRET range (~ 10 nm where coupling goes as $1/R^6$).⁹⁶⁻⁹⁸

The spectral overlap between the plasmon and the fluorophore determines whether FRET or the Purcell effect occur and whether these mechanisms lead to an enhancement or quenching of the fluorophore emission. If the frequency of plasmon resonance overlaps with that of fluorophore's absorption, the excitation rate of the fluorophore will be enhanced from its free space value.⁹⁶⁻¹⁰³ In the case for metal nanoparticles larger than 20 nm which shows mainly scattering, the emission amplification will be possible through both FRET at close distances (~ 10 nm) and the Purcell effect with longer distances (~ 10 – 50 nm).⁹⁶⁻¹⁰³ Note that the Purcell enhancement for the plasmon's radiation is usually negligible because the LDOS for the fluorophore is negligible. If a few emissions from plasmon were observed, that process is primarily dominated by FRET at distances of a few nanometers.⁹⁷

If the plasmon resonance frequency was overlapped with that of fluorophore's emission, an enhancement or quenching of the emission intensity is possible.⁹⁵⁻¹⁰³ If the fluorophore is within a few nanometers of the plasmon, its emission will be quenched by FRET into the plasmon. Although the plasmon could re-radiate this energy and possibly enhance the emission, the near field of the fluorophores also excites higher order modes in the plasmon which cannot re-radiate into the far field, leading to an overall quenching at the separation distances of a few nanometers. At distances where FRET can be negligible, a strong Purcell enhancement will be triggered because of the enhanced LDOS of the plasmonic field compared to the free space. This will lead to an increase of the radiative rate of the fluorophore, and if the plasmon can scatter the light more efficiently than the absorption, leading to drastically fluorescence emission

enhancement. It should be noted that, when the system is excited with pumping light which can induce the population inversion of fluorophores, stimulated emission could occur due to the emission rate increments.

1.4 Strong Light Matter Coupling

Until the beginning of the 20th century, light and matter have been treated as different ways. The development of quantum mechanics has enabled the theoretical description of the interaction between light-quanta and matter.¹²⁵ These theoretical studies have revealed that two types of light-matter interactions can be occurred. One can find the dramatically modification of the radiative decay of fluorophores in the vicinity of a metallic surface¹²⁶ due to the Purcell effect (see section 1.5 and 1.6).¹⁰⁵ This phenomenon can be affected by the surrounding electric environment, and can modulate only the radiative rate constants. Such system is called as weak coupling regime. If the light-matter interaction became so large that the perturbation theory of quantum energy cannot be ignored, a new hybrid state could form between light and matter. Such system is called as strong coupling regime, resulting in the modulation of both the radiative decay rates and the energy level. The first experimental demonstration of strong photon–exciton coupling has been reported by Yakovlev *et al.* in 1975.¹²⁷ Then, Likewise *et al.* have reported the exciton–surface plasmon strong coupling of Langmuir–Blodgett monolayer assemblies on a silver surface in 1982.¹²⁸

1.4.1 Theoretical Description of Exciton Polariton

The theoretical description of light-matter interactions was firstly provided by Jaynes and Cummings.¹²⁹ Then, the coupling with surface plasmons has been described by Agranovich and Malshukov.¹³⁰ In the most common and simple cavity quantum electrodynamics model of two-level system, the strong coupling system is described by the well-known Jaynes–Cummings Hamiltonian¹²⁹ which considers the system as the sum of the molecules, the electromagnetic field, and the molecule–field interaction within the rotating frame approximation¹²⁹

$$\begin{aligned}\hat{H}_{JC} &= \hat{H}_{mol} + \hat{H}_{cav} + \hat{H}_{incident} \\ &= \frac{1}{2} \hbar \omega \hat{\sigma}_z + \hbar \omega_c \left(\hat{a}^\dagger \hat{a} + \frac{1}{2} \right) + \hbar g_0 (\hat{a}^\dagger \hat{\sigma} + \hat{a} \hat{\sigma}^\dagger)\end{aligned}$$

where $\hat{\sigma}_z$, $\hat{\sigma}$ and $\hat{\sigma}^\dagger$ are Pauli matrices for inversion, raising and lowering, respectively. The \hat{a} and \hat{a}^\dagger are creation and annihilation operators for the field mode, and ω and ω_c are the transition frequencies of the molecule and the cavity, respectively. The g_0 is the magnitude of the light–matter coupling strength. In the interaction of the Hamiltonian, the terms $\hat{a}^\dagger \hat{\sigma}$ correspond to the transition from the ground state of the molecule to an excited state, simultaneously annihilating a photon in the cavity ($\hat{a} \hat{\sigma}^\dagger$ is the reverse process). This Hamiltonian can be diagonalized via the Hopfield–Bogoliubov method,¹³¹ leading to the formation of the two eigenstates in the system. The two eigenstates are linear combinations of light and matter such as molecular bonding, also called exciton polaritons. These states are given by

$$\begin{cases} |UP\rangle = \alpha |e, 0\rangle + \beta |g, 1\rangle \\ |LP\rangle = \beta |e, 0\rangle - \alpha |g, 1\rangle \end{cases}$$

where $|g\rangle$ and $|e\rangle$ represent the ground and excited state of the molecule, respectively. The $|0$ and $|1\rangle$ are the index of number of photons. At the resonance condition, i.e.

the transition frequency of the molecule matches the frequency of the cavity, the polariton is a hybrid state of half-light and half-matter. The energy difference between the upper and lower polariton is called the vacuum Rabi-splitting $\hbar\Omega_R$. It can be expressed as a function of coupling strength:

$$\hbar\Omega_R = 2\hbar g = 2d\sqrt{N} \sqrt{\frac{\hbar\omega_c}{2\varepsilon_0 v}}$$

Dealing with one exciton (E_{mol}) and one cavity photon (E_c), the coupling is described by a 2×2 matrix Hamiltonian¹³²

$$\begin{pmatrix} E_c & \frac{\hbar\Omega_R}{2} \\ \frac{\hbar\Omega_R}{2} & E_{mol} \end{pmatrix} \begin{pmatrix} \alpha \\ \beta \end{pmatrix} = E \begin{pmatrix} \alpha \\ \beta \end{pmatrix}$$

Diagonalization of this Hamiltonian leads to the eigenvalues of the Hamiltonian, which represent the two polariton states.

$$E_{\pm} = \frac{E_c + E_{mol}}{2} \pm \sqrt{(\hbar\Omega_R)^2 + (E_{mol} - E_c)^2}$$

Basically, the exciton energy is independent from the wavevector, whereas the cavity photon (such as Fabry-Perot resonator) has the in-plane dispersion as below:

$$E_c = \frac{\hbar c}{n_c} \sqrt{\left(\frac{m\pi}{L_c}\right)^2 + \left(\frac{2\pi}{\lambda}\right)^2 \sin^2\theta}$$

Thus, the resulting exciton polaritons also show strong in-plane dispersion. This strong angle dependence of the cavity implies that one can tune the resonance energy by simply varying the incident angle. From above eigenvectors, it is possible to extract the ratio between the optical and material characters of the polaritons, the Hopfield coefficient,¹³¹ defined as $|\alpha|^2$ and $|\beta|^2$.

$$|\alpha|^2 = \frac{1}{2} \left(1 + \frac{E_{mol} - E_c}{\sqrt{(E_{mol} - E_c)^2 + 4g^2}} \right)$$

$$|\beta|^2 = \frac{1}{2} \left(1 - \frac{E_{mol} - E_c}{\sqrt{(E_{mol} - E_c)^2 + 4g^2}} \right)$$

Note, these equations can be extended to an $N \times N$ matrix to include molecular transitions with the Holstein–Primakoff Hamiltonian.¹³³ In this case, coupling strength (g) is represented as $g_0\sqrt{N}$. Thus, the molecular concentration in the field volume is quite important for achieving a large coupling strength.

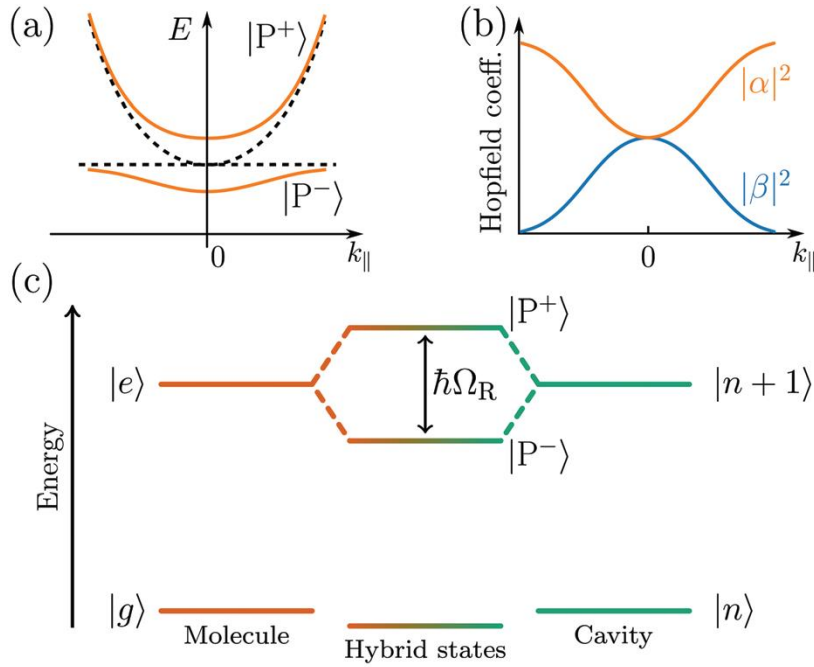


Figure 1-3. Polariton dispersion at resonance and (b) corresponding Hopfield coefficients, where $|\alpha|^2 + |\beta|^2 = 1$. (c) Jablonski diagram of a coupled molecule–cavity (electronic or vibrational transition) system showing the new hybrid polaritonic states with Rabi splitting $\hbar\Omega_R$.¹³⁵

1.4.2 Determination of Weak and Strong Coupling

The Jaynes-Cummings model¹²⁹ does not clearly illustrate the transition from weak coupling to strong coupling. In order to understand the state transition, it is necessary to interpret it from a different point of view. Under the resonance condition, the relative strength of the coupling is governed by three parameters: the photon decay rate of the cavity (κ), the molecule (γ), and the coupling strength (g). These three parameters define the dynamics of the system in the time domain. With the much smaller g than κ and γ , the system is weak coupling regime. On the other hand, when g becomes much larger than κ and γ , the strong coupling regime appears. In the strong coupling regime, the light-matter interaction is faster than dissipation processes. Therefore, the molecule interacts coherently with the cavity and can emit and re-absorb cavity photons several times before the cavity photon is lost. In other words, photon energy is delocalized in the system. Both κ and γ are related to the linewidth of the cavity and the molecular absorption band, respectively. Strong coupling occurs when the splitting (at resonance) is larger than the transmission linewidths, resulting in $2g > (\kappa + \gamma) / 2$.^{64,65} The transition between weak and strong coupling occurs when both polaritonic branches are spectroscopically resolved. In short, when the splitting energy (Ω_R) must be larger than the full width at half maximum (FWHM) of the bare molecule absorption ($\Delta\omega_{mol}$) and the cavity mode ($\Delta\omega_c$).

$$\Omega_R > \frac{\Delta\omega_c + \Delta\omega_{mol}}{2}$$

1.4.3 Decay Process of Exciton Polariton

In the strong coupling regime, N molecules and one cavity mode hybridize, and new hybrid states of $N+1$ are formed including upper and lower polaritons.¹⁴⁹ The other $N-1$ states are optically inactive states (dark states) located at around E_{mol} which are expressed as the exciton reservoir or exciton bath. These dark states have an

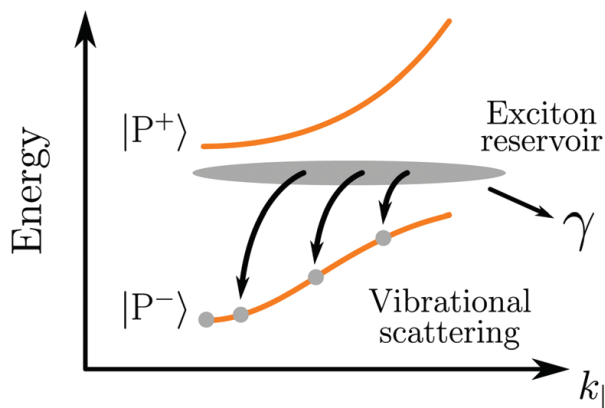


Figure 1-4. Vibrationally assisted relaxation processes from the exciton reservoir to the lower polaritonic branch. γ represents the dissipation of energy from the exciton to the environment (exciton decay, bimolecular quenching, etc.).

important effect on the relaxation pathways in strong coupling system. The number of states ($N-1$) in the dark exciton reservoir is larger than in the upper and lower polaritons. Therefore, the transition from the upper polariton is fast, while the transition to the lower polariton is slow.¹⁵⁰ After initial excitation to the upper polariton, exciton polariton relaxes to the exciton reservoir at the time scale of 150 fs. On the other hand, since there is only one lower polariton state, the relaxation rate from the exciton reservoir is much slower than the rate of emission from the lower polariton.¹⁵¹ Thus, the polariton lifetime is dominated by the rate of relaxation from the exciton reservoir down to the lower polariton.^{152,153}

1.5 Limitation of LSP

The optical phenomena introduced so far are supported by a strong localized field and coherent ability. The index of the LSP intensity can be quantified by the quality factor Q_{LSP} as same as the case for the micro cavity like Fabry-Perot resonator. The expression of quality factor differs depending on the specific metal geometry. However, under the condition that the particle size is sufficiently smaller than the incident wavelength, Q_{SPR} can be expressed as:

$$Q_{LSP}(\lambda) = -\frac{\text{Re}[\varepsilon_{metal}(\lambda)]}{\text{Im}[\varepsilon_{metal}(\lambda)]}$$

According to the above equation, The LSP quality factor is determined only by the complex dielectric functions of the metal, not dependent on the shape or the surrounding mediums. Note that the above equation is only used for the specific particles placed in a uniform electrostatic field space. However, generally speaking, the resonance frequency of plasmons is sensitively influenced by the geometry and/or the surrounding environment.^{18,19} Currently, the resonance frequency of plasmons is evaluated through a simple mathematical analysis on the peak indicated by the Lorentz function. The new quality factor is defined as the whole energy E stored in an oscillator, divided by the energy dissipated per radian. It then follows from simple wave-equation that the quality factor can be described as:

$$Q_{LSP}(\lambda) = \frac{E}{\frac{1}{\lambda} \frac{dE}{dt}} = \frac{\lambda}{2\gamma} \approx \frac{E_{LSP}(\lambda)}{\Gamma}$$

where E_{LSP} represents the SPR peak energy and Γ is the full-width of the plasmon peak at half its maximum amplitude. A higher quality factor representing a sharper resonance is often desirable because of the higher optical extinction and

stronger local electromagnetic field enhancement. The localized surface plasmons show generally broader spectral width (fwhm: >100nm) when compared to propagating surface plasmons (fwhm: ~50nm). This low quality factor as a cavity significantly limits the potential applications of LSP such as high sensitive plasmon sensor, chemical reaction, or lasing action which requires the high coherence property. In the past several ten years, improving the LSP's quality factor has been basically expected from the appropriate engineering of the shape and size of nanostructure fabrications. However, a lot of studies involving various geometries, including nanotriangles,^{54,55} nanorods,⁵⁶ nanostars,^{57,58} and nanocrosses,⁵⁹ have demonstrated the remarkable effect to narrow the LSP band depending on these particles. However in addition to this essential factor, typical LSP is broader than the prediction from this simple formula owing to large radiative loss and non-radiative damping. As a result, LSP have low quality factors around 10, which is too below to use in many photovoltaic devices. However, the spectral width and quality factor can be improved when nanoparticles are arranged in periodic array.

1.6 Coherent Plasmon Coupling in Periodic Metal Nano Arrays

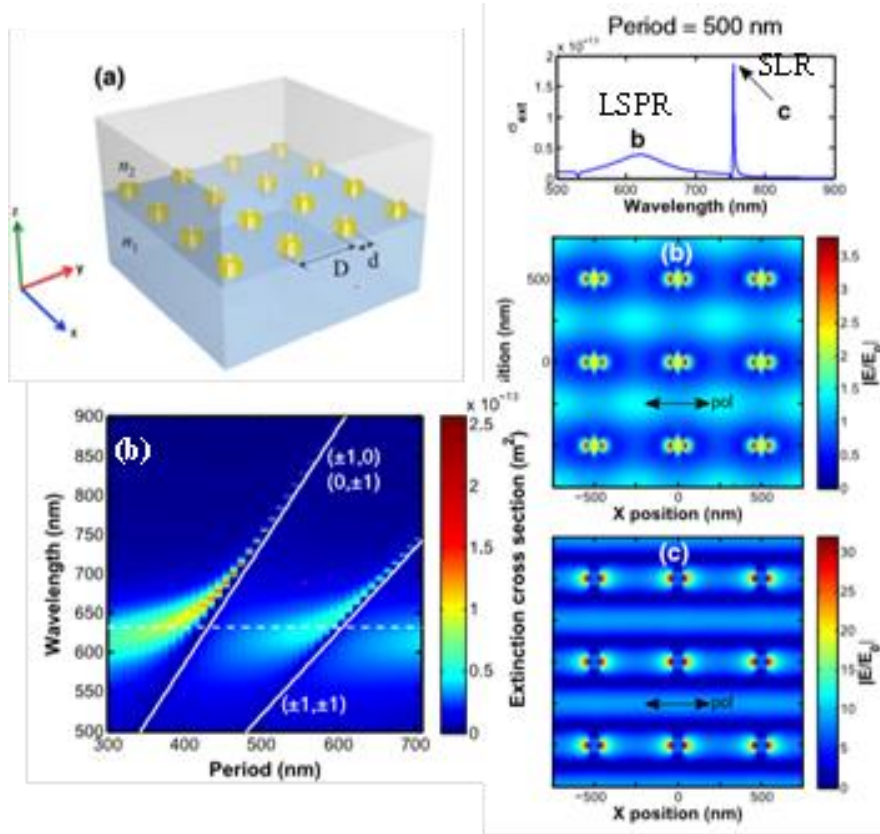


Figure 1-5. (a) Schematic illustration of Au Lattice structure. (b) extinction cross-section spectrum of Au Lattice structure for different lattice periods. Solid lines show the theoretical position of Rayleigh anomalies. (c) The extinction spectrum of Au lattice structure whose spacing is 500 nm. (d-e) FDTD maps of the normalized electric field modulus of (d) LSP mode and (e) SLR mode. The black arrow denotes the incident polarization.⁵³

The far field coupling of LSPs with scattered radiation fields makes it possible to dramatically improve the quality factor. When many particles are randomly dispersed, the scattered fields impinging on a given particle have no particular phase relationship and the effects of the scattered fields are relatively small.⁶⁷ However, when the nanoparticles are arranged in a periodic with the comparable period to the incident light wavelength, the fields scattered from the specific particle can arrive in the same phase as the incident light. The scattered fields correspond to the diffraction of the incident

light in the plane of the array. By using the appropriate the nanostructure geometry with the distinct array period, the diffracted light and the LSPs excited by the incident light can be adjusted and coupled to be in phase with each other. This far field coupling known as surface lattice resonance (SLR) can lead to the significant improvement of quality factor as well as the dramatic enhancement of both absorption and the local electromagnetic field because the diffracted fields can act to counter the radiative damping of the single particle response.⁶⁸

The fundamental ideas of surface lattice resonance were explored in theoretical works by several research groups since 1960s. DeVoe *et al.*, gave the first theoretical description using an electric dipole model for quasi-stationary aggregations of molecules,^{69,70} then Purcell and Pennypacker summarized this model with adding phase retardation effects which was based on the consideration of propagation of electromagnetic waves.⁷¹ After several years, the first coupled dipole approximation (CDA) for nanoparticle aggregations, leading to Mie solutions of the dipole sum, was constructed by Laor and Schatz.⁷² Then, this CDA model was extended by including retardation effects due to wave propagation and mean polarizability of whole nanoparticles, giving the critical perspective that a high quality factor for SLR comes from hybridized between the narrow diffracted mode such as Rayleigh anomaly with the LSPs of nanoparticles.⁷³⁻⁷⁶ Currently, the SLR properties such as electromagnetic field and optical cross-section can be easily and computationally reproduced through the FDTD method.

Despite a well-developed mathematical description of ultranarrow resonances and clarification of the physical mechanism, the experimental observation of these resonances was not straightforward until the 2000s.⁷⁷⁻⁸² Later studies provided an

improved understanding of the properties and conditions necessary for the excitation of ultranarrow plasmonic resonances. There were two factors that contributed to the lack of observation of narrow resonances: one is the environmental factors such as the high numerical aperture of incident light^{78,80} and the refractive index mismatch of the surrounding mediums.^{79,80} Another is the structural factors, such as the number of particles⁸¹ and the uniformity of each nanoparticles.⁸² The environmental factor gives the low spatial coherence of the incident light and diffracted light, resulting in the limited number of dipoles that could interact in phase with each other. The structural factor significantly increases the polarizability disorder induced in individual particles and reduces the essential quality of each LSP.

1.7 Stimulated Emission via Plasmonic Crystals

According to the Fermi's golden rule, the spontaneous emission rate of an emitter is proportional to the LDOS and can be enhanced within an optical microcavity by the Purcell factor F_P . The Purcell factor is typically used to quantify the enhanced spontaneous emission rate in dielectric resonators and it is proportional to influence the fluorescence intensity and/or buildup dynamics of population inversion for lasing.¹⁰⁴ A simplified expression for F_P is follows;¹⁰⁵

$$F_P = \frac{Q\lambda^3}{4\pi^2V}\beta^2$$

where Q depends on the spectral line width and mode volume V are defined as the electromagnetic field confinement. A large LDOS can increase not only the rate of spontaneous emission but also stimulated emission processes in the lasing action, which can improve laser modulation speeds without requiring stronger pump powers.

SLR provides not only high quality factor for plasmonic system, but also extending the plasmon lifetime,⁸³ enhanced and spatially expanded near field,^{80,84} and the degree of freedom in the moment of propagating light.^{85,86} Since SLR is the same kind of propagating polariton as SPPs, an optical band depending on the incident light angle is formed in whole array same as photonic crystals. The optical band can be easily modulated by changing the lattice shape. For example, in square plasmonic lattice, band edge modes are formed at zero wavevector where correspond to the Γ point in the band structure, so slow light with a nearly zero group velocity can be trapped at the band edge states resulting in a large local density of optical states (LDOS).⁸⁷⁻⁸⁹ In honeycomb lattices, an effective Dirac Hamiltonian can be induced and Dirac-like bosonic collective plasmons can be excited in the vicinity of two Dirac points in the Brillouin

zone.^{90,91} These edge states provide two-dimensionally propagating plasmons depending on the lattice space. In addition, by tuning the polarization of incident light, band edge point in the Brillouin zone could be manipulated to produce a band gap at the specific incident angles.⁹¹ The metal periodic structure exhibiting SLR is also called a plasmonic crystal, and is expected to be applied to a low-threshold plasmonic laser (see section 1.5), high sensitivity sensor, or the multiple color film due to the light confinement originated from the above-mentioned features and defects.^{74,92,93}

Until now, the 2D-plasmon lasing devices have been constructed using the square lattice of Au nanodisks on transparent substrates covered with a solid gain layer of dye adsorbed in the polymer matrix⁸⁷ or immersed in the liquid gain medium.^{117,118} In these system, samples were optically pumped with 800 nm femtosecond pulses (repetition rates: 10 kHz). Under the illumination of the laser, the arrays emitted light from the surface. Above the lasing threshold, a narrow emission peak emerged with the fwhm of 1.3 nm and directional beam emission with a small divergence angle ($< 1.5^\circ$) was observed.^{87,117}

2D-plasmon lasing action can be well described by combining rate equation using a four-level electronic state model with electromagnetic field simulation.¹¹⁹⁻¹²⁴ From theoretical estimations, below the lasing threshold, the stimulated transition rate is negligible compared to that of the spontaneous emission. On the other hand, above the threshold, the stimulated emission rate was 4 orders of magnitude higher than the spontaneous emission rate. A spatial map of the stimulation emission revealed that the population inversion leading to lasing action had maximum values in hotspot regions within 25 nm of the nanoparticle, which was in great agreement with the near field patterns at the band edge. This calculation confirmed that the nanoscale localization of

near fields stimulated excited state gain to resonantly transfer energy into surface plasmons.

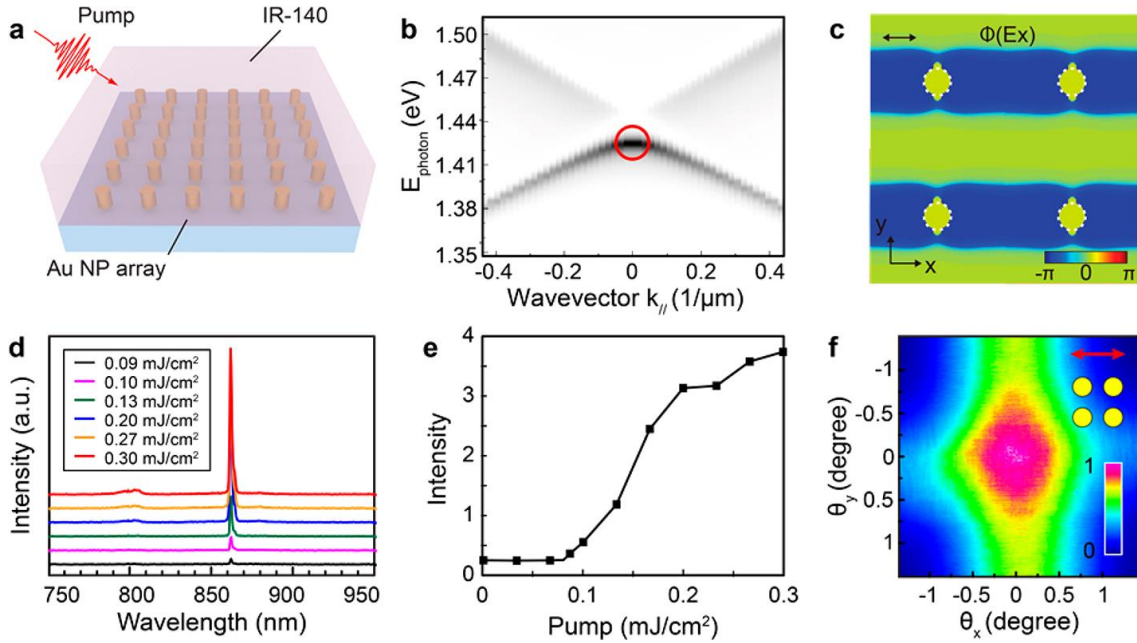


Figure 1-6. Directional lasing from spaser NP arrays. (a) Scheme showing a laser device including gold NP arrays embedded in liquid or solid-state gain media. (b) Calculated optical band structure. (c) Simulated phase profile at lattice plasmon resonances. (d,e) Power dependent lasing emission and input-power-output-intensity curves. (f) Far-field beam profile with a highly directional lasing spot.

1.8 Bose-Einstein Condensation with Strong Coupling Regime

The high Q factor of SLR provides a highly coherent electric field space. In recent years, unique optical and physical phenomena based on exciton polariton systems have been attracted attention, such as greatly enhancement of Raman scattering cross section,¹⁷⁶⁻¹⁷⁸ third harmonic generation,^{179,180} improving of photon-electron conversion efficiency and increasing the quantum efficiency of water splitting.¹⁸¹ These phenomena are based on the coherent interaction of strong coupling system.¹⁸² In the last few years, some groups have demonstrated the Bose-Einstein condensation (BEC) at room temperature by increasing coherent interactions in strong coupling system, and are expected to have new applications in chemical reactions and photophysics. BEC is an aggregation state that has a high density of bosonic particles in the lowest quantum state, leading to spatially overlapping wave functions of the bosonic particles.¹⁸³ The overlapping wave functions give rise to macroscopic quantum phenomena such as interference between the wave functions of the particles, superfluid and superconductivity. Due to their low effective mass (1/10000 times smaller than bare excitons) and high binding energy of organic excitons, polaritons can produce a BEC at higher temperatures as compared to atoms, which require cryogenic conditions. Kasprzak *et al.* demonstrated the first polariton BEC using a CdTe-based microcavity.¹⁸⁴ Inorganic based exciton-polariton BECs have been used to demonstrate thermal equilibrium below the threshold,^{184,185} threshold corresponding to onset of degeneracy,¹⁸⁵⁻¹⁸⁶ narrowing of the linewidth, long-range spatial coherence,^{184,185,187} temporal coherence,^{184,188} spontaneous polarization¹⁸⁹ and polariton accumulated coherence.¹⁹⁰ In another study, a plasmonic lattice was used instead of an optical cavity. As an emitter, perylene bisimide/PMMA matrix was used in this system.¹⁹¹ It was found

that the lasing threshold of the system depends on the concentration of the dye inside the polymer matrix: the higher the concentration the lower the lasing threshold value.¹⁹¹ The optical properties of the BEC differ substantially from those of the polaritons. The emission peak at band edge ($k_{\parallel}=0$) was blue shifted due to a repulsive interaction between polaritons, and a nonlinear increase in emission intensity as a function of pumping intensity was observed as well as a sudden decrease in bandwidth. In addition, the emission was polarized like the pump beam and showed a long-range phase coherence, which was proven by the use of a Michelson interferometer.^{192,193} The possibility to reach room temperature exotic matter phases offers a way to explore new chemistry.¹⁹⁴ Furthermore, electrically pumped polariton lasers open the door to engineer devices being orders of magnitude more energy efficient due to the low lasing threshold.^{195,196}

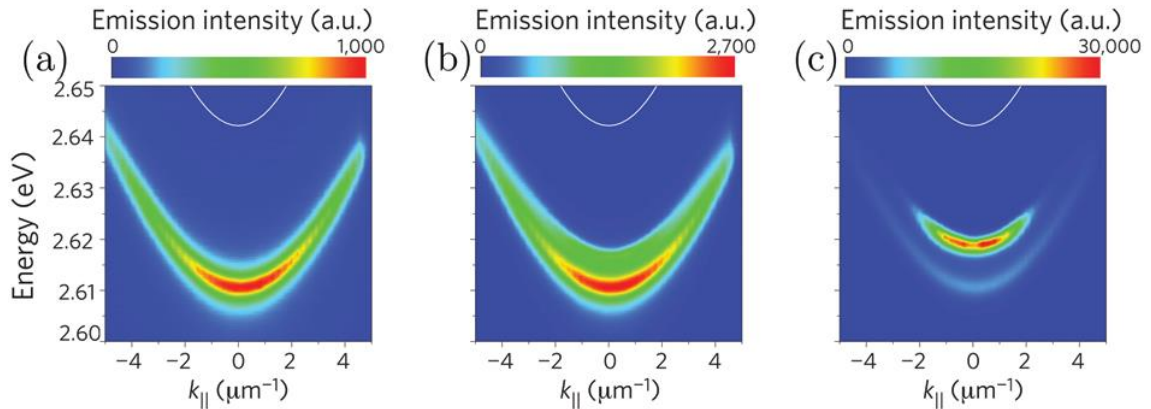


Figure 1-7. Emission from the lower polariton (a) below the threshold, (b) near the threshold and (c) above the threshold measured by momentum-resolved time-integrated spectroscopy. A blue shift of the emission is observed in (b and c), and the emission intensity increases nonlinearly.

1.9 Purpose of This Paper

In this paper, for high efficient utilization of visible light, I attempted to create a system enabling efficiently light energy transfer and condensation into a very small space by combining two-dimensionally expanded plasmon-active Au nanostructures with dye molecules. Extreme light condensation via higher-order plasmon excitation at room temperature was achieved by using low-temperature annealing, electrochemical methods, and various spectroscopic measurements. Then, I demonstrated the application of observed optical phenomena, such as lasers and strong couplings by interacting light and matter. Based on these findings, it was realized for the first time that efficient light propagation and light aggregation are possible by strong interactions between the lattice structure with specific defects and dye molecules. The research scheme is as follows. In chapter 2, a method for improving energy loss due to the decrease of the structural inhomogeneity in the metal nanostructures produced by top-down method was introduced. In chapter 3, the establishment of a precise control method for the Au dimer gap, and the ultimate light confinement with controlled structure with the method was demonstrated. In chapter 4 and 5, the fluorescence enhancement process mediated by dark plasmons and strong coupling induced in the Au square lattice structure was discussed. Chapter 6 showed a new system enabling efficient light propagation and light condensation into the void defects in the plasmonic lattice structure.

The present study will offer a novel method to concentrate the efficient light energy into the nanoscale region which can realize the novel light-matter phase and the effective light energy conversion system.

1.10 References

- (1) Jones M. R., Osberg K. D., Macfarlane R. J., Langille M. R. and Mirkin C. A. *Chem. Rev.*, **111**, 3736–3827 (2011).
- (2) Ringe E., Zhang J., Langille M. R., Sohn K., Cobley C., Au L., Xia Y., Mirkin C. A., Huang J., Marks L. D. and Van D. R. P., *Mater. Res. Soc. Symp. Proc.*, **1208**, O10-02 (2010).
- (3) Ringe E., Langille M. R., Sohn K., Zhang J., Huang J., Mirkin C. A., Van D. R. P. and Marks L. D. *J. Phys. Chem. Lett.*, **3**, 1479–1483 (2012).
- (4) Jain P. K. and El M. A. *J. Phys. Chem. C*, **111**, 17451–17454 (2007).
- (5) Brandl D. W., Mirin N. A. and Nordlander P. *J. Phys. Chem. B*, **110**, 12302-12310 (2006).
- (6) Ghosh S. K. and Pal T. *Chem. Rev.*, **107**, 4797–4862 (2007).
- (7) Ashcroft N. W. and Mermin D. N. *Solid Stat. Physics*, Cengage Learning (1976).
- (8) Oates T. W. H., Wormeester H. and Arwin H. *Prog. Surf. Sci.*, **86**, 328-376 (2011).
- (9) Lackowicz J. R., *Plasmonics*, **1**, 5-33 (2006).
- (10) Dostalek J. and Knoll W., *Biointerphases*, **3**, 12-22 (2008).
- (11) Mayer K. M. and Hafner J. H., *Chem. Rev.*, **111**, 3828–3857 (2011).
- (12) Biagioni P., Huang J. and Hecht B. *Rep. Prog. Phys.*, **75**, 024402 (2012).
- (13) Zuloaga J. and Nordlander P. *Nano Lett.*, **11**, 1280–3 (2011).
- (14) Kats M. A., Yu N., Genevet P., Gaburro Z. and Capasso F. *Opt. Express* **19**, 21748–53 (2011).
- (15) Kreibig U. and Vollmer M. *Optical Properties of Metal Clusters* (Berlin: Springer)(1995)
- (16) Mayer K. M. and Hafner J. H. *Chem. Rev.*, **111**, 3828–57, (2011).
- (17) Amendola V., Sajaia R., Maragò O. M. and Iatì A. *Nanoscale*, **19**, 8782–92 (2015).
- (18) Blaber M. G., Arnold M. D. and Ford M. J. *J. Phys. Condens. Matter*, **22**, 143201 (2010).
- (19) Arnold M. D. and Blaber M. G. *Opt. Express*, **17**, 3835–47 (2009).
- (20) Amendola V. and Meneghetti M. *Phys. Chem. Chem. Phys.*, **11** 3805–21 (2009).
- (21) Daniel M. C. and Astruc D. *Chem. Rev.*, **104**, 293–346 (2004).
- (22) Link S. and El-Sayed M. A. *Annu. Rev. Phys. Chem.*, **54**, 331–66 (2003).
- (23) Voisin C., Del Fatti N., Christofilos D. and Vallée F. *J. Phys. Chem. B*, **105**, 2264–80 (2001).
- (24) Maier S. A. *Plasmonics: Fundamentals and Applications* (Springer) (2007).

- (25) Sönnichsen C., Franzl T., Wilk T., von Plessen G., Feldmann J., Wilson O. and Mulvaney P. *Phys. Rev. Lett.*, **88**, 077402 (2002).
- (26) Sönnichsen C., Franzl T., Wilk T., Von Plessen G. and Feldmann J. *New J. Phys.*, **4**, 93 (2002).
- (27) Alabastri A., Tuccio S., Giugni A., Toma A., Liberale C., Das G., Angelis F. D., Fabrizio E.D. and Zaccaria R. P. *Materials*, **6**, 4879–910 (2013).
- (28) Link S. and El-Sayed M. A. *J. Phys. Chem. B* **103** 4212–7 (1999).
- (29) Aruda K. O., Tagliazucchi M., Sweeney C. M., Hannah D. C., Schatz G. C. and Weiss E. A. *Proc. Natl Acad. Sci. USA*, **110**, 4212–7 (2013).
- (30) Tang Y. and Ouyang M. *Nat. Mater.*, **6**, 754–9 (2007).
- (31) Li X., Xiao D. and Zhang Z. *New J. Phys.*, **15**, 023011 (2013).
- (32) Brongersma M. L., Halas N. J. and Nordlander P. *Nat. Nanotechnol.*, **10**, 25–34 (2015).
- (33) Meng X., Liu L., Ouyang S., Xu H., Wang D., Zhao N. and Ye J. *Adv Mater.*, **28**, 6781–803 (2016).
- (34) Perner M., Bost P., Lemmer U., Von Plessen G., Feldmann J., Becker U., Mennig M., Schmitt M. and Schmidt H. *Phys. Rev. Lett.*, **78**, 2192 (1997).
- (35) Dulkeith E., Niedereichholz T., Klar T., Feldmann J., Von Plessen G., Gittins D., Mayya K. and Caruso F. *Phys. Rev. B.*, **70**, 205424 (2004).
- (36) Zohar N., Chuntanov L. and Haran G. *J. Photochem. Photobiol. C: Photochem. Rev.*, **21**, 26–39 (2014).
- (37) Ghosh S. K. and Pal T. *Chem. Rev.*, **107**, 4797–862 (2007).
- (38) McMahon, J. M., Li, S., Ausman, L. K. & Schatz, G. C. *J. Phys. Chem. C*, **116**, 1627. (2012).
- (39) Yoshito T., Akio S., Keiji S., *SCIENTIFIC REPORTS*, **2**, 764 (2012).
- (40) Mirin N. A., Bao K. and Nordlander P. *J. Phys. Chem. A*, **113**, 4028–34 (2009).
- (41) Storhoff J. J., Lazarides A. A., Mucic R. C., Mirkin C. A., Letsinger R. L. and Schatz G. C. *J. Am. Chem. Soc.*, **122**, 4640–50 (2000).
- (42) Messina E. *ACS Nano*, **5**, 905 (2011).
- (43) Taylor R. W., Esteban R., Mahajan S., Coulston R., Scherman O. A., Aizpurua J. and Baumberg J. J. *J. Phys. Chem. C*, **116**, 25044–51 (2012).
- (44) Lovera A., Gallinet B., Nordlander P. and Martin O. J. *ACS Nano*, **7**, 4527–36 (2013).

- (45) Rahmani M., Lukiyanchuk B., Ng B., Kg A. T., Liew Y. and Hong M. *Opt. Express*, **19**, 4949–56 (2011).
- (46) Mukherjee S., Sobhani H., Lassiter J. B., Bardhan R., Nordlander P. and Halas N. J. *Nano Lett.*, **10**, 2694–701 (2010).
- (47) Jain P. K., Huang W. and El-Sayed M. A. *Nano Lett.*, **7**, 2080–8 (2007).
- (48) Atay T., Song J. and Nurmikko A. V. *Nano Lett.*, **4**, 1627–31 (2004).
- (49) Wang, Y. *et al. Nanoscale* **5**, 9897 (2013).
- (50) Wen, F. *et al. ACS Nano* **9**, 6428 (2015).
- (51) Pérez-González, O. *et al. Nano Lett.*, **10**, 3090 (2010).
- (52) Zhu, W. *et al. Nat. Commun.*, **7**, 1 (2016).
- (53) Esteban, R., Borisov, A. G., Nordlander, P. & Aizpurua, J. *Nat. Commun.*, **3**, 825 (2012).
- (54) Jensen, T. R., Malinsky, M. D., Haynes, C. L., Van Duyne, R. P. *J. Phys. Chem. B*, **104**, 10549–10556 (2000).
- (55) Zhang, X., Hicks, E. M., Zhao, J., Schatz, G. C., Van Duyne, R. *Nano Lett.*, **5**, 1503–1507 (2005).
- (56) Si, G., Zhao, Y., Lv, J., Lu, M., Wang, F., Liu, H., Xiang, N., Huang, T. J., Danner, A. J., Teng, J. *Nanoscale*, **5**, 6243–6248 (2013).
- (57) Hao, F., Nehl, C. L., Hafner, J. H., Nordlander, P. *Nano Lett.*, **7**, 729–732 (2007).
- (58) Senthil Kumar, P., Pastoriza-Santos, I., Rodríguez-González, B., Javier García de Abajo, F., Liz-Marzan, L. M. *Nanotechnology*, **19**, 015606 (2008).
- (59) Rodríguez-Fortuño, F. J., Martínez-Marco, M., Tomás-Navarro, B., Ortuño, R., Martí, J., Martínez, A., Rodríguez-Cantó, P. *J. Appl. Phys. Lett.*, **98**, 133118 (2011).
- (60) Wang, F., Shen, Y. R. *Phys. Rev. Lett.*, **97**, 206806 (2006).
- (61) Prodan, E., Radloff, C., Halas, N. J., Nordlander, P. A. *Science*, **302**, 419–422 (2003).
- (62) Rechberger, W., Hohenau, A., Leitner, A., Krenn, J., Lamprecht, B., Aussenegg, F. *Opt. Commun.*, **220**, 137–141 (2003).
- (63) Nordlander, P., Oubre, C., Prodan, E., Li, K., Stockman, M. *Nano Lett.*, **4**, 899–903 (2004).
- (64) Halas, N. J., Lal, S., Chang, W.-S., Link, S., Nordlander, P. *Chem. Rev.*, **111**, 3913–3961 (2011).
- (65) Panina, L. V., Grigorenko, A. N., Makhnovskiy, D. P. *Phys. Rev. B: Condens. Matter Mater. Phys.*, **66**, 155411 (2002).

- (66) Koh, A. L., Bao, K., Khan, I., Smith, W. E., Kothleitner, G., Nordlander, P., Maier, S. A., McComb, D. W. *ACS Nano*, **3**, 3015–3022 (2009).
- (67) Zoric, I., Zäch, M., Kasemo, B., Langhammer, C. *ACS Nano*, **5**, 2535–2546 (2011).
- (68) Rodriguez, S., Schaafsma, M., Berrier, A., Gómez Rivas, J. *Phys. B*, **407**, 4081–4085 (2012).
- (69) DeVoe, H. *J. Chem. Phys.*, **41**, 393–400 (1964).
- (70) DeVoe, H. *J. Chem. Phys.*, **43**, 3199–3208 (1965).
- (71) Purcell, E. M., Pennypacker, C. R. *Astrophys. J.*, **186**, 705–714 (1973).
- (72) Laor, U., Schatz, G. C. *Chem. Phys. Lett.*, **82**, 566–570 (1981).
- (73) Markel, V. J. *Mod. Opt.*, **40**, 2281–2291 (1993).
- (74) Zou, S., Janel, N., Schatz, G. C. *J. Chem. Phys.*, **120**, 10871–10875 (2004).
- (75) Markel, V. A. *J. Phys. B: At., Mol. Opt. Phys.*, **38**, L115–L121 (2005).
- (76) Zou, S., Schatz, G. C. *Nanotechnology*, **17**, 2813–2820 (2006).
- (77) Lamprecht, B. *et al. Phys. Rev. Lett.*, **84**, 4721 (2000).
- (78) Kravets, V. G., Schedin, F., Grigorenko, A. N. *Phys. Rev. Lett.*, **101**, 087403 (2008).
- (79) Auguié, B., Barnes, W. L. *Phys. Rev. Lett.*, **101**, 143902 (2008).
- (80) Chu, Y., Schonbrun, E., Yang, T., Crozier, K. B. *Appl. Phys. Lett.*, **93**, 181108 (2008).
- (81) Zou, S., Schatz, G. C. *J. Chem. Phys.*, **121**, 12606–12611 (2004).
- (82) Auguié, B., Barnes, W. L. *Opt. Lett.*, **34**, 401–403 (2009).
- (83) Rodriguez, S. R. K. *et al. Phys. Rev. X*, **1**, 21019 (2011).
- (84) Nikitin, A. G., Kabashin, A. V., Dallaporta, H. *Opt. Express*, **20**, 27941–27952 (2012).
- (85) Saj, W. M. *Opt. Express*, **13**, 4818 (2005).
- (86) Guo, R., *et al.*, *Phys. Rev. B*, **95**, 1 (2017).
- (87) Zhou, W., Dridi, M., Suh, J. Y., Kim, C. H., Co, D. T., Wasielewski, M. R., Schatz, G. C., Odom, T. W. *Nat. Nanotechnol.*, **8**, 506–511 (2013).
- (88) Figotin, A., Vitebskiy, *Waves in Random and Complex Media* 2006, 16, 293–382 (2006).
- (89) Krauss, T. F. *Nat. Photonics*, **2**, 448–450 (2008).
- (90) Han, D., Lai, Y., Zi, J., Zhang, Z. Q., Chan, C. T. *Phys. Rev. Lett.*, **102**, 123904 (2009).
- (91) Weick, G., Woollacott, C., Barnes, W. L., Hess, O., Mariani, E. *Phys. Rev. Lett.*, **110**, 106801 (2013).
- (92) Schokker, A. H., Koenderink, A. F. *ACS Photonics*, **2**, 1289–1297 (2015).

- (93) Schokker, A. H., Koenderink, A. F. *Optica*, **3**, 686–693 (2016).
- (94) Lakowicz J. R., *Principles of Fluorescence Spectroscopy*, (Springer Academic) (2006).
- (95) Tsai Y. C., Lin C. F. and Chang J. W. *Opt. Rev.*, **16**, 347–350 (2009).
- (96) Mertens H., Koenderink A. F. and Polman A. *Phys. Rev. B: Condens. Matter Mater. Phys.*, **76**, 115123 (2007).
- (97) Khurgin J. B. and Sun G., *J. Opt. Soc. Am. B*, **26**, B83–B95 (2009).
- (98) G. Sun, J. B. Khurgin and C. C. Yang, *Appl. Phys. Lett.*, 2009, 95, 171103 (2009).
- (99) Lakowicz J. R., *Anal. Biochem.*, **337**, 171–194 (2005).
- (100) Prodan E., Radloff C., Halas N. J. and Nordlander P., *Science*, **17**, 419–422 (2003).
- (101) Arnoldus H. F. and George T. F., *J. Chem. Phys.*, **87**, 4263 (1987).
- (102) Bharadwaj P. and Novotny L., *Opt. Express*, **15**, 14271 (2007).
- (103) Kang K. A., Wang J., Jasinski J. B. and Achilefu S., *J. Nanobiotechnol.*, **9**, 16 (2011).
- (104) Dridi M., Schatz G. C. *J. Opt. Soc. Am. B*, **32**, 818–823 (2015).
- (105) Purcell E. M., Torrey H. C. and Pound R. V., *Phys. Rev.*, **69**, 37–38 (1946).
- (106) Oulton R. F., Sorger V. J., Zentgraf T., Ma R. M., Gladden C., Dai L., Bartal G., Zhang X. *Nature*, **461**, 629–632 (2009).
- (107) Sidiropoulos T. P. H., Roeder R., Geburt S., Hess O., Maier S. A., Ronning C., Oulton R. F. *Nat. Phys.*, **10**, 870–876 (2014).
- (108) Zhang Q., Li G., Liu X., Qian F., Li Y., Sum T. C., Lieber C. M., Xiong Q. *Nat. Commun.*, **5**, 4953 (2014).
- (109) Lu Y. J., Kim J., Chen H. Y., Wu C., Dabidian N., Sanders C. E., Wang C. Y., Lu M. Y., Li B. H., Qiu X., Chang W. H., Chen L. J., Shvets G., Shih C. K., Gwo S. *Science*, **337**, 450–453 (2012).
- (110) Lu Y. J., Wang C. Y., Kim J., Chen H. Y., Lu M. Y., Chen Y. C., Chang W. H., Chen L. J., Stockman M. I., Shih C. K., Gwo, S. *Nano Lett.*, **14**, 4381–4388 (2014).
- (111) Stockman M. I. *Nat. Photonics*, **2**, 327–329 (2008).
- (112) Stockman M. I. *J. Opt.*, **12**, 024004 (2010).
- (113) Auguie B., Barnes W. L. *Phys. Rev. Lett.*, **101**, 143902 (2008).
- (114) Kravets V. G., Schedin F., Grigorenko A. N. *Phys. Rev. Lett.*, **101**, 087403 (2008).
- (115) Zou S., Janel N., Schatz G. C. *J. Chem. Phys.*, **120**, 10871–10875 (2004).

- (116) Humphrey A. D., Barnes W. L. *Phys. Rev. B: Condens. Matter Mater. Phys.*, **90**, 075404 (2014).
- (117) Yang A., Hoang T. B., Dridi M., Deeb C., Mikkelsen M. H., Schatz G. C., Odom T. W. *Nat. Commun.*, **6**, 6939 (2015).
- (118) Wang D., Wang W., Hua Y., Schaller R. D., Yang A., Schatz G. C., Odom T. W. *Nat. Nanotechnol.*, **12**, 889–894 (2017).
- (119) Chua S. L., Chong Y. D., Stone A. D., Soljacic M., Bravo-Abad J. *Opt. Express*, **19**, 1539–1562 (2011).
- (120) Bermel P., Lidorikis E., Fink Y., Joannopoulos J. D. *Phys. Rev. B: Condens. Matter Mater. Phys.*, **73**, 165125 (2006).
- (121) Chang S. H., Taflove A. *Opt. Express*, **12**, 3827–3833 (2004).
- (122) Huang Y. Y., Ho S. T. *Opt. Express*, **14**, 3569–3587 (2006).
- (123) Teixeira F. L. *IEEE Trans. Antennas Propag.*, **56**, 2150–2166 (2008).
- (124) Zhukovsky S. V., Chigrin D. N., Lavrinenko A. V. *J. Phys. Rev. Lett.*, **99**, 073902 (2007).
- (125) Dirac P. A. M. *Proc. R. Soc. London, Ser. A*, **114**, 243–265 (1927).
- (126) Drexhage K. H. in *Progress in Optics*, ed. E. Wolf, Elsevier, **12**, 163–232 (1974).
- (127) Yakovlev V. A., Nazin V. G. and Zhizhin G. N. *Opt. Commun.*, **15**, 293–295 (1975).
- (128) Pockrand I., Brillante A. and Moebius D. *J. Chem. Phys.*, **77**, 6289–6295 (1982).
- (129) Jaynes E. T. and Cummings F. W. *Proc. IEEE*, **51**, 89–109 (1963).
- (130) Agranovich V. M. and Malshukov A. G. *Opt. Commun.*, **11**, 169–171 (1974).
- (131) Hopfield J. J., *Phys. Rev.*, **112**, 1555–1567 (1958).
- (132) Skolnick M. S., Fisher T. A. and Whittaker D. M. *Semicond. Sci. Technol.*, **13**, 645–669 (1998).
- (133) Holstein T. and Primakoff H. *Phys. Rev.*, **58**, 1098–1113 (1940).
- (134) Khitrova G., Gibbs H. M., Kira M., Koch S. W. and Scherer A. *Nat. Phys.*, **2**, 81–90 (2006).
- (135) Agranovich V. M., Gartstein Y. N. and Litinskaya M. *Chem. Rev.*, **111**, 5179–5214 (2011).
- (136) Houdre R., Stanley R. P. and Ilegems M. *Phys. Rev. A: At., Mol., Opt. Phys.*, **53**, 2711–2715 (1996).

- (137) Rice P. R. and Brecha R. J. *Opt. Commun.*, **126**, 230–235 (1996).
- (138) Tanji-Suzuki H., Chen W., Landig R., Simon J. and Vuletic V. *Science*, **333**, 1266–1269 (2011).
- (139) Zhao W., Wang S., Liu B., Verzhbitskiy I., Li S., Giustiniano F., Kozawa D., Loh K. P., Matsuda K., Okamoto K., Oulton R. F. and Eda G. *Adv. Mater.*, **28**, 2709–2715 (2016).
- (140) Miroschnichenko A. E., Flach S. and Kivshar Y. S. *Rev. Mod. Phys.*, **82**, 2257–2298 (2010).
- (141) Luk'yanchuk B., Zheludev N. I., Maier S. A., Halas N. J., Nordlander P., Giessen H. and Chong C. T. *Nat. Mater.*, **9**, 707–715 (2010).
- (142) Halas N. J., Lal S., Chang W. S., Link S. and Nordlander P. *Chem. Rev.*, **111**, 3913–3961 (2011).
- (143) Carusotto I. and Ciuti C. *Rev. Mod. Phys.*, **85**, 299–366 (2013).
- (144) Ridolfo A., Leib M., Savasta S. and Hartmann M. J. *Phys. Rev. Lett.*, **109**, 193602 (2012).
- (145) Hamsen C., Tolazzi K. N., Wilk T. and Rempe G. *Phys. Rev. Lett.*, **118**, 133604 (2017).
- (146) Vasanelli A., Todorov Y. and Sirtori C. *C. R. Phys.*, **17**, 861–873 (2016).
- (147) Jaako T., Xiang Z. L., Garcia-Ripoll J. J. and Rabl P. *Phys. Rev. A: At., Mol., Opt. Phys.*, **94**, 033850 (2016).
- (148) Martí'nez L. A., Ribeiro R. F., Campos G. A. J. and Yuen-Zhou J. *ACS Photonics*, **5**, 167–176 (2018).
- (149) Pino del J., Feist J. and Garcia-Vidal F. J. *New J. Phys.*, **17**, 053040 (2015).
- (150) Coles D.M., Michetti P., Clark C., Adawi A. M. and Lidzey D. G. *Phys. Rev. B: Condens. Matter Mater. Phys.*, **84**, 205214 (2011).
- (151) Deng H., Haug H. and Yamamoto Y. *Rev. Mod. Phys.*, **82**, 1489–1537 (2010).
- (152) Lidzey D. G., Fox A. M., Rahn M. D., Skolnick M. S., Agranovich V. M. and Walker S. *Phys. Rev. B: Condens. Matter Mater. Phys.*, **65**, 10 (2002).
- (153) Coles D. M., Michetti P., Clark C., Tsoi W. C., Adawi A. M., Kim J. S. and Lidzey D. G. *Adv. Funct. Mater.*, **21**, 3691–3696 (2011).
- (154) Yuen-Zhou J., Saikin S. K. and Menon V. M. *J. Phys. Chem. Lett.*, **9**, 6511–6516 (2018).

- (155) Schwartz T., Hutchison J. A., Genet C. and Ebbesen T. W. *Phys. Rev. Lett.*, **106**, 196405 (2011).
- (156) Hutchison J. A., Schwartz T., Genet C., Devaux E. and Ebbesen T. W. *Angew. Chem., Int. Ed.*, **51**, 1592–1596 (2012).
- (157) Feist J., Galego J. and Garcia-Vidal F. J. *ACS Photonics*, **5**, 205–216 (2018).
- (158) Galego J., Garcia-Vidal F. J. and Feist J. *Phys. Rev. X*, **5**, 041022 (2015).
- (159) Galego J., Garcia-Vidal F. J. and Feist J. *Nat. Commun.*, **7**, 13841 (2016).
- (160) Shalabney A., George J., Hutchison J., Pupillo G., Genet C. and Ebbesen T. W. *Nat. Commun.*, **6**, 5981 (2015).
- (161) George J., Shalabney A., Hutchison J. A., Genet C. and Ebbesen T. W. *J. Phys. Chem. Lett.*, **6**, 1027–1031 (2015).
- (162) George J., Chervy T., Shalabney A., Devaux E., Hiura H., Genet C. and Ebbesen T. W. *Phys. Rev. Lett.*, **117**, 153601 (2016).
- (163) Ahn W., Vurgaftman I., Dunkelberger A. D., Owrutsky J. C. and Simpkins B. S. *ACS Photonics*, **5**, 158–166 (2018).
- (164) Chervy T., Thomas A., Akiki E., Vergauwe R. M. A., Shalabney A., George J., Devaux E., Hutchison J. A., Genet C. and Ebbesen T. W. *ACS Photonics*, **5**, 217–224 (2018).
- (165) Simpkins B. S., Fears K. P., Dressick W. J., Spann B. T., Dunkelberger A. D. and Owrutsky J. C. *ACS Photonics*, **2**, 1460–1467 (2015).
- (166) Memmi H., Benson O., Sadofev S. and Kalusniak S. *Phys. Rev. Lett.*, **118**, 126802 (2017).
- (167) Long J. P. and Simpkins B. S. *ACS Photonics*, **2**, 130–136 (2015).
- (168) Casey S. R. and Sparks J. R. *J. Phys. Chem. C*, **120**, 28138–28143 (2016).
- (169) Vergauwe R. M. A., George J., Chervy T., Hutchison J. A., Shalabney A., Torbeev V. Y. and Ebbesen T. W. *J. Phys. Chem. Lett.*, **7**, 4159–4164 (2016).
- (170) Thomas A., George J., Shalabney A., Dryzhakov M., Varma S. J., Moran J., Chervy T., Zhong X., Devaux E., Genet C., Hutchison J. A. and Ebbesen T. W. *Angew. Chem., Int. Ed.*, **55**, 11462–11466 (2016).
- (171) Hiura H., Shalabney A. and George J. *Europe PMC* (2018),
DOI: 10.26434/chemrxiv.7234721.v1.

- (172) Coles D. M., Somaschi N., Michetti P., Clark C., Lagoudakis P. G., Savvidis P. G. and Lidzey D. G. *Nat. Mater.*, **13**, 712–719 (2014).
- (173) Zhong X., Chervy T., Zhang L., Thomas A., George J., Genet C., James H. A. and Ebbesen T. W. *Angew. Chem.*, **129**, 9162–9166 (2017).
- (174) Georgiou K., Michetti P., Gai L., Cavazzini M., Shen Z. and Lidzey D. G. *ACS Photonics*, **5**, 258–266 (2018).
- (175) Sa´ez-Bla´zquez R., Feist J., Ferna´ndez-Domi´nguez A. I. and Garcı´a-Vidal F. J. *Phys. Rev. B*, **97**, 241407 (2018).
- (176) Shalabney A., George J., Hiura H., Hutchison J. A., Genet C., Hellwig P. and Ebbesen T. W. *Angew. Chem., Int. Ed.*, **54**, 7971–7975 (2015).
- (177) Pino del J., Feist J. and Garcia-Vidal F. J. *J. Phys. Chem. C*, **119**, 29132–29137 (2015).
- (178) Strashko A. and Keeling J. *Phys. Rev. A*, **94**, 023843 (2016).
- (179) Chervy T., Xu J., Duan Y., Wang C., Mager L., Frerejean M., Munninghoff J. A. W., Tinnemans P., Hutchison J. A., Genet C., Rowan A. E., Rasing T. and Ebbesen T. W. *Nano Lett.*, **16**, 7352–7356 (2016).
- (180) Barachati F., Simon J., Getmanenko Y. A., Barlow S., Marder S. R. and Ke´na-Cohen S. *ACS Photonics*, **5**, 119–125 (2018).
- (181) Shi X., Ueno K., Oshikiri T., Sun Q., Sasaki K. and Misawa H. *Nat. Nanotechnol*, **13**, 953–958 (2018).
- (182) Groenhof G. and Toppari J. J. *J. Phys. Chem. Lett.*, **9**, 4848–4851 (2018).
- (183) Anderson M. H., Ensher J. R., Matthews M. R., Wieman C. E. and Cornell E. A. *Science*, **269**, 198–201 (2018).
- (184) Kasprzak J., Richard M., Kundermann S., Baas A., Jeambrun P., Keeling J. M. J., Marchetti F. M., Szymanska M. H., Andre R., Staehli J. L., Savona V., Littlewood P. B., Deveaud P. B. and Dang L. S. *Nature*, **443**, 409–414 (2006).
- (185) Balili R., Hartwell V., Snoke D., Pfeiffer L. and West K. *Science*, **316**, 1007–1010 (2007).
- (186) Deng H., Weihs G., Santori C., Bloch J. and Yamamoto Y. *Science*, **298**, 199–202 (2002).
- (187) Shalabney A., George J., Hutchison J., Pupillo G., Genet C. and Ebbesen T. W. *Nat. Commun.*, **6**, 5981 (2015).

- (188) Love A. P. D., Krizhanovskii D. N., Whittaker D. M., Bouchekioua R., Sanvitto D., Rizeiqi S. A., Bradley R., Skolnick M. S., Eastham P. R., Andre R. and Dang L. S. *Phys. Rev. Lett.*, **101**, 067404 (2008).
- (189) Baumberg J. J., Kavokin A. V., Christopoulos S., Grundy A. J. D., Butte R., Christmann G., Solnyshkov D., Malpuech G., Baldassarri G., Feltin E., Carlin J. F. and Grandjean N. *Phys. Rev. Lett.*, **101**, 136409 (2008).
- (190) Schneider C., Rahimi-Iman A., Kim N. Y., Fischer J., Savenko I. G., Amthor M., Lerner M., Wolf A., Worschech L., Kulakovskii V. D., Shelykh I. A., Kamp M., Reitzenstein S., Forchel A., Yamamoto Y. and Hofling S. *Nature*, **497**, 348–352 (2013).
- (191) Ramezani M., Halpin A., Fernandez-Dominguez A. I., Feist J., Rodriguez S. R. K., Garcia-Vidal F. J. and Rivas J. G. *Optica*, **4**, 31–37 (2017).
- (192) Plumhof J. D., Stoferle T., Mai L., Scherf U. and Mahrt R. F. *Nat. Mater.*, **13**, 247–252 (2013).
- (193) Cookson T., Georgiou K., Zasedatelev A., Grant R. T., Virgili T., Cavazzini M., Galeotti F., Clark C., Berloff N. G., Lidzey D. G. and Lagoudakis P. G. *Adv. Opt. Mater.*, **5**, 1700203 (2017).
- (194) Deng H., Weihs G., Snoke D., Bloch J. and Yamamoto Y. *Proc. Natl. Acad. Sci. U. S. A.*, **100**, 15318 (2003).
- (195) Wang J., Da P., Zhang Z., Luo S., Liao L., Sun Z., Shen X., Wu S., Zheng G. and Chen Z. *Nanoscale*, **10**, 10371–10376 (2018).

Chapter 2

Improvement of the Light Condensation on Plasmonic Arrays via Low Temperature Annealing

2.1 Introduction

Generally, the precisely controlled plasmonic nanomaterials are fabricated by the top-down lithographic methods such as electron-beam lithography (EBL).¹⁻³ As I described in the general introduction in chapter 1, such structures shows the intrinsic damping due to the dielectric function of the material. In addition, such defined nanostructures prepared by the conventional lithographic technique have other external factors such as grain boundaries, surface roughness, or adhesion layers,⁴⁻⁸ resulting in the low quality factor (Q-factor).^{9,10} As the proof of this, the metal nanoparticles synthesized by the wet-chemical process shows the relatively high Q-factor because of their high monocrystalline and smooth surface.^{11,12} In order to improve the Q-factor of lithographically defined structures, several approaches, such as the thermal annealing,^{5,13-15} (see figure 2-1), or the substituting metal adhesion layers with organic ligands^{9,16} have been suggested. However, these methods unfortunately lead to the drastic change in the structural shape or the dielectric environment of the metal structures. From such background, the promising methods enabling the improvement of the Q-factor are required to be established.

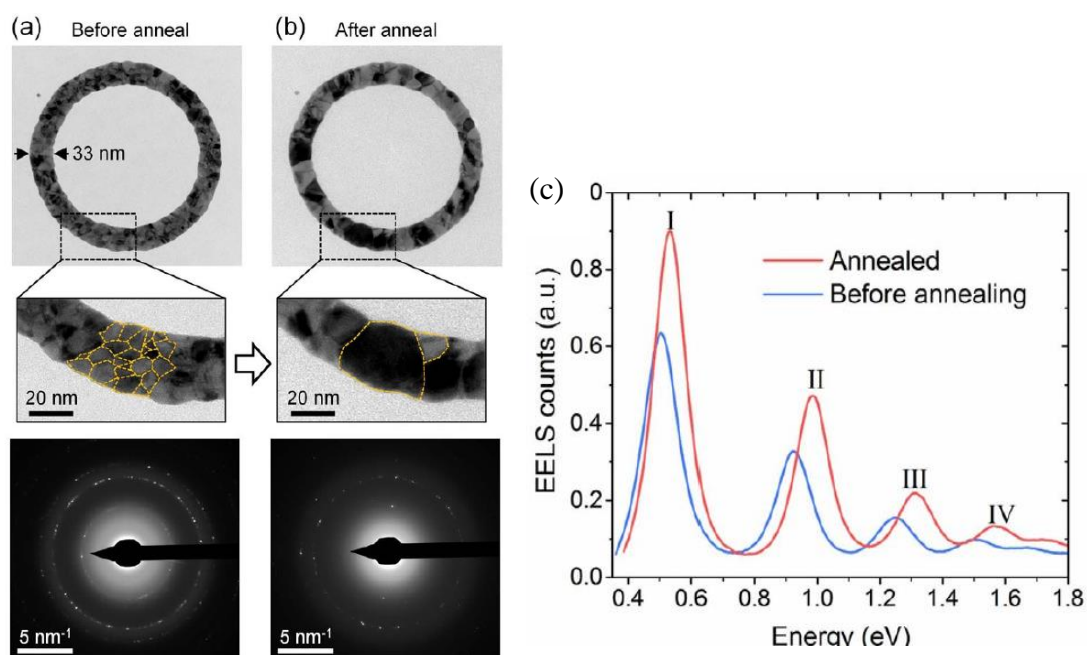


Figure 2-1. TEM image and electron diffraction pattern of the same ring structure before (a) and after annealing (b) at 400°C, showing a reduction in the density of grains and grain boundaries. (c) EELS spectra before and after annealing. Peaks I–IV with their corresponding EELS plasmon maps underneath show the first four harmonic resonance modes.¹⁵

In this chapter, I have proposed an easy way to improve the Q-factor of two dimensionally arranged gold nanostructures prepared by top-down methods. At the present investigation, the low-temperature annealing of the Au nanostructures are applied to reduce the surface grain boundaries without any changes in the structural geometry. The geometric and plasmonic properties of the gold nanostructures before and after low-temperature annealing were evaluated through SEM, XRD, electrochemical under potential deposition (UPD), and microspectroscopy measurements. Interestingly, it was found that, despite the incomplete removal of grain boundaries, annealed nanostructures showed the higher Q-factor close to the ideal result. The effect of the interface between the nanostructures and the dielectric substrate were also investigated because it effects on the Q-factor of the structure.

2.2 Experimental Method

2.2.1 Angle-Resolved Nanosphere Lithography (AR-NSL)

The Au nanoprism arrays were prepared by an angle-resolved nanosphere lithography technique (AR-NSL).^{17,18} The 400 μL of the PS bead colloidal solution was centrifuged at 9000 rpm for 10 min (see table 3-1), then, after removing all the supernatant solution, the 100 μL of ethanol and deionized water was added. Then PS beads was dispersed by sonication in water bath (at 10 $^{\circ}\text{C}$) for 10 minutes. After the preparation of the PS solutions, 20 μL of its solution were dropped on the surface of deionized water. Thin water layer on the glass surface leads to uniform spreading of PS beads at the air-water interface. After the spreading of PS beads onto the water surface, the closely packed monolayer of PS beads formed. The prepared high quality monolayer was then transferred onto the surface of the hydrophilized ITO substrate. The Au layer were deposited onto the polystyrene (PS) beads (Polysciences Inc.; diameters = 500 nm) monolayer supported on a ITO substrate ($n=1.71$) via the electron beam (EB) vapor deposition method.^{17,18} Then, the PS mask was removed by sonication in THF for 10s, and rinsed with acetone and deionized water. The structure of the dimer on the ITO substrate was inspected by an atomic force microscope (AFM, Nanoscope-IIIa, Digital Instruments) and Scanning electron microscope (SEM) (ELS-F125, Elionix Co.).

The spin coating conditions for the first PS bead adjustment were determined as follows. generally, the particles in the liquid are separated by centrifugation, but it may be difficult to resuspend the pellets if excessive centrifugal force is applied. Here, I introduce a method for calculating the ideal pellet formation time using the Stokes equation. The sedimentation velocity of spherical particles is described as

$$v = \frac{2gr^2(\rho_1 - \rho_2)}{9\eta}$$

where, v is the sedimentation velocity, g is the gravitational acceleration, r is the radius of the sphere particle, ρ_1 and ρ_2 are the densities of the particles and the suspended solvent, respectively, and η is the viscosity of the solution. The physical parameter of purchased PS bead solution is below; $2r = 500$ nm, $\rho_1=1.05$ g cm⁻³, $\rho_2=1.00$ g cm⁻³ and $\eta=1.002$, respectively. Stokes' equation is re-expressed as follows

$$v = (2.8 \times 10^{-6})Gd^2 [\text{cm s}^{-1}]$$

where G is the centrifugal force generated and d is the height of the solution. In practice, it is necessary to set the centrifugation time about 50% longer in order to form pellets that can be separated from the supernatant. Table 2-1 shows a table of sedimentation rate and ideal pellet formation time when the solution height is 0.5 cm and centrifuge radius is 8.2 cm.

Table 2-1. Ideal pellet formation time derived from the sedimentation velocity equation

ω [rpm]	G [cm ⁻¹ s ⁻¹]	v [cm s ⁻¹]	Pellet formation time [min]
4000	1468	1.0E ⁻³	46.7
5000	2294	1.6E ⁻³	29.9
6000	3303	2.3E ⁻³	20.8
7000	4496	3.1E ⁻³	15.3
8000	5873	4.1E ⁻³	11.7
9000	7432	5.1E ⁻³	9.2
10000	9176	6.4E ⁻³	7.5

2.2.2 Electron Beam Lithography (EBL)

The Au nanodisk arrays were fabricated on a slide glass substrate ($n = 1.51$) using electron beam lithography (EBL).¹⁻³ A positive-type resist (ZEP520a, Zeon Chemicals Co.) layer was formed by the spin-coating method at 4000 rpm for 60 s. Then, an spacer (320Z, Showa Denko Co.) film was formed in the same way. The substrate was then baked on a hotplate at 160°C for 4 min and was subsequently introduced into the EBL system (ELS-F125, Elionix Co.). The accelerating voltage and beam current of the EBL system were set at 125 kV and 100 pA, respectively. After the designed patterns were drawn, the spacer was removed by immersing it into deionized water, and then the resist layer was dissolved using ZED-N50 (Zeon Chemicals Co.) and rinsed by ZMD-B (Zeon Chemicals Co.). A 75-nm-thick Au film was deposited on the substrate by sputtering (MPS-400C1/HC1, ULVAC, Japan). The resist layer was subsequently removed from the substrate using a resist remover (ZDMAC, Zeon Chemicals Co.).

2.2.3 Steady-State Extinction Measurements

The linearly polarized light from a halogen source was focused at normal incidence on the surface of the sample with a condenser lens (numerical aperture, NA = 0.1). The transmitted light was collected using a 10x objective lens through an inverted microscope (Olympus IX-71) and was sent to the entrance port of an imaging spectrometer (Teledyne Princeton Instruments IsoPlane sct320) equipped with a charge-coupled device (CCD) camera (Teledyne Princeton Instruments PIXIS100). Transmission spectra were measured relative to bare substrate areas ($3 \times 3 \mu\text{m}^2$) of the sample.

2.2.4 Surface Analysis

The surface of the gold nanostructures before and after annealing was evaluated by the X-ray diffraction measurement (XRD) and under potential deposition (UPD) of Cu methods. XRD measurement was performed at a scan speed of 0.02° /sec using Cu as the radiation source ($K_{\alpha 1}$: 1.5405\AA , $K_{\alpha 2}$: 1.5443\AA).

The Cu UPD analysis was performed using three-electrode electrochemical cell. The prepared Au nanostructures supported on the conductive substrate were used as a working electrode. The counter and reference electrodes were a Pt plate and Ag/AgCl (sat. KCl aq.), respectively. Electrochemical measurements were performed in 0.1 M H_2SO_4 and 10 mM CuSO_4 aqueous solutions, using an automatic polarization system (Hokuto Denko, HSV-100).

2.3 Results and Discussion

2.3.1 Geometry and Extinction of Annealed Au Nanoprisms

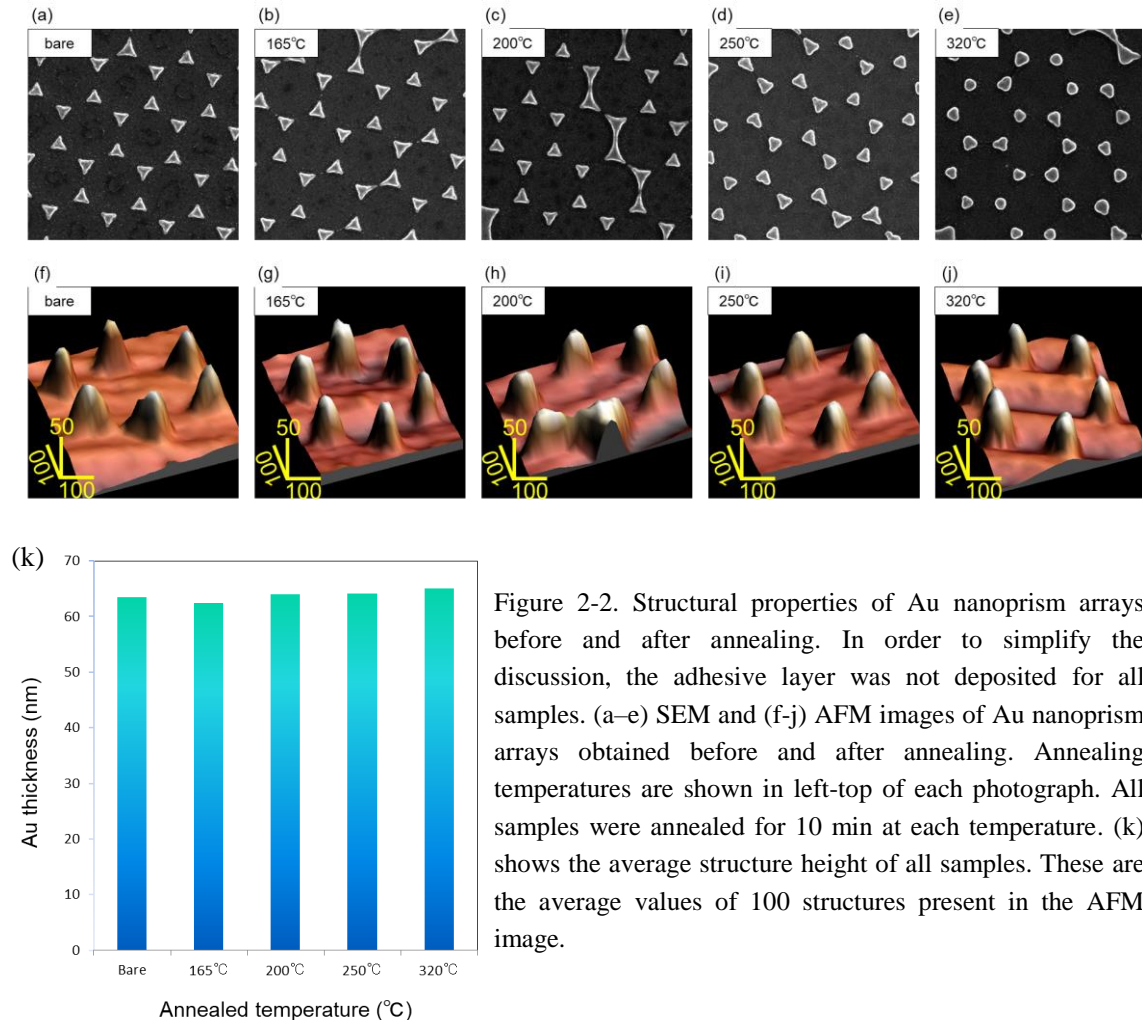


Figure 2-2. Structural properties of Au nanoprism arrays before and after annealing. In order to simplify the discussion, the adhesive layer was not deposited for all samples. (a–e) SEM and (f–j) AFM images of Au nanoprism arrays obtained before and after annealing. Annealing temperatures are shown in left-top of each photograph. All samples were annealed for 10 min at each temperature. (k) shows the average structure height of all samples. These are the average values of 100 structures present in the AFM image.

A uniform Au nanoprism array with a thickness of 40 nm was fabricated by AR-NSL method as shown in figure 2(a) and (f). The AR-NSL method can prepare the various type of structure by changing the deposition angle but the coupling effect between particles before and after annealing must be considered in multimers case. Thus, the monomer was prepared in this experiment to simplify the discussion. By annealing Au nanoprisms ranging between 165 and 320 °C, the effect of heat on the geometry and optical properties was investigated. Due to surface melting, remarkable

rounding of edges was observed at higher temperature than 250 °C (figure 2-2(d) and (e)), while the case for the lower than 250 °C, the shape was clearly maintained (figure 2-2(b),(c)). Interestingly, in the annealing temperature region in this experiment, the average particle thickness after annealing was almost stable. Considering that the particle volume is not changed before and after annealing, it is suggested that the Au atoms existing inside and/or surface are reorganized through annealing process. These results indicate that the atomic reconstruction on the surface and inside may be induced above 250 °C.

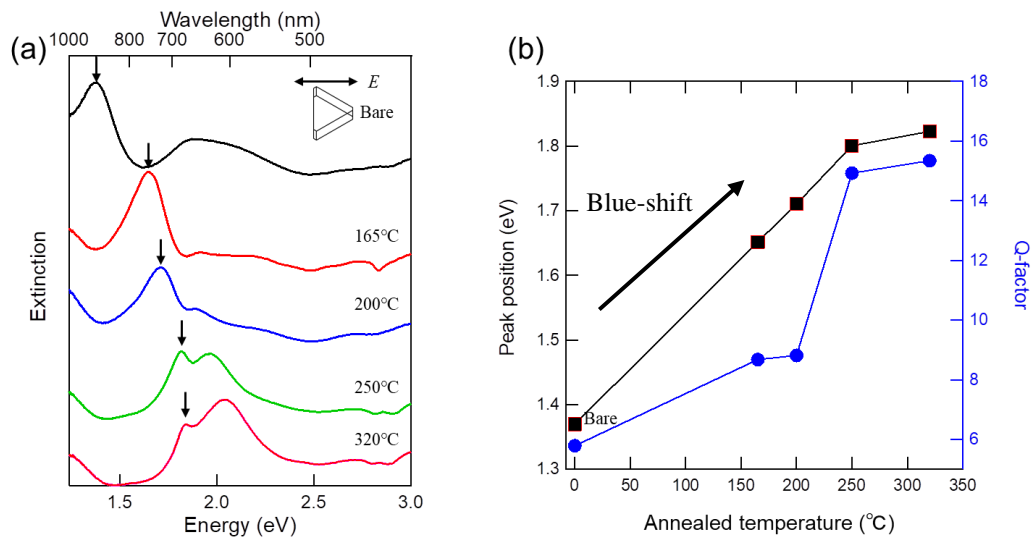


Figure 2-3. Optical properties of Au nanoprism arrays before and after annealing. (a) Extinction spectra of annealed structures under longitudinal incident light polarization. The shifted peaks are indicated by arrows. (b) LSP peak position (■) and Q-factor (●) of dipole LSP mode at lower energy. The peaks that appears around 2 eV (620 nm) after high temperature annealing corresponds to the substrate-structure interface mode (shown in 2.5.3)

The plasmon characteristics before and after annealing were examined by normal incident extinction measurement as shown in figure 2-3(a). The extinction spectra show the exponential blueshift of LSP depending on the annealing temperature. It was also observed that the Q-factor was improved up to 2 times higher than bare Au nanoprism. The blue shift of the LSP peak may be caused by a decrease in ohmic-loss

derived from the rearrangement of Au atoms or a change in geometry due to rounded edges. The FDTD simulations for the bare Au nanoprism well reproduced the extinction spectrum of the structure annealed at 200 °C for 30 min as shown in figure 2-4. Furthermore, the simulation revealed that another peak at 2 eV appeared after high temperature annealing originated from the interaction between the substrate and the nanostructure interface. Therefore, it is considered that the dramatically improvement of the Q-factor of the structure annealed at high temperature and the appearance of the substrate interface mode of plasmon are caused due to the change in the morphology of the entire structures. The structural change was not observed in the structure annealed below 200 °C in SEM and AFM images shown in figure 2-2(a)-(c) and (f)-(h), so it was considered that the Q-factor was improving by changing other structural factors at low temperature.

2.3.2 Time Dependent of Low Temperature Annealing

It was suggested that cold annealing could be used to improve the Q-factor of Au nanostructures without structural changes. However, it should be noted that the improvement of the Q-factor can be controlled by the annealing time, as the elimination of other structural factors causing ohmic-loss may not be completed early and sufficiently. Figure 2-4(a) shows the annealing time series of the extinction spectra of Au nanoprism. The temperature was fixed at 200 °C, and the structures were annealed within 30 min. The extinction spectra peak was not changed after annealing for longer than 30 min, but its Q-factor continued to improve up to maximum 15 shown in figure 2-4(b). The structural modification was not confirmed from the SEM images before and

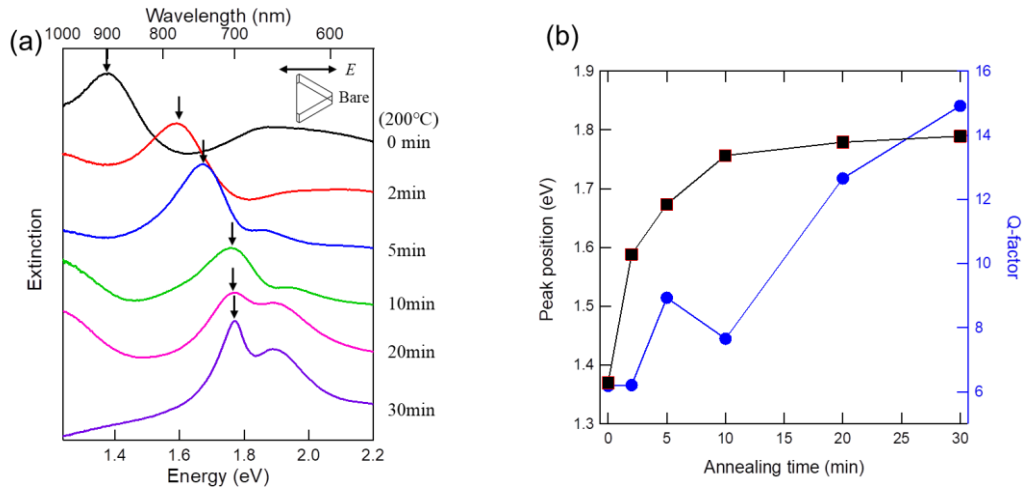


Figure 2-4. Optical properties of Au nanoprism arrays before and after annealing. (a) Extinction spectra of annealed structures under longitudinal incident light polarization. The annealing temperature was fixed at 200°C, and the time series of the extinction spectrum was recorded. (b) LSP peak position (■) and Q-factor (●) of dipole LSP mode at lower energy.

after annealing, suggesting that the elimination of other structural factors causing ohmic-loss was completed after 30 min. Since this structure has a small ohmic loss, it may be possible to express it in an electric field simulation such as FDTD calculation.

From the SEM and AFM images of before annealing, the pre-annealed (and post-annealed) Au nanoprisms were modeled as a triangular prism with a side of 100 nm and a film thickness of 40 nm in FDTD simulation. In figure 2-5 (a), the simulated extinction cross section corresponds reasonably well with the experimental extinction spectrum acquired after low temperature annealing, but mismatches that of bare structure. This result means that annealing has almost eliminated loss factors that cannot be modeled by FDTD, such as roughness or surface morphology. The calculated spectrum showed two major plasmon peaks at 1.93 eV and 1.77 eV. Electric field maps help us to understand these modes. The peak appearing at 1.77 eV forms strong electric fields across the edge shown in figure 2-5 (b) and (d). On the other hand, it can be seen that the electric field is concentrated at the interface of the ITO substrate at the peak appearing at 1.93 eV shown in figure 2-5 (c) and (e). Thus, it is considered that the

former is a normal LSP mode, and the latter is another LSP mode formed by interacting plasmon and substrate. The LSP mode called as proximal mode, which is caused by the interaction with the substrate interface, often appears in structures with sharp edges such as nanoblock structures and nanoprism structures supported on high refractive index materials.²⁶ Based on these results, It was found that low temperature annealing induces the blue shift of LSP by improving some factors such as roughness and surface morphology. Moreover, this process can support the new LSP mode like proximal mode by improving the adhesion and interaction between the substrate and the structure.

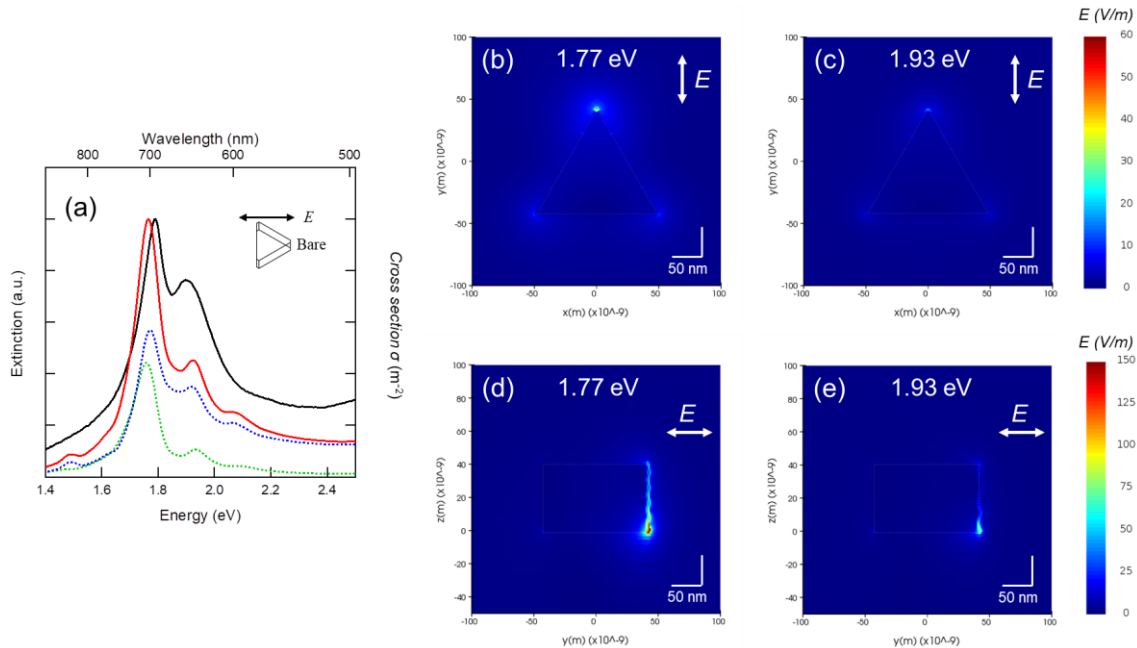


Figure 2-5. Simulated optical properties of Au nanoprism array. From the SEM and AFM images, the pre-annealed (and post-annealed) Au nanoprisms were modeled as a triangular prism with a side of 100 nm and a film thickness of 40 nm. The field simulation was performed with FDTD software of Lumerical. As an experimental environment, an ITO layer with a refractive index of 1.71 was assumed on the lower side of the structure, while upper side was set as air with a refractive index of 1.0. The simulation area was divided into 0.5 nm uniform meshes and PML was adopted for all boundary conditions. (a) shows the experimental extinction spectra (black line) and simulated extinction cross section (red line) under longitudinal light polarization. The dashed lines in the figure show the cross sections of absorption (green line) and scattering (blue line), respectively. (b)-(e) show the near field distributions at the two main peaks shown in (a). (b) and (c) are near field cross section at half the height of the structure ($h = 20\text{ nm}$), then (d) and (e) indicate the cross section of x-plane in the vertical bisector (horizontal to the polarization direction).

2.3.3 XRD Measurement for Annealed Au Nanoprisms

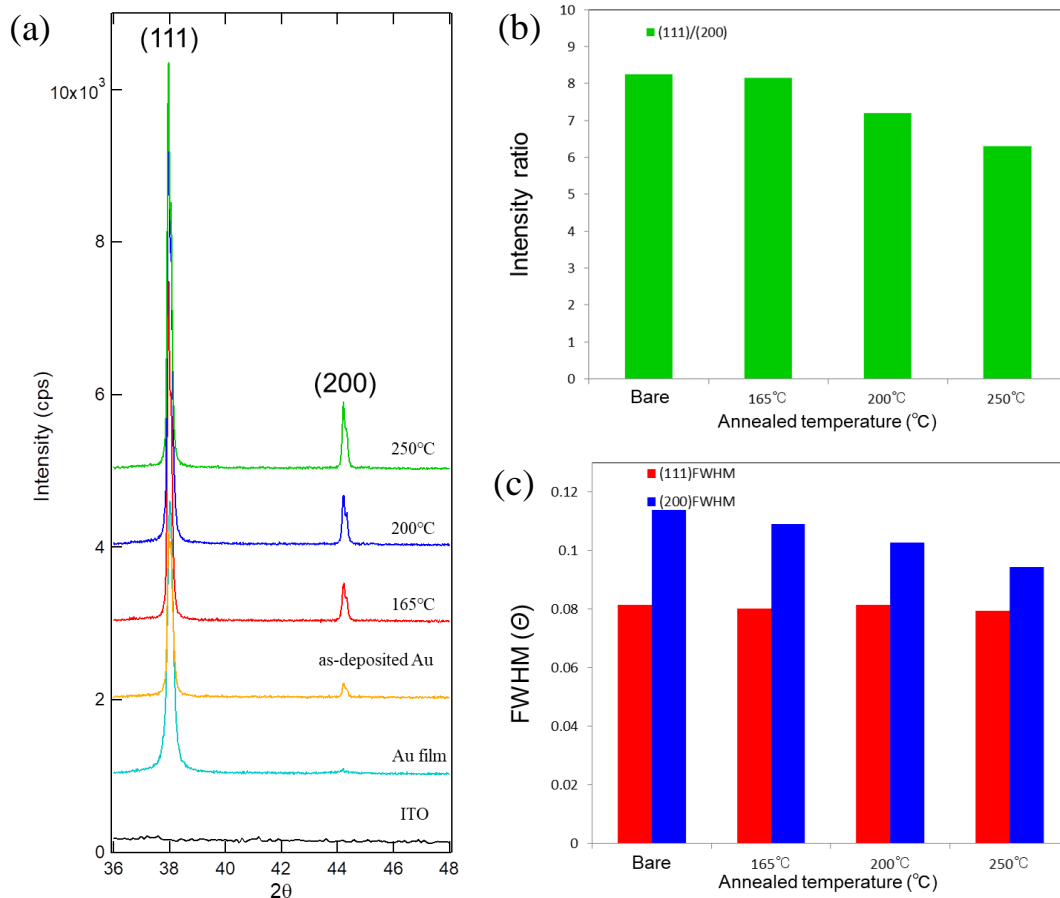


Figure 2-5. XRD measurement for annealed Au nanostructures. (a) XRD spectra for Au-NSL substrates annealed at a series of temperatures. (b) shows the diffraction intensity ratio of the (111) and (200) surfaces. (c) is the FWHM of (111) and (200) surface. From the Scherrer's rule,¹⁹ the sharpness of the XRD peak means that the corresponding crystal surface size is large. These data were obtained by computational analyzing the XRD peak due to the $K_{\alpha 1}$.

XRD provides crystal information on the Au nanoprism surface before and after annealing. In the XRD spectrum, the peak intensity ratio represents the ratio of crystal planes in the structure and the FWHM of a peak indicates the size of the corresponding crystal plane (Scherrer's rule¹⁹). Unlike the vapor-deposited Au thin film, multiple diffraction peaks were observed in the XRD spectrum of the Au nanoprism, indicating the polycrystalline surface (figure 2-5(a)). Diffraction peaks from the (111) and (200) planes were mainly observed in the Au nanoprism, and the intensity ratio

$(I_{(111)}/I_{(200)})$ tended to decrease with increasing the annealing temperature as shown in figure 2-4(b), meaning that increased the amount of (200) planes after annealing. Interestingly, the FWHM of the (200) diffraction peak decreased depending on the annealing temperature. This indicates that the crystal size of (200) plane increased, whereas the (111) plane showed no temperature dependence as can be found in figure 2-5(c). Thus, these behaviors indicate that a lot of the amorphous crystals were reconstructed to the (200) and/or (100) plane instead of the (111) plane. Since the annealing temperature is much smaller than the surface melting temperature of bulk, it is considered that amorphous crystals are likely to be priority reconstructed to the (200) plane where the phase transition energy of the surface is relatively smaller than (111) plane.

It has been found that the effect of grain boundaries on damping strongly depends on their orientation, their position along the particle length with respect to the plasmon resonance, and whether low or high-angle grain boundaries are present.²⁰ The crystallographic defect density can vary greatly between different types of grain boundaries. An isotropic Au having defect-free twin boundaries shows less damping than that having high-angle grain boundaries with crystallographic defects that act as scattering centers for electrons.²¹ Therefore, I considered that the large plasmon damping in as-deposited samples is predominantly due to the presence of high-angle grain boundaries of small amorphous crystal island. As grain boundary mobility increases with the degree of misorientation, so these high-angle grain boundaries are also most easily removed by annealing. The results of optical and surface analysis in my work suggest that the boundaries that remain are predominantly low-angled ones as

(100) and (111) that have little effect on plasmon damping. The annealed structures, while polycrystalline, are therefore optically indistinguishable from a single crystal.

2.3.4 Cu Under Potential Deposition on Au Nanoprisms

It can be expected that the electrochemical Cu UPD is the best analytical method for evaluating the crystal purity of the Au nanoprism surface because the co-adsorption potential of Cu is very sensitive to the type of crystals on the Au surface. The intensity of the adsorption current in the cyclic voltammogram (CV) depends on the crystal size and amount, and the waveform greatly depends on the purity of the crystal, which becomes broader on the amorphous surface. Cu UPD on annealed Au nanoprism was carried out in the electrolyte aqueous solution containing copper sulfate with three electrode cell. Figure 2-6 (a) shows the CVs acquired with the potential scan rate of 10 mV / sec. The broken lines in the figure indicate the co-adsorption of Cu on the surfaces (111) and (100). It was confirmed that the two adsorption peaks increased and became sharper as the annealing temperature increased. This implies that the small amorphous crystals are reconstructed to improve the purity of the crystals. Figure 2-6(b) shows the UPD current density ratio between the annealed and non-annealed Au nanoprism structures, enabling the quantitative evaluation of the crystal size and amount. One can see the dramatic increase of the current density ratio for (100) plane (up to 1.7 times), and slightly increasing of that for (111) plane via annealing (up to 1.2 times). However, this behavior was not observed in XRD spectra. These results come from electrochemistry which allows us to directly provide information on the surface of the gold electrode and the crystalline phase change that are too small to be detected by XRD. Particularly, the (100) plane is preferentially reconstructed, leading to the

improving the crystal purity of the surface. Therefore, it can be said that the improvement of the Q-factor by the low-temperature annealing where no structural change happens comes from the reconstruction of the crystal surface of the Au nanoprisms.

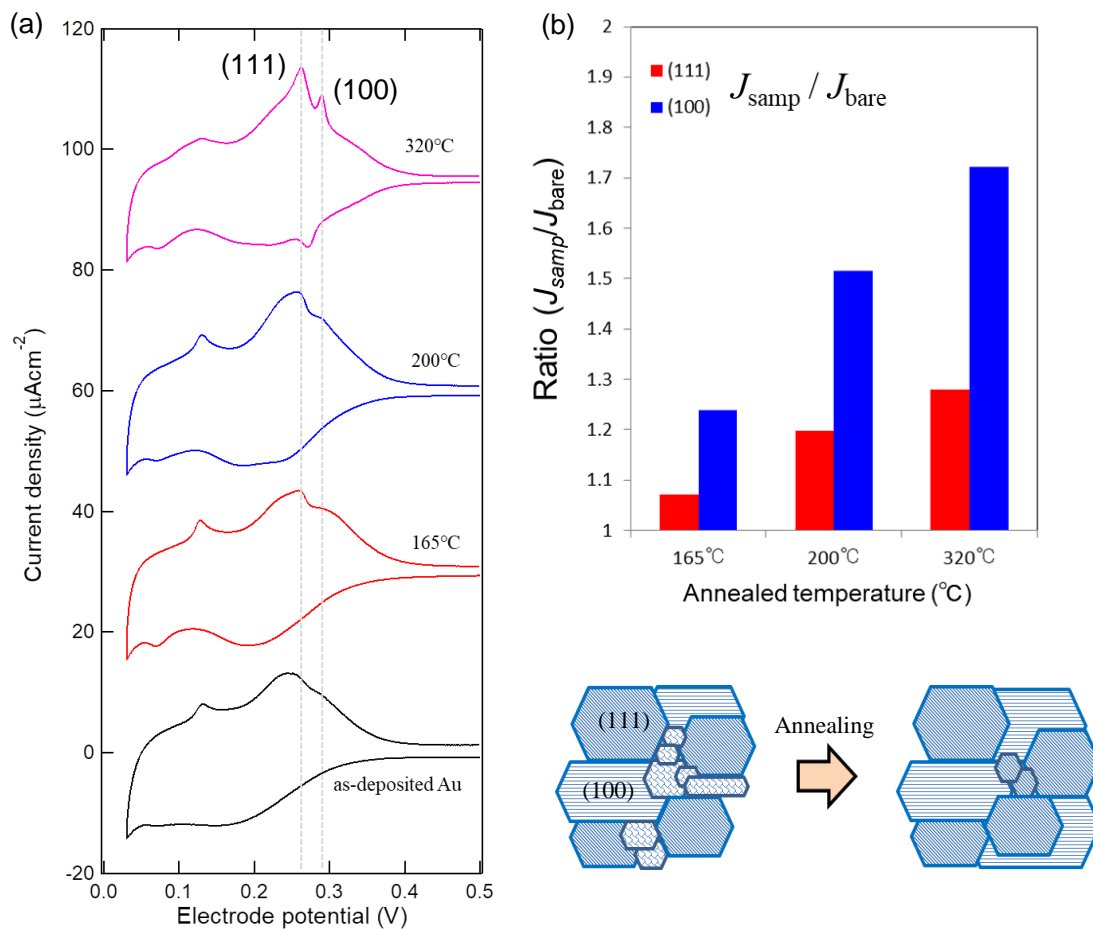
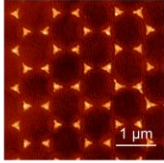
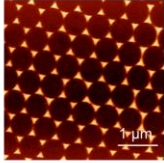
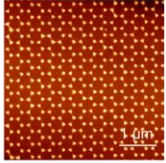
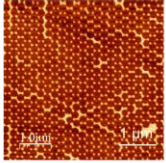



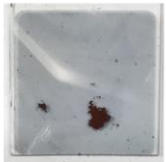
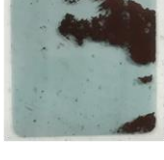





Figure 2-6 (a) Cyclic voltammogram for underpotential deposition (UPD) of copper on annealed and non-annealed Au nanoprisms in 0.1 M H_2SO_4 + 10 mM CuSO_4 solution. (scan rate 10 mV/s) (b) is the UPD current density ratio of that of the annealed sample to the that of the bare structure. The co-adsorption peak of (111) appears at + 0.27 V (vs. Ag/AgCl), while the co-adsorption peak of (100) appears at + 0.29 V (vs. Ag/AgCl). Bottom illustration shows the reconstruction of crystal plane before and after annealing

Table 2-2 Various Colorations of Au nanoprism fabricated with different size PS beads.

PS beads diameter	750 nm	500 nm	350 nm	200 nm
AFM image Before annealing				
Before annealing				
After annealing 200°C / 30min				

As shown in Table 2-1 by combining the particle size of the PS beads used in the mold and the annealing process, various colorings can be supported on the substrate. Before annealing, the LSP is excited in the near infrared, so it is colorless, but by annealing, the plasmon shifts to the visible region, resulting in a bright color (see figure 2-7). Since the shift width of plasmon can be freely controlled by the annealing time, it is expected to be applied to multicolor filters. This result is another powerful benefit provided by the annealing process.

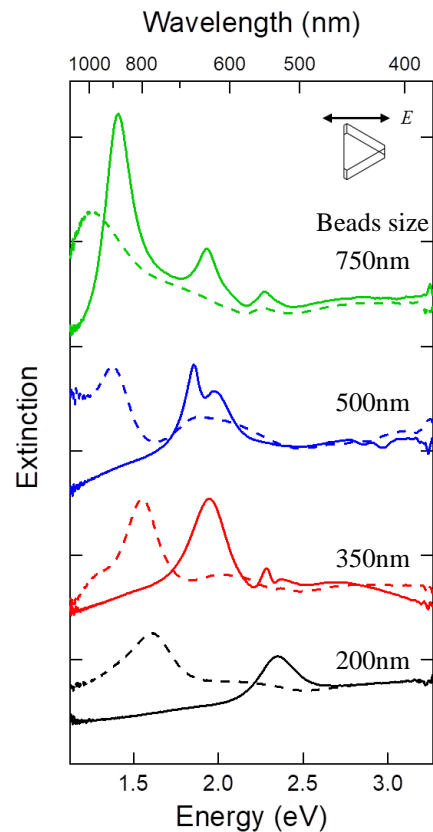


Figure 2-7 Extinction spectra of Au nanoprism fabricated with different size PS beads before (dash lines) and after (solid lines) annealing at 200°C for 30 min.

2.3.5 Improvement of Surface Lattice Resonance

Finally, I will introduce the noble application of low temperature annealing method into the lithographically-prepared well defined structure system. The surface lattice resonance (SLR) induced in the two dimensionally arranged metal nanodisk arrays has a higher Q factor than the single particle LSP due to the far field coupling between the LSPs. The metal nanolattice is mainly produced by the EBL method, but the non-uniformity of the geometric parameters, such as surface morphology or shape, reduced, leading the Q factor. From this point of view, the low temperature annealing method would have the possibility to improve the Q-factor of Au nanodisk arrays fabricated by EBL without changing the shape.

Figures 2.8(a)-(d) show the SEM and AFM images of the Au nanodisk arrays prepared by EBL, offering that the structural morphology does not change after low temperature annealing (at 200°C for 20 min). On the other hand, unlike the case of Au nanoprisms, Au nanodisk arrays showed sharper SLR spectra without significant shifting its peak position as shown in figure 2-8(e)-(g). The Q-factors of SLR which is known to depend on the lattice spacing has improved to the same level as previous reports. These behaviors support that the SLR is defined by diffracted scattered light and indicate that low temperature annealing only modifies the surface morphology and dramatically improves the quality and uniformity of the LSP. Surprisingly, the Q-factor of the Au nanodisk array with lattice space of 500 nm has improved by up to 5 times. This structure has a same or slightly wider FWHM than the narrow SLR. Thus, low temperature annealing method not only provides dramatic quality improvements for SLRs, but also promises to increase versatility of plasmonic crystal applications to various fields.

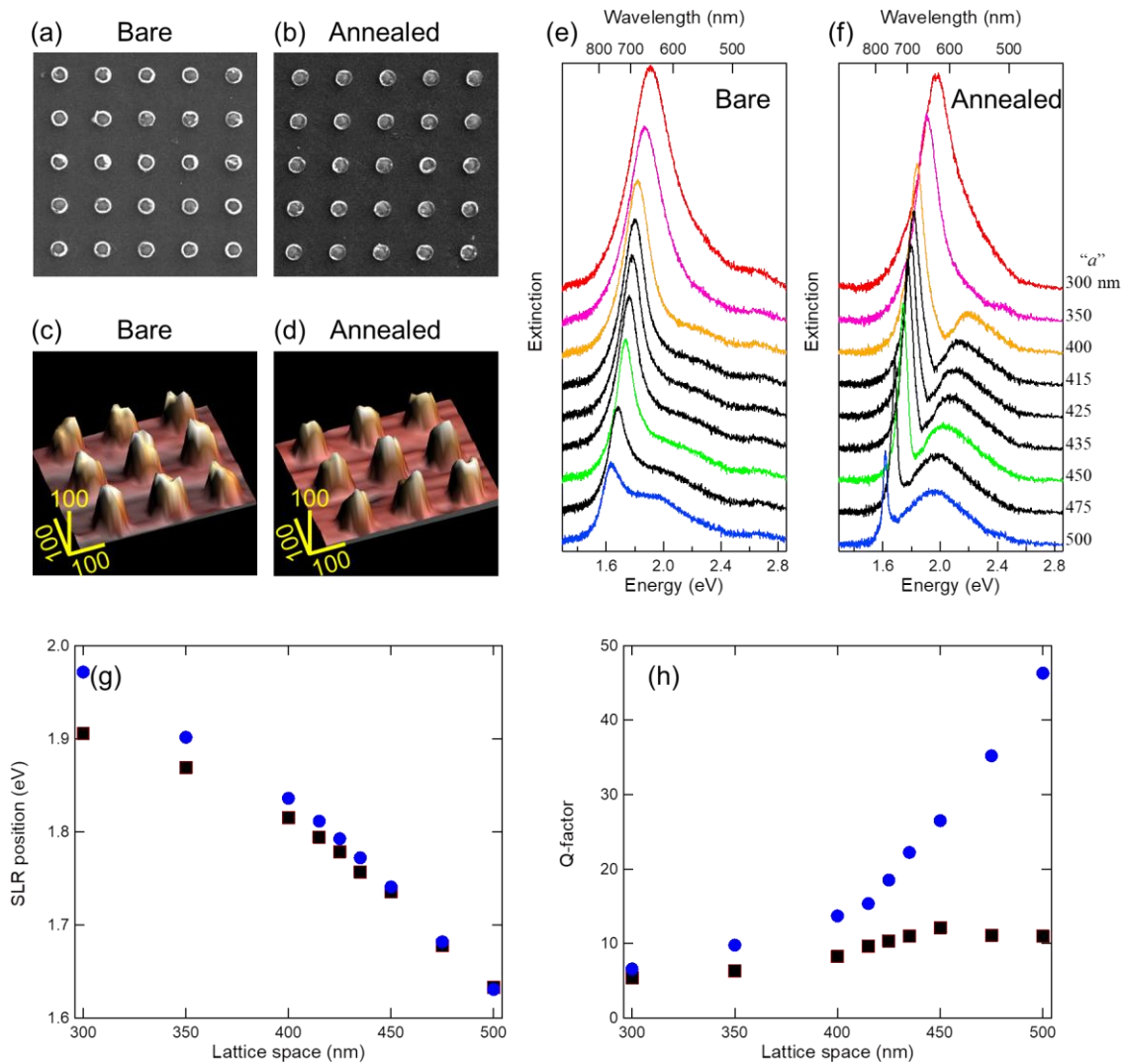


Fig.2-8 Structural and optical properties of square lattice of Au nanodisk arrays before and after annealing. (a–b) SEM and (c–d) AFM images of Au lattice structure with lattice space of 400 nm before and after annealing. Each scale size is unified. (e) and (f) show the normal incident extinction spectra before and after annealing (at 200°C for 20min), respectively. All spectra were collected in water to reduce the index mismatch. (g) and (h) are SLR peak position and Q-factor plot analyzed from the extinction spectrum. ■ and ● indicate the optical values before and after annealing, respectively.

2.4 Conclusion

In this section, I have proposed a facile process to improve the Q-factors of Au nanostructures fabricated by top-down lithography process. By annealing the Au nanostructures at the relatively lower temperature (i.e. lower than 200°C), it became possible to dramatically improve the Q-factor to a value equivalent to the simulated result without changing structural shape. XRD and electrochemical Cu UPD approaches revealed that small amorphous crystal islands having high-angle grain boundaries on the surface are reconstructed into low-angle grain boundaries (such as (100) and (111) planes) by annealing, resulting in improving the Q-factor due to reduced ohmic loss. Furthermore, the results of FDTD and experiments also suggest that the improvement of the adhesiveness between the adhered structure and the substrate contributes to the increase of the Q factor. Note, when the structures are annealed above 250°C, they show also dramatically improves the Q factor, but include the morphology changing. When low temperature annealing was applied to the Au nanodisk lattice structure, surprisingly, the Q factor was improved by up to 5 times without drastically SLR energy changes. Since SLR with a large Q factor provides high coherent light and a strong localized field, it is expected that the annealed Au lattice structure will form a weak or strong coupling with the matter such as dye excitons. These results provide design guidelines that indicate the dominant sources of damping for a given energy range, and will enable the fabrication of high Q-factor plasmonic resonators and antennas such as plasmonic crystals for developing plasmonic high sensitive sensor and laser, and multicolor device (see chapter 4-6).

2.5 References

- (196) Im H., Bantz K. C., Lindquist N. C., Haynes C. L. and Oh S. H. *Nano Lett.* **10**, 2231–2236 (2010).
- (197) Duan H., Hu H., Kumar K., Shen Z. and Yang J. K. W. *ACS Nano*, **5**, 7593–7600 (2011).
- (198) Duan H., Hu H., Hui H. K., Shen Z. and Yang J. K. W. *Nanotechnology*, **24**, 185301 (2013).
- (199) Nagpal P., Lindquist N. C., Oh S. H. and Norris D. J. *Science*, **325**, 594–597 (2009).
- (200) Chen K. P., Drachev V. P., Borneman J. D., Kildishev A. V. and Shalaev V. M. *Nano Lett.*, **10**, 916–922 (2010).
- (201) Sambles J. R. *Solid State Commun.*, **49**, 343–345 (1984).
- (202) Habteyes T. G., Dhuey S., Wood E., Gargas D., Cabrini S., Schuck J. P., Alivisatos P. A. and Leone R. S. *ACS Nano*, **6**, 5702–5709 (2012).
- (203) Liu Z., Boltasseva A., Pedersen H. R., Bakker R., Kildishev V. A., Drachev P. V. and Shalaev M. V. *Metamaterials*, **2**, 45–51 (2008).
- (204) Sönnichsen C., Franzl T., Wilk T., Plessen G., Feldmann J., Wilson O., and Mulvaney P. *Phys. Rev. Lett.*, **88**, 077402 (2002).
- (205) Zhang L., Chan C. Y., Li J. and Ong H. C. *Opt. Express*, **20**, 12610–12621 (2012).
- (206) Critchley, K. Khanal P. B., Gorzny L. M., Vigderman L., Evans D. S., Zubarev R. E., Kotov A. N., *Adv. Mater.*, **22**, 2338–2342 (2010).
- (207) Huang, J. S., Callegari V., Geisler P., Brüning C., Kern J., Prangma J. C., Wu X., Feichtner T., Ziegler J., Weinmann P., Kamp M., Forchel A., Biagioni P., Sennhauser U. and Hecht B. *Nat. Commun.*, **1**, 150 (2010).
- (208) Jung Y. S., Sun Z., Kim H. K. and Blachere J. *Appl. Phys. Lett.* **87**, 263116 (2005).
- (209) Tinguely, J. C., Sow I., Leiner C., Grand J., Hohenau A., Felidj N., Aubard J. and Krenn J. R. *BioNanoSci.*, **1**, 128–135 (2011).
- (210) Michel B., Lei Z., Huigao D., Shu F. T., Christian A. N., Cheng-Wei Q. and Joel K. W. *Y. Scientific Reports*, **4**, 5537 (2014).
- (211) Liu H., Wang B., Leong E., Yang P., Zong Y., Si G., Teng J., and Maier S. A. *ACS Nano*, **4**, 3139–3146 (2010).

- (212) Sawai Y, Takimoto B, Nabika H, Ajito K and Murakoshi K. *J. Am. Chem. Soc.*, **129**, 1658-1662 (2007).
- (213) Nagasawa F, Takase M and Murakoshi K. *J. Phys. Chem. Lett.*, **5**, 14–19 (2014).
- (214) Scerrer P. *Nachr. Ges. Wiss. Göttingen.*, **26**, 98–100 (1918).
- (215) Bietsch A. and Michel B. *Appl. Phys. Lett.*, **80**, 3346–3348 (2002)
- (216) Bosman, M. et al. *Sci. Rep.*, **3**, 1312 (2013).
- (217) Lee, J. Hwang, S. Lee, H. Kwak, J. *J. Phys. Chem. B*, **108**, 5372–5379 (2004).
- (218) Magnussen, O. M. et al. *Phys. Rev. Lett.*, **64**, 2929–2932 (1990).
- (219) Magnussen, O. M. *J. Vac. Sci. Technol. B Microelectron. Nanom. Struct.*, **9**, 969 (1991).
- (220) Moller A. F. et al. *Phys. Rev. B*, **51**, 2484 (1994).
- (221) Saito K and Tatsuma T. *Nanoscale*, 48 (2015)

Chapter 3

Electrochemical Structure Control for Ultimate Light Confinement

3.1 Introduction

The plasmon-induced electromagnetic fields are often preferred to enhance the light-matter interactions. As I mentioned in section 1.3, the metal nanodimer structure separated by several nanometers induces a various type of hybridized plasmon modes from visible to near infrared range, depending on its interparticle gap distance.¹⁻⁶ The most notable property is the enhanced electromagnetic field induced in the gap. The Q factor is not so large because it is limited to the dielectric function like a single particle. The localized near field at the gap can be enhanced to several hundred times than that of a single particle. Thus, its property has been offered for the noble application in various research fields. Recent studies have shown that the dipolar interaction at sub-nanometer (less than 1 nm) allows the formation of higher-order plasmon such as bonding quadrupolar plasmon (BQP) which is optically dark.^{4,6} Because a dark mode has a longer lifetime of the excited state compared with a that of the bright mode, it can further enhance the local field, and would be dramatically improving the light-matter interactions. If one can control the excitation of the higher-order multipolar plasmon modes, advantages for various applications of the LSPR field could be promised. So far, several noble techniques including electron beam lithography, scanning probe manipulation, molecular cross linking and chemical synthesis,^{5,7-9} have already achieved the structural resolution down to the molecular

scale, leading to the BQP excitation. However, such outstanding technologies have the difficulties in mechanical operability. Therefore, there seems to be still a room for improvement in terms of operability or reproducibility to prepare well-defined gap structures.

Recent works have demonstrated that electrochemical methods, which can control both the free electron densities and the geometrical structures of metals, are quite effective for precise control of the plasmonic properties.¹⁰⁻¹⁵ In this chapter, I have demonstrated the flexible tuning of the dimer plasmon mode using electrochemical metal dissolution and deposition reaction. First, nanometer-order structural control was demonstrated by oxidizing the gold nanoprism dimer structure in electrochemical. It was proved that the quenching spectral intensity obtained during oxidative dissolution and the dissolved volume had a linear relationship. In addition, this method has been applied to sub-nanometer structural control of well-defined dimer structures. The plasmonic property changes of single Au nanodimers during the electrochemical dissolution reaction were monitored via *in-situ* dark-field microscopic scattering measurements. Through precise control of the dimer structures under appropriate electrochemical conditions, the plasmon mode transition from bonding mode to BQP was successfully observed. Finally, the structural control resolution was extended to the monatomic level by using the UPD of Cu. It is very surprising that the optical spectrum was modulated even with atomic-level gap changes. The method and phenomena presented here will be useful in the preparation of plasmonic structures for ultimate light confinement applications.

3.2 Experimental Method

3.2.1 Sample Fabrication

Au nanoprism dimer and Au nanodisk array dimers with various gap distances were fabricated on ITO-coated glass slide substrate by AR-NSL and EBL. The sample preparation procedure was same as that in section 2.2.1. In the experiment of the structure made by EBL, the gap was defined as the interparticle distance d , as shown in Figure 3-1 (a). The particle diameter and height are 125 and 50 nm, respectively.

3.2.2 Electrochemical Extinction Measurements

The Au nanostructures were evaluated by scanning electron microscopy (SEM) before and after electrochemical measurements. Extinction spectrum measurements in the visible to near-infrared region were conducted using a multichannel spectrometer (MCPD-2000, Ohtsuka Electronics). The prepared Au nanostructures supported on the conductive substrate were used as a working electrode for electrochemical measurements. The counter and reference electrodes were a Pt plate and Ag/AgCl, respectively. Electrochemical measurements were performed using an automatic polarization system (Hokuto Denko, HSV-100). The electrolyte for the electrochemical oxidation reactions was an aqueous solution of KCl (10 or 50 mM).

3.2.3 Electrochemical Dark-field Spectroscopic Measurements

The electrochemical dark-field spectroscopic measurements were performed using an inverted microscope. Electrochemical Au dissolution was performed in a 10 mM KBr contained 0.1 M NaClO₄ aqueous solution. The electrochemical cell consisted

of the ITO substrate, a Pt coil and an Ag/AgCl electrode, which played as the working electrode (W.E.), the counter electrode (C.E.), and the reference electrode (R.E.), respectively. Figure 3-1(c) shows the cyclic voltammogram for Au wire obtained in the prepared solution. The oxidation current at more positive than 0.7 V is corresponding to the dissolution of Au. From this voltammogram, I have decided the applying potential for the dissolution experiment. The inverted microscope was equipped with a 100 W halogen lamp, a dark field condenser and a 60×/0.7 numerical aperture (NA) dry objective lens (IX-71, Olympus Co.). The angle of incidence of the light onto the structure was 43°. The light source for measurements was a halogen lamp (100 W) with controlled attenuation, resulting in a negligible temperature increase under the illumination less than the order of kW cm^{-2} in an aqueous electrolyte solution. The dark-field scattering spectrum was collected from each isolated single nanostructure. Pure single nanoparticle scattering spectra were acquired using a high-sensitivity spectrometer (IsoPlane SCT-320, Princeton Instruments). An illustration of the experimental set-up is shown in figure 3-1.

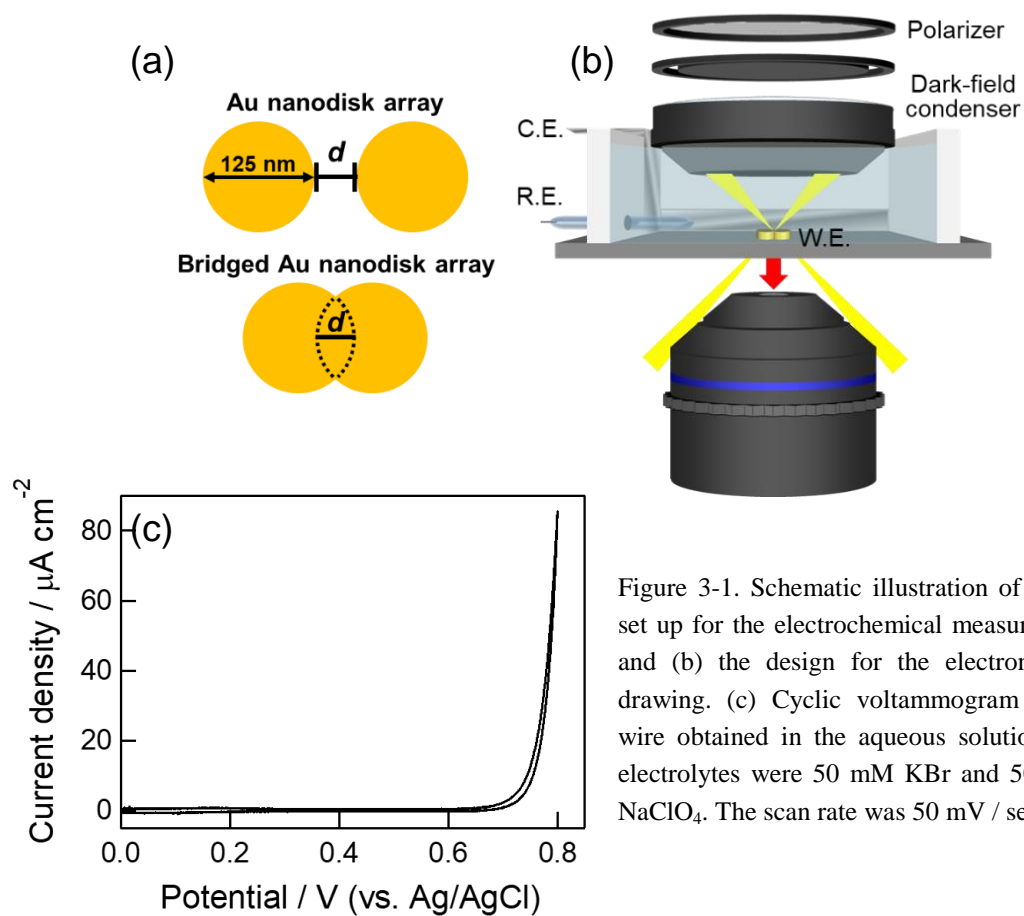


Figure 3-1. Schematic illustration of (a) the set up for the electrochemical measurements and (b) the design for the electron beam drawing. (c) Cyclic voltammogram of Au wire obtained in the aqueous solution. The electrolytes were 50 mM KBr and 500 mM NaClO₄. The scan rate was 50 mV / sec.

3.2.4 Electric Field Simulations of the Au Nanodisk Array

Three-dimensional FDTD simulations were performed using commercial software (EEM-FDM, EEM Co.). A uniform mesh size was set at 0.2 nm (in the x, y and z directions). The perfectly matched layer (PML) was adopted as a boundary condition. The optical constants of gold were taken from previously documented data within the spectral range from 500 nm to 800 nm.

3.3 Results and Discussion

3.3.1 Nanoscale Control of Au Nanoprisms Gap via Electrochemical Gold Dissolution

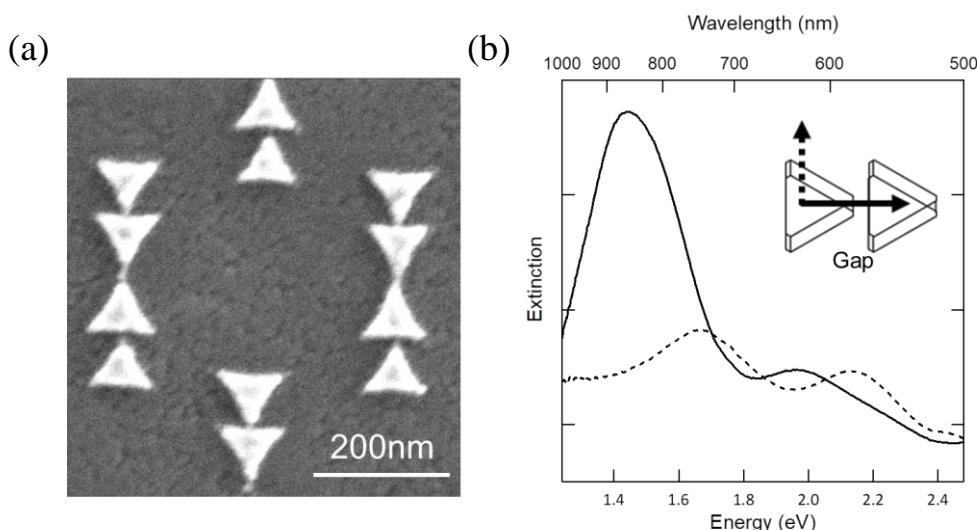


Figure 3-2. (a) SEM image of Au nanoprism dimer structures supported on a conductive glass substrate prepared by AR-NSL method. (b) Extinction spectra of Au dimer structures measured in air. The solid and broken lines correspond to the polarized incident light parallel and perpendicular to the long axis of the dimer, respectively.

Well-defined Au nanoprism dimer structures were prepared on a conductive glass substrate by AR-NSL method, as shown in figure 3-2(a). The well-ordered metal nanostructures showed a broad plasmon resonance peak at around 1.38 eV under polarized light irradiation parallel to the long dimer axis, as illustrated in figure 3-2(b). When the polarized light was perpendicular to the long dimer axis, relatively weak features were observed around 2.07 eV. The strong plasmon resonance peak in the parallel polarization is attributed to the bonding dipolar plasmon mode, which is excited by the dipole–dipole interaction of the dimer. The polarization dependence of the plasmon resonance wavelength shift is caused by the different dipole–dipole interactions under different polarization.^{3,16} The relatively broad feature reflects the

interaction between the dimer structures.^{17,18} These optical characteristics of the bonding dipolar plasmon indicate the structural anisotropy of the dimer structures with a gap distance of a few nanometers. In the present system, the gap is defined by the space between the tip of one triangular nanoparticle and the base of another triangular nanoparticle. It has been reported that this gap distance is sensitive to the peak wavelength of the extinction spectrum.¹⁸⁻²⁰ With the increase of the gap distance at nanoprism dimer, the dipolar coupling become weaker and, thus, the plasmon resonance wavelength shift to the shorter wavelength.

In situ spectroscopic measurements of the Au dimer structures were carried out to monitor the change in their polarized extinction spectrum as functions of electrochemical potential and polarization time. At positive electrode potential exceeding 0.80 V, Au dissolution proceeds in KCl aqueous solution.²¹ Thus, I applied electrode potentials of 0.80, 0.87, and 0.89 V to evaluate the effect of the Au dissolution rate on the dimer optical properties. Time dependent extinction spectra obtained under potential polarization for 600 s using polarized light parallel and perpendicular to the long axis of dimer are presented in the upper and bottom rows of figure 3-3, respectively. At 0.80 V, which is at slightly more negative potential than that of apparent Au dissolution, no spectral change was observed under both parallel and perpendicular polarization, as shown in figure 3-3(a). At 0.87 and 0.89 V, changes in the extinction spectra were observed. In the case of 0.87 V, the peak wavelength of the spectrum shifted to shorter wavelength, especially for the parallel polarization (figure 3-3(b) upper) compared with that for the perpendicular case (figure 3-3(b) bottom). With the decrease in the volume of triangular nanoparticle, the gap at the dimer may vary to change the bonding dipolar plasmon mode. Considerable changes both in the peak

wavelength as well as the intensity of the extinction were observed at 0.89 V, especially after 100 s (figure 3-3(c)). The intensity of the plasmon resonance peak decreased faster at 0.89 V than that at 0.87 V. These changes are induced by the structural changes of the Au dimers caused by electrochemical dissolution reactions. The dependence of spectral changes on potential may reflect the distinct Au electrochemical dissolution rates exponentially accelerated from 0.87 to 0.89 V.

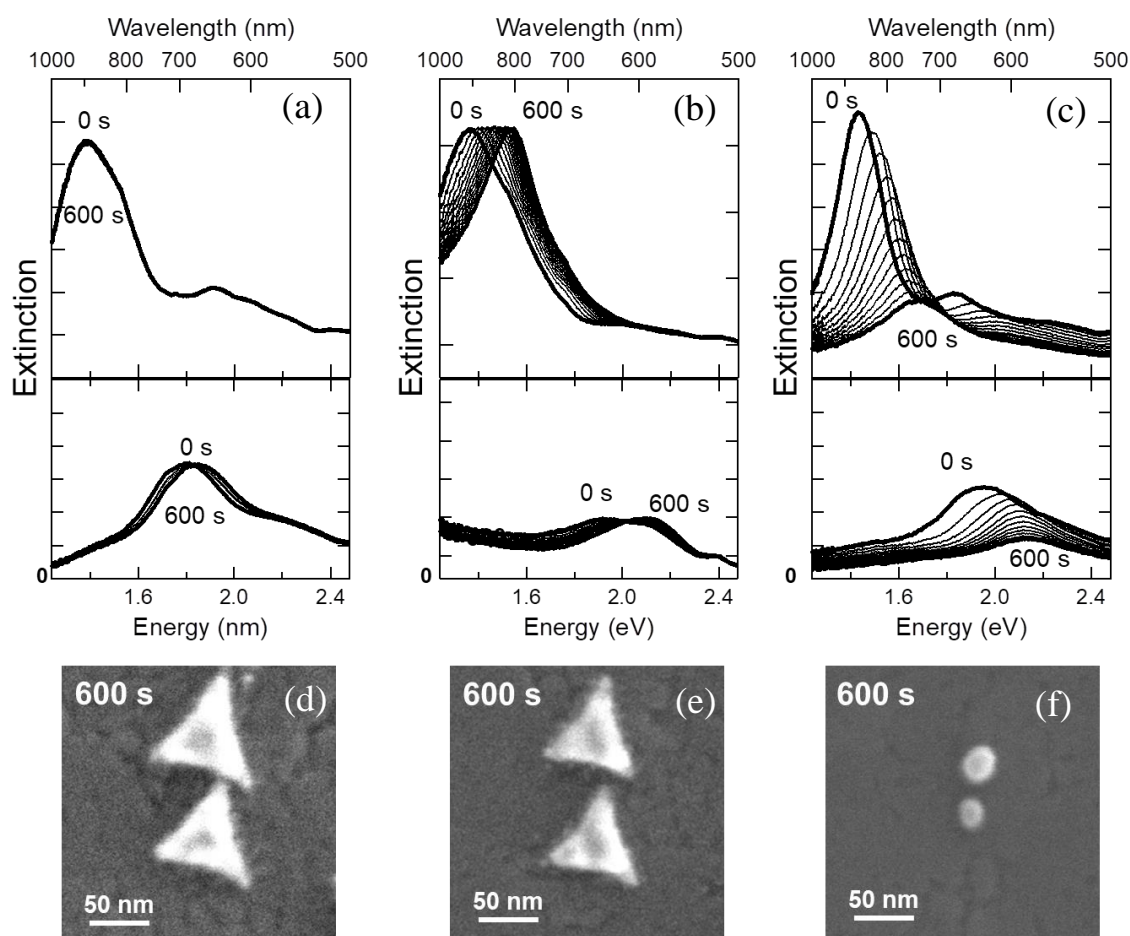


Figure 3-3. (a) Time-dependent electrochemical extinction spectra of Au dimer structures obtained after applying electrode potentials of (a) 0.80, (b) 0.87, and (c) 0.89 V in (a) 50 and (b), (c) 10 mM KCl. The upper and lower columns correspond to the polarized direction parallel and perpendicular to the long axis of the structures, respectively. Potential was applied for 600 s. SEM images of Au dimer structures after 600 s of electrochemical dissolution at (d) 0.80, (e) 0.87, and (f) 0.89 V.

SEM was used to confirm the changes in the structures of the Au dimers. SEM images in the bottom row of figure 3-3 show the Au nanostructures after the observation of their spectral changes. While the structure after applying potential of 0.80 V did not show apparent change from that before measurements, the size of the structures after keeping at 0.87 V slightly decreased. As the size of triangular nanostructures decreased, their gap distance increased to ca 10 nm. After dissolution at 0.89 V, much of the Au nanostructures had dissolved, leading to the formation of rounded dimers composed of particles with diameters of 20–30 nm separated by more than 15 nm. These observations prove that the dependence of the rate of the nanostructure optical property changes on electrode potential reflects the structural changes induced during dissolution at the respective potential.

In time-dependent electrochemical extinction spectra of the nanostructures, both decreasing scattering intensity and a plasmon resonance wavelength shift were clearly observed (figure 3-3). These variations are derived from the change in dimer structure during electrochemical polarization. When the shape of triangle becomes rounded, the plasmon resonance wavelength shifts to shorter wavelength.^{22,23} In addition, as the gap distance of Au dimer arrays increases, their plasmon resonance wavelength shifts to shorter wavelength, and the intensity of the plasmon resonance peak decreases with the volume of the metal structure.^{16,24,25} Particularly under light irradiation perpendicular to the long axis of the structures, the intensity change would reflect only the volume change because of the weak dipole–dipole interaction between nanostructures.^{16,25} Thus, the present results would imply not only the decrease in the volume of the metal nanostructures but also the increase of their gap distance.

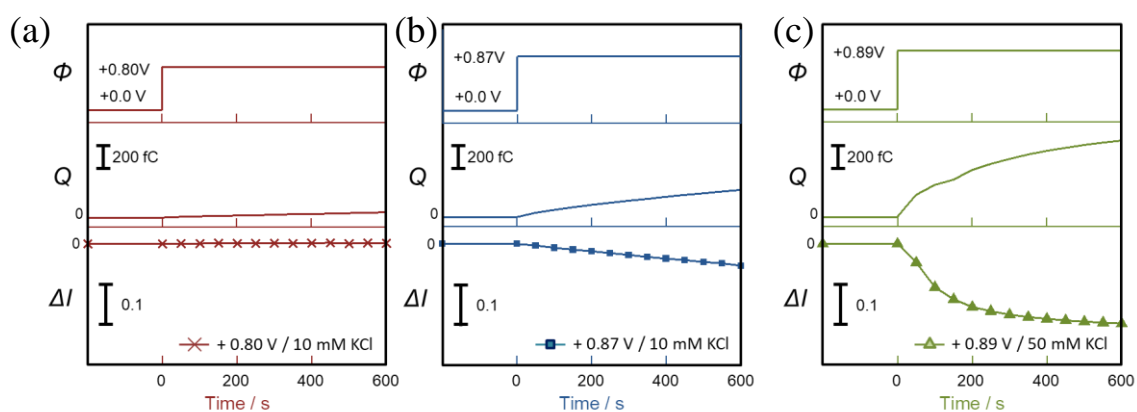


Figure 3-4. Time series plots of (upper) applied electrode potential, (middle) charge, and (bottom) the integral intensity change of the scattering cross section divided by the initial integral obtained with an applied potential of (a) 0.80, (b) 0.87, and (c) 0.89 V.

Here, the correlation between the electrochemical dissolution and structural change of the nanostructures is discussed by comparing the charge (Q) of the oxidative dissolution and changes in optical properties. Figure 3-4 presents the chronoamperometry results obtained at each electrode potential. From the observed currents and the estimated number of the dimer structures in the observed area, Q of the oxidation reaction per Au nano-dimer was estimated. To discuss the change in optical properties, the integrated scattering intensity which indicates the volume of observed metal structures after applying potential for t s was normalized to the initial integrated scattering intensity to obtain $I(t)/I_0$ (figure 3-4). These integrated scattering intensity changes were collected from extinction spectra obtained under the light illumination polarized to the long axis direction. No change of $I(t)/I_0$ was observed without applying electrode potential. Although the time-dependent changes in Q and $I(t)/I_0$ were negligible at 0.80 V, they became apparent at 0.87 and 0.89 V. As mentioned above, the change in $I(t)/I_0$ directly reflects the volume change of Au nanostructures. The difference in the change rate of $I(t)/I_0$ can be considered as the dependence of the

volume decreasing rate for the Au nanostructures on the electrode potential. These changes correlated well with the observed time-dependent change of Q .

To further analyze these results, $I(t)/I_0$ are plotted against Q in figure 3-5(a). The slopes of the plots change after $Q = 6.9 \times 10^{-13}$ C per nanodimer, which corresponds to 100 s of electrochemical polarization at 0.89 V. The slope of the data obtained at an electrochemical polarization of 0.87 V for $Q = 5.9 \times 10^{-13}$ C per nanodimer is comparable to that of the initial slope of the data measured at 0.89 V. The important point here is that the integrated scattering intensity depends on the volume of metal nano-structure.^{25,26} The difference of the slopes suggests that there is an essential difference in the plasmonic optical properties of the nanostructures caused by the structural change after dissolution at $Q = 6.9 \times 10^{-13}$ C per nano-dimer. Figures 3-3(b) and (c) clearly revealed different tendencies of the maximum plasmon resonance wavelength shift under electrochemical polarization at 0.87 and 0.89 V, respectively. At 0.87 V, the maxima of the extinction spectra shifted to shorter wavelength as the electrochemical dissolution progressed, while the maximum scattering intensity did not change much (figure 3-3(b)). These spectral changes showing relatively slow rate could be derived from slight changes in the gap distance between nanostructures that retained their triangular shapes, as confirmed by the SEM image in figure 3-3(e).^{18,27} Based on these characteristics, it is expected that the relatively slow dissolution at 0.87 V allows precise control of the gap distance, providing Au nanodimer structures with well-defined plasmonic properties.

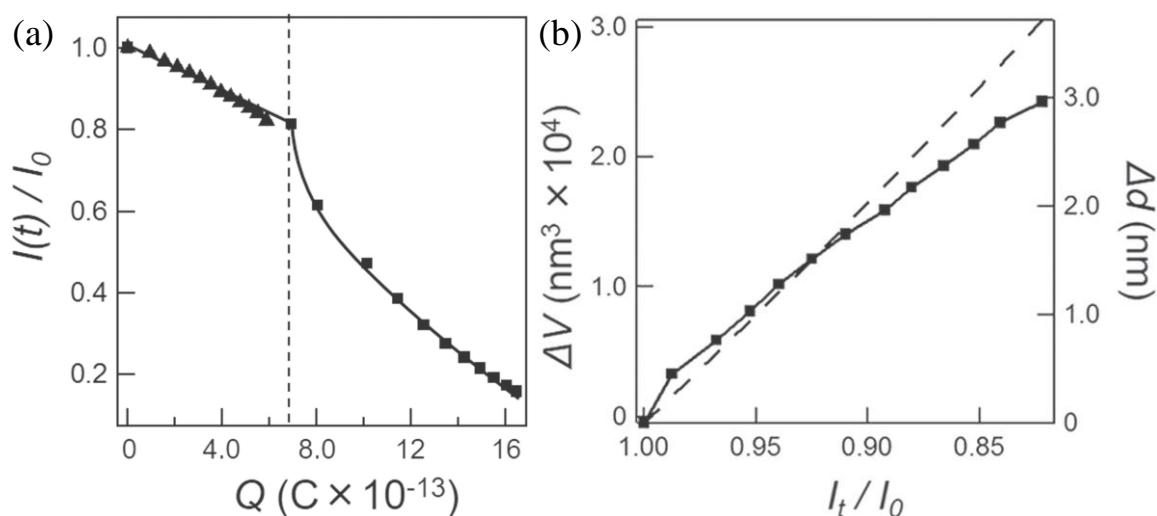


Figure 3-5. (a) Plots of $I(t)/I_0$ as a function of Q per nanodimer. Triangle and square plots correspond to applied potentials of 0.87 and 0.89 V, respectively. (b) ΔV_{EC} and Δd_{EC} determined by the electrochemical measurements as a function of $I(t)/I_0$ at 0.87 V (square plot with solid line); and ΔV_{opt} and Δd_{opt} determined by the optical measurements using $I(t)/I_0 = 0.822$ giving $\Delta V_{opt} = 2.96 \times 10^4 \text{ nm}^3$ and $\Delta d_{opt} = 3.72 \text{ nm}$ (broken line).

To quantitatively evaluate the change in the structure volume which leads to the gap distance change of the nanodimers at 0.87 V, the correlation between volume changes estimated from Q and $I(t)/I_0$ was examined. The present electrochemical dissolution reaction of Au is the one-step threeelectron oxidation process²¹; $\text{Au} + 4\text{Cl}^- \rightarrow \text{AuCl}_4^- + 3e^-$. Based on the chronoamperometry at 0.87 V, Q after 600 s indicates that the amount of Au dissolved in the reaction is 2.0×10^{-18} mol. The optical absorption of relatively small amount of $[\text{AuCl}_4]^-$ ion, whose absorption maximum at around 2.38 eV, did not affect the spectral observation as confirmed in figures 3-3(b) and (c).²⁸ If I assumed homogeneous dissolution of the Au nanodimer structure consisting of two equilateral triangles positioned in a line, estimated changes in volume from the amount of Au dissolved in the reaction by the electrochemical measurements can give the volume change (V_{EC}) and the gap distance (Δd_{EC}). The average height and side length of each Au triangular nanostructure were 30 and 80 nm, respectively. From the volume

change, $\Delta V_{EC} = 2.4 \times 10^4 \text{ nm}^3$, the change in the gap distance, Δd_{EC} , after 600 s can be regarded as 2.96 nm.

In addition to Q , $I(t)/I_0$ determined by the optical measurements can also give ΔV_{opt} and Δd_{opt} based on the assumption that the scattering intensity changes are solely attributed to the decrease in the volume caused by dissolution. This assumption is supported by the linear relationship between $I(t)/I_0$ and $V(t)/V_0$ at 0.87 V. Validity is also supported by the SEM images in figures 3-3(a) and (b). Comparable values of Δd_{EC} and Δd_{opt} shown in figure 3-5(b) proves successful control of the optical properties of the dimer through the precise tuning of the gap in the present system. It should be noteworthy that larger volume dissolution at 0.89 V than that at 0.87 V results in the nonlinear relation between $I(t)/I_0$ and $V(t)/V_0$ in figures 3-5(a). In this case, the estimation of the gap distance based on the optical measurement becomes inaccurate. Generally, edge part of metal nanostructure shows faster electrochemical dissolution due to the localization of electric field under the electrochemical polarization. Acceleration of the dissolution rate at 0.89 V compared with that at 0.87 V results in apparent inhomogeneous dissolution giving rounded dimer structure as shown in figure 3-3(f).

These results reveal that a change in gap distance of 2.96 nm was achieved by the present electrochemical method through slow metal dissolution for 600 s at 0.87 V. In the present system, the rate of surface dissolution is estimated to be 0.30 nm min^{-1} , corresponding to the average rate of a single atomic Au layer for 60 s. Slight deviation of the plots from dotted line showing nonlinear behavior in figure 3-5(b) could originate from the change in the extinction spectrum of the dimer, reflecting not only the volume but also anisotropic shape at the gap. It should be considered that the electrochemical

reaction proceeds on the nano-structure may lead to the formation of an anisotropic shape. Thus, the present assumption based on the expectation of the uniform dissolution could be too simplified. However, relatively good agreement between the values of Δd determined by individual optical and electrochemical observations proves the validity of the present estimation. Further detailed analysis considering the quantum-scale optical characteristics of the nanostructures may offer a more quantitative understanding of their behavior on the ultra-small scale. Next, by extending this system to a scattering measurement system and a single particle measurement system, the fine control of gaps and the accompanying transition of plasmon mode were investigated.

3.3.2 Dark field imaging during electrochemical Au dissolution

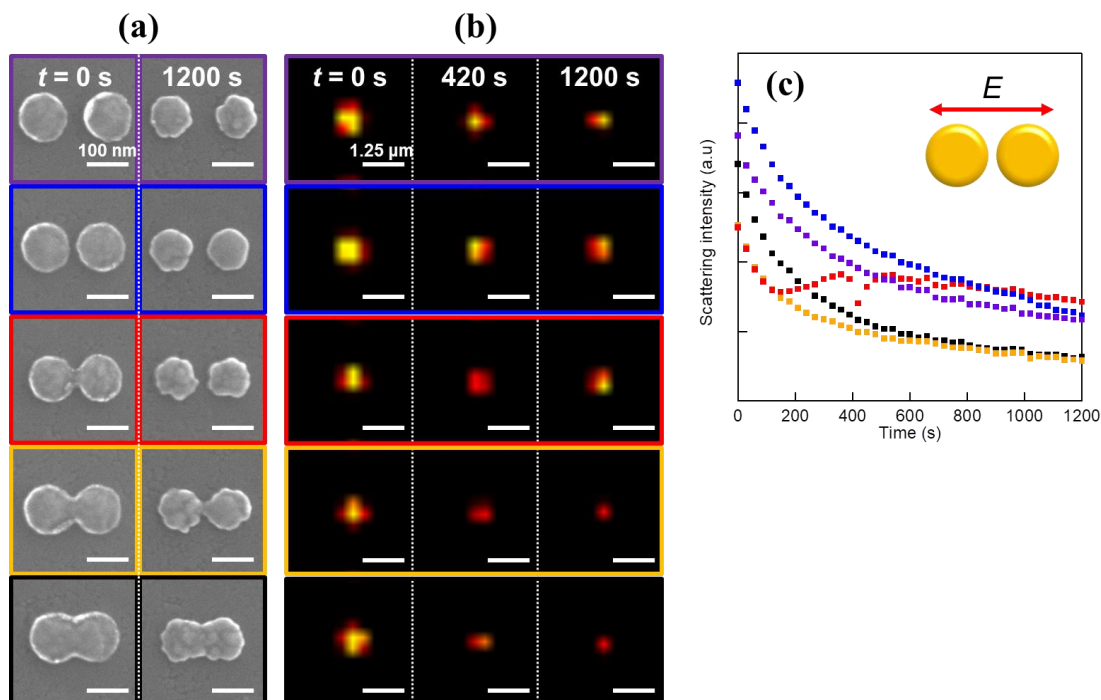


Figure 3-6. Single particle dark-field scattering properties of bridged Au nanodisk dimers in the visible and NIR regimes. Thickness is 50 nm and radius of single Au nanodisk is 75 nm. (a) SEM images of Au nanodisk arrays with the gap distance -30 nm (black), -20 nm (orange), -5 nm (red), 10 nm (blue) and 30 nm (violet), were obtained before (left) and after dissolved the Au nanodisk arrays (right) at +0.74 V in 10 mM KBr aq.. (c) time series of scattering intensity changes of single Au nanodisk array

Various bridged and nonbridged Au nanodisk arrays were fabricated by the electron beam lithography method as shown in the left panel of figure 3-6(a). The designed diameter of the Au nanodisk and the thickness for all structures were set at 125 and 50 nm, respectively. The interparticle distances between the two disks (represented as ' d ' shown in figure 3-1(a)) in the structures were -30, -10, -5, 10, and 30 nm, ranging from bottom to top. Scattering images of each structure were obtained via dark field microscopy under longitudinal polarized light illumination (see the right panel of Fig. 3-6(a)). Clearly, the scattering properties of the Au nanodisk are strongly dependent on the value of d . The scattering intensities of the nonbridged structures become

relatively stronger than those of the bridged structures. The inhomogeneous scattering intensity from one spot would reflect the different plasmon mode or the surface roughness of the structure.²⁹ During these measurements, the scattering spectra were also obtained (see figure 3-7).

As shown in the scattering spectra for each of the structures shown in figure 3-7, the Au nanodisk arrays have clear anisotropic scattering properties that are dependent on the light polarization direction. Under the condition of transverse polarization, no clear d -value dependence appeared in the scattering spectra, while the scattering properties were quite sensitive to changes in d for the longitudinal polarization case. When d increased from -30 to -5 nm, the

intensity of the peak at the lower energy decreased, while the intensity of the peak in the higher energy region increased. The lower energy mode disappeared at d values of more than -5 nm. The higher mode shifted from 2.2 to 1.7 eV as d changed from -30 to 10 nm and then increased to 1.8 eV following a 20 nm increase in d . Regarding to the optical properties of the dimer, I have checked the high reproducibility by preparing many structures with the same structure preparation procedure.

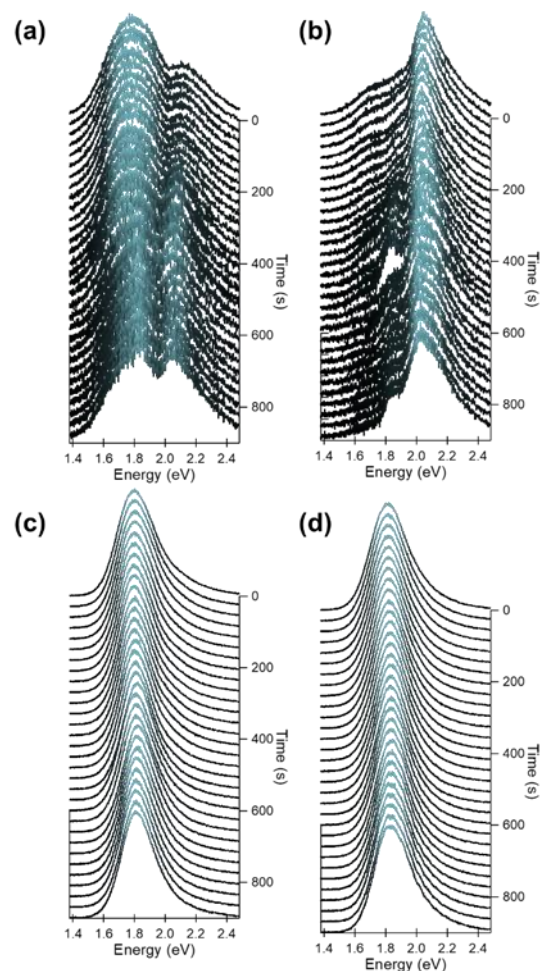


Figure 3-7. Polarized scattering spectra for Au dimer structures with various d values obtained during the electrochemical potential polarization. The polarization direction of the incident light was parallel to the long axis of the dimer. The electron beam drawing designs for each structure were (a) -30 , (b) -10 , (c) 10 , and (d) 30 nm, respectively.

Using these Au structures, tuning of the plasmonic properties was conducted during the electrochemical dissolution reactions under a static potential of 0.74 V in an aqueous solution that contained 10 mM KBr and 0.1 M NaClO₄ (see figure 3-1(c)). The left and middle panels of figure 3-6(b) show the scattering images of each structure at the potential polarization times of 420 and 1200 s, respectively. SEM observations of all structures were also conducted after electrochemical potential polarization for 1200 s, as shown in the right panel of figure 3-6(b). Figure 3-6(c) shows the plots for the time series scattering intensity changes for all structures which were obtained during the electrochemical measurements as a function of the electrochemical dissolution time. As shown in the plots, the scattering intensity decreased as the electrochemical dissolution progressed, which led to a reduction in the volume of the structure. The homogeneous dissolution of the Au surface leads to an exponential decrease of the volume, resulting in an exponential decrease of the scattering intensity. The reductions in the scattering intensities by 30–40% after 1200 s agree roughly with the estimated volume of the dimer structure after dissolution. SEM images obtained after potential polarization for 1200 s (shown in the right panel of figure 3-6(b)) have also confirmed these apparent reductions in volume. SEM images have demonstrated that the homogeneous dissolutions required to retain the disk-shaped structures of the dimers, because of the slow reaction rate, have been achieved successfully in all cases. As described in section 3.3.1 previous study, I have clarified that the resolution of the current electrochemical method is around 0.30 nm min⁻¹.

It should be stressed here that the tendency of the change in scattering intensity for the case where $d = -5$ nm is quite different from the corresponding tendencies for the other structures with distinct d values. From 0 to 200 s and from 420 to 1200 s, the

scattering intensity decreased exponentially in the same manner as the other structures, but this intensity gradually increased between 200 and 420 s. This scattering property change can be correlated with the gradual gap formation that occurs at the centers of these structures. Notably, a dip due to the intensity modulation was observed at approximately 420 s. When the continuous nature of the dissolution process is considered, it can be assumed that the gap was formed at the time at which this dip was observed. SEM and atomic force microscopy (AFM) images shown in figure 3-6(b) and figure 3-8, respectively, which were obtained after the electrochemical measurements for 1200 s, verify the formation of the gap after the dissolution process, particularly at the contact of the dimer structure with $d = -5$ nm that was confirmed before dissolution. Therefore, flexible modulation of hybridized plasmon of dimers would be achieved by fine controlling this structure using the electrochemical dissolution process.

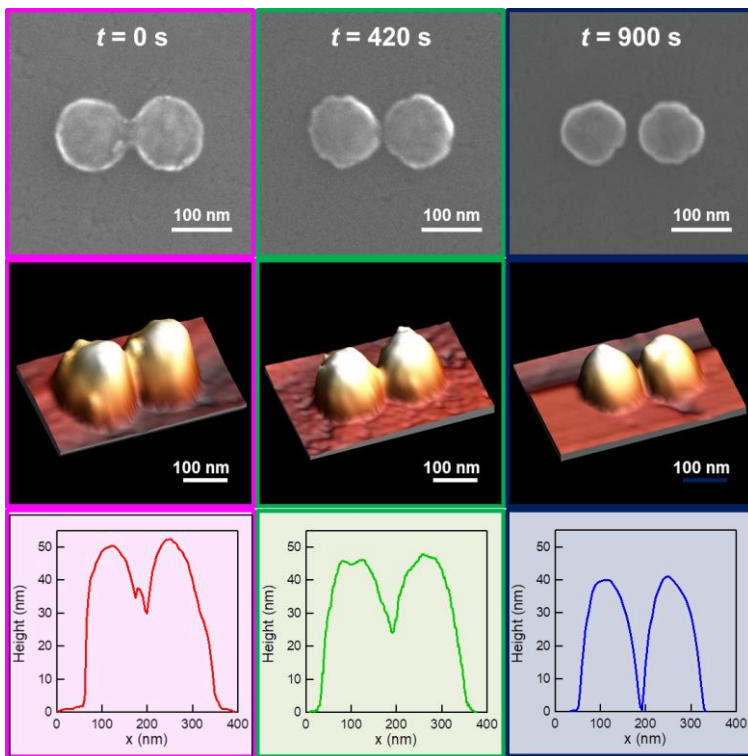


Figure 3-8. The SEM and AFM measurements of Au dimer structures obtained at dissolution time. Each potential applying time was (left) 0, (middle) 420, (right) 900 sec. The middle images were 3D AFM images for each structure. The bottom column is the cross-section view obtained at the center of the dimer structure.

3.3.3 *In situ Observations of Plasmonic Property Changes During Electrochemical Reactions*

To investigate further, more detailed discussion of the structural changes during the formation of the gap was conducted through in situ spectral measurements. Time-series scattering spectra for the structure with $d = -5$ nm were collected during the electrochemical dissolution reaction. Figure 3-9(a) and (b) were obtained under illumination by the transverse and longitudinal polarizations, respectively, with an oblique angle of incidence of 43° . The right panels in both figures represent the scattering intensities that were obtained from the left panel in each case. The vertical axes indicate the time required for the electrochemical

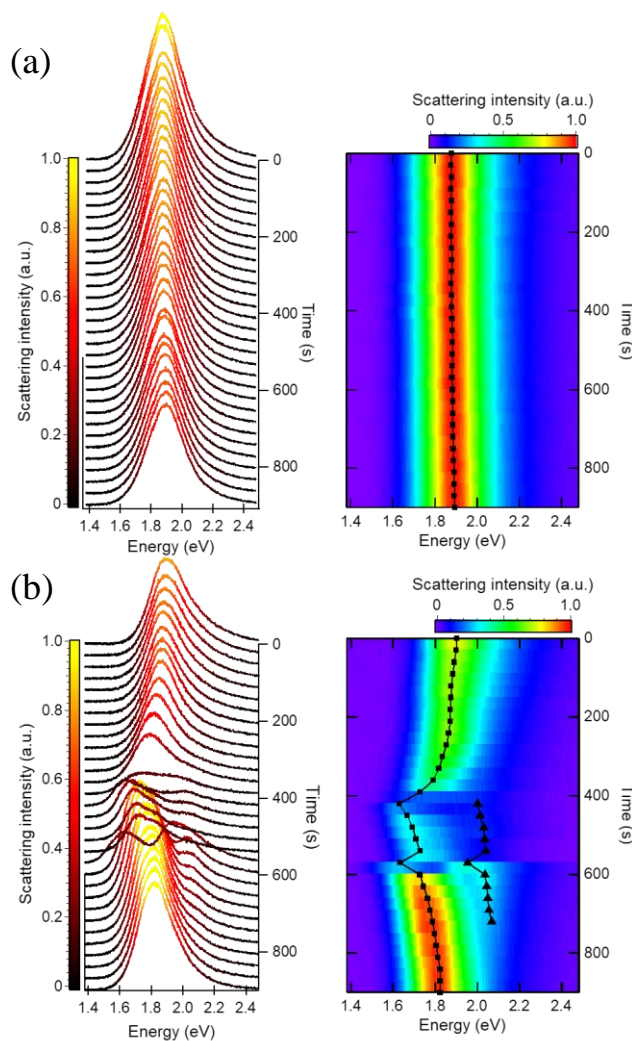


Figure 3-9. Time series scattering spectra of Au nanodisk arrays with a gap distance of -5 nm under a polarization potential of 0.74 V in 10 mM KBr aq. The polarization directions of the incident light were oriented (a) vertical and (b) parallel to the long axis of the structure. The vertical axis corresponds to the potential polarization time. The right panel of the figure shows the image plots of the scattering intensity.

dissolution processes. For the transverse polarizations shown in figure 3-9(a), while the scattering intensity did decrease gradually, the shapes of the spectra did not change. In

addition, the linewidth of the spectra which is affected by the radiation damping also remained almost the same. In contrast, figure 3-9(b) for the longitudinal polarizations shows apparent changes in both the spectra and the scattering intensities. In this case, from a dissolution time of 0 s to 400 s, the single plasmon mode shifted from 1.91 to 1.83 eV as the intensity decreased. After the sudden disappearance of the mode at 420 s, a novel mode with relatively weak scattering appeared at approximately 1.6 and 2.0 eV until the time reached 570 s. Then, a strong single plasmon mode appeared again at 1.78 eV and subsequently shifted to 1.83 eV as the dissolution progressed after 600 s. It should be mentioned here that this plasmon resonance energy shift occurs as a result of the changes in the free electron density determined by the electrochemical potential. While several reports, including the previous work in Murakoshi Lab., have revealed the effect of the electrochemical potential on the plasmon resonance, the spectral changes observed at the constant electrochemical potential here originated from changes in the volume and the shape of the dimer structure.

Importantly, in figure 3-9(b), during the time region from 420 to 600 s, dramatic changes were observed in both the spectra and the light scattering intensity. These characteristic changes for the structure with $d = -5$ nm were not observed in the other structures with distinct d values. The same in situ

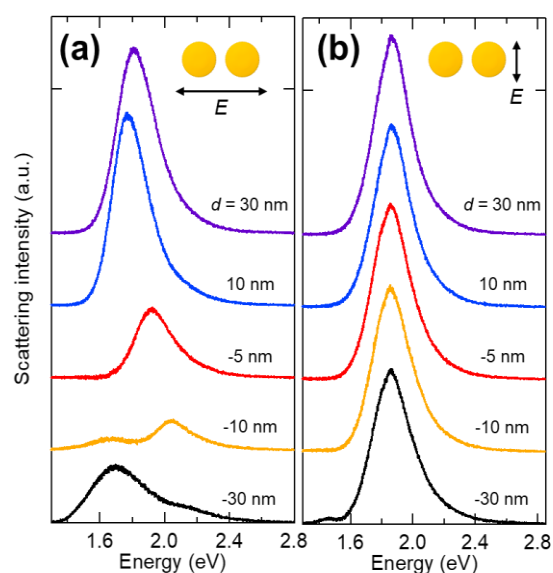


Figure 3-10. Polarized scattering spectra for Au dimer structures with various d values immersed in the electrolyte solution. Each polarized direction was (a) parallel and (b) vertical to the long axis of the dimer structure, respectively.

scattering measurements have also been conducted for all other structures. In figure 3-10, a clear dependence on the light polarization direction was successfully observed but the unique intensity suppression behavior observed in figure 3-10(b) could not be confirmed.

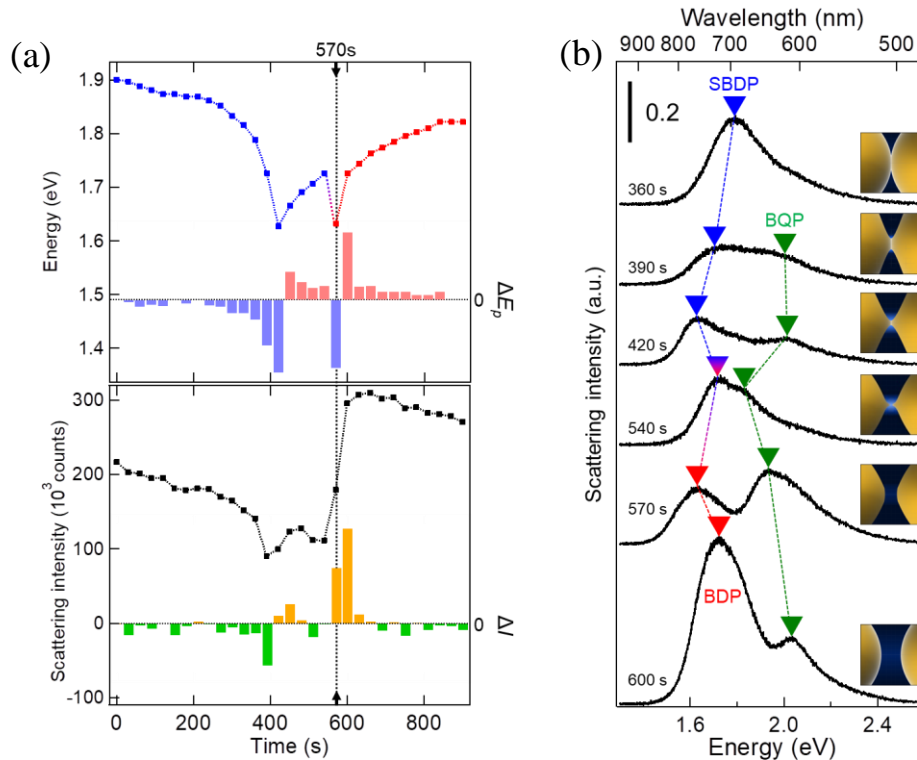


Figure 3-11. (a) Maximum plasmon energy and scattering intensity changes as a function of the polarization time. The bars at the specific points indicate the change ratios of the plasmon resonance energy and the scattering intensity versus that at the previous point. (b) Normalized scattering spectra obtained at each potential polarization time. The insets show the schematic illustrations of the presented dissolution process at each potential polarization time.

The observed shifts in the energies of these modes may reflect the changes in the gap structure. Proposed structures for the gap during dissolution are shown schematically in figure 3-11(b) with their corresponding spectra. During the dissolution process up to 360 s, the observed single plasmon mode can be assigned to the shielded BDP mode. The red shift in the shielded BDP was due to the reduction in the volume of the conduction path.⁶ Suppression of the scattering intensity showing the two modes, i.e., the shielded BDP and BQP modes, at 390 s reflects the formation of a very narrow

conductive channel at the gap. The abrupt changes observed in both the resonance energy and the scattering intensity at 420 s indicate the breaking of the narrow conduction path to form a very small gap, which results in the mode transition from the shielded BDP mode to the BDP mode observed at 1.62 eV. At the mode transition from the shielded BDP to BDP, the BQP energy was shifted to a slightly higher energy, from 2.02 to 2.05 eV, which also reflected the formation of the gap. During the period from 420 to 540 s, the gap increased as the dissolution reflected the energy shift to the higher energy of the BDP. The small shoulder observed at 1.80 eV after dissolution for 540 s could be attributed to the excitation of the octupolar plasmon coupling modes, which are only excited on an ideal dimer structure with quite a small gap.⁹ On further dissolution up to 570 s, a very interesting recovery from the BDP to BQP modes was observed, as discussed previously. From SEM observations, we have confirmed that the plasmon transition was observed in only the case of the gap formation. Thus, it can be assumed that the present mode shift is due to the excitation of the higher order plasmon mode. This hypothesis could be supported by the previous documented results on the observation of the excitation of the higher order coupling mode on the ideal dimer of gold nanospheres.³⁰ The validity of the assignment of these two modes is supported by the higher energy shifts of the modes after further dissolution up to 900 s. The origin of the interesting spectral changes that occur from 540 to 570 s, which show the lower energy shift of the BDP mode and the recovery of the quadrupole mode, remains unclear at present. It can be assumed that the changes in the structures of the Au gap and in those of electrochemical double layer, which include adsorbed ions and hydrated water molecules, may contribute to the interesting plasmon mode transitions including the changes in the contribution of the quantum tunneling effect at ultra-small gaps. This

point cannot be elicited from other theoretical investigations and, therefore, should be the value for this work. Incidentally, in the experiments, I have also prepared the dimer structures with different structure heights ranging between 10 and 50 nm. By using different height structures, I have confirmed that the change in the structure height can be negligible because the change leads to just around 0.03 eV energy change. Thus, it can be said that the current observation as shown in figure 3-3 and 3-4 could have originated from the change in the gap distance within the dimer. Of course, further detailed studies using in situ vibrational spectroscopy may be required to clarify the origin of the changes to modify the dielectric constant at the gap.^{5,31} It should, however, be emphasized that the electrochemical method presented here is a very promising technique for control of the hybridized plasmon modes.

3.3.4 Finite-difference time-domain calculations

To verify the excitation of the quadrupolar mode, finite-difference time-domain (FDTD) calculations were performed, with the results shown in figure 3-12. As parameters for these calculations, the gap distances of the dimer and the oblique angle of incidence were set to -5 and 0.6 nm, and 43° , respectively. The calculated extinction spectra are shown in the top part of figure 3-12(a). The gap distance parameters for the blue and red lines were -5 and 0.6 nm, respectively. In the case where $d = -5$ nm (blue line), a single resonance peak was observed at 1.88 eV, while two resonance modes appeared at 1.69 and 1.98 eV (red line). The experimental scattering spectra obtained at polarization times of 0 and 570 s, corresponding to blue and red spectra, are depicted in the bottom panel of figure 3-12(a). In these scattering spectra, the two resonance peaks observed at 2.05 and 1.67 eV showed good agreement with the calculated results but it

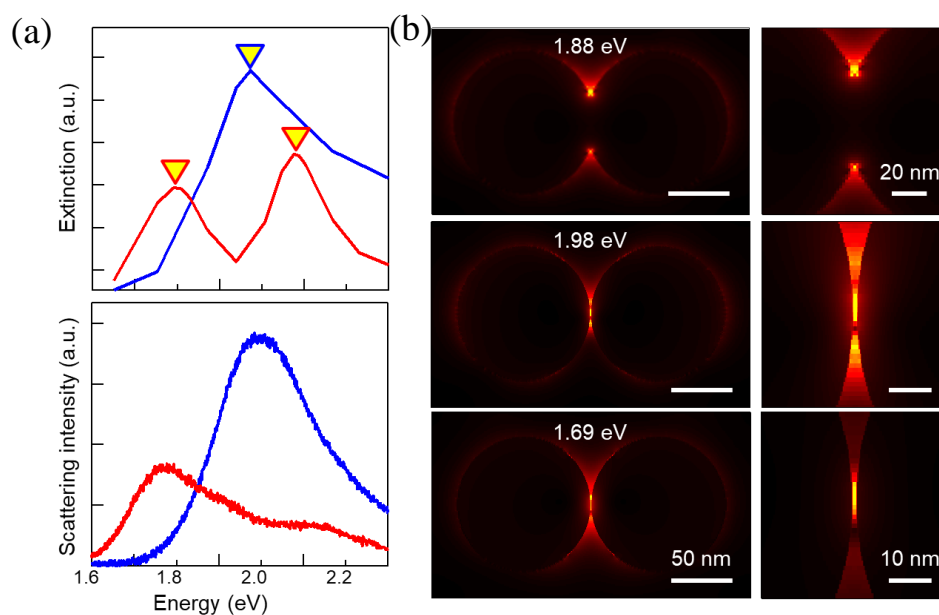


Figure 3-12. (a) Theoretically estimated extinction spectra of Au nanodisk arrays with gap distances of -5 (blue solid line) and 0.6 nm (red solid line) obtained using the FDTD method. The oblique angle of incidence and the permittivity of the surrounding medium were set at 43° and $\epsilon = 1.71$, respectively. (top) Scattering spectra of Au nanodisk arrays with a gap distance of -5 nm obtained at polarization times of 0 (blue solid line) and 570 s (red solid line). (bottom) (b) Spatial distributions of the electrical fields of the Au nanodisk array under illumination at (top) 1.88 , (middle) 1.98 , and (bottom) 1.69 eV. The gap distance parameters for these structures were (top and middle) -5 and (bottom) 0.6 nm.

was found that the scattering at 2.05 eV was strongly suppressed. In figure 3-12(b), the calculated spatial distributions of the electric fields for each resonance mode are shown. At 1.69 and 1.88 eV, simple bright spots that can be assigned to the dipolar plasmon mode can be confirmed, while three bright spots are observed at 1.98 eV. According to previous theoretical studies, the multiple bright spots can be attributed to the excitation of the quadrupolar antisymmetric distribution mode within the gap.^{9,32} As reported in one of these previous theoretical studies, far-field scattering is strongly suppressed as a result of the excitation of the quadrupolar mode.²¹ This would be a reasonable explanation for the nonappearance of the peak at 2.05 eV in the experimental scattering spectrum that was obtained at the polarization time of 570 s. When the gap distance of 0.6 nm is considered, the reaction ratio of d can be estimated to be approximately 0.13

nm min^{-1} ($2.2 \times 10^{-1} \text{ nmol min}^{-1}$), which is comparable with the value in section 3.3.1. As in the section 3.3.1, I have only observed the shift of the plasmon resonance wavelength because of the change in the size. Consequently, these comparisons of the experimental data with the calculated spectra strongly support the implication that the results presented here indicate successful gap control on a sub-nanometer scale that has not been achieved to date by other techniques under ambient conditions. Further studies on quantitative analysis on the absorption and the scattering could be important using developed calculations for comparisons with the experimental results of the present far-field scattering measurements as well as the near-field observations using such as photoemission electron microscopy (PEEM).

3.3.5 Long time excitation of higher order mode

In addition to the above investigations, I have demonstrated the characteristic advantage of the present electrochemical method. In the experiment, the electrode potential was scanned from 0.74 to 0.60 V after polarization for 420 s to stop the Au dissolution reaction. figure 3-13 shows the time-series scattering spectra that were obtained under these experimental conditions. An electrode potential of 0.6 V was maintained for 800 s to verify the stability of the excited quadrupolar mode. As a characteristic of the quadrupole mode, light scattering is suppressed for a long time. As shown in figure 3-13, the excitation of the quadrupole mode of the Au nanostructures remained very stable, even over this relatively long timescale. This means that the highly confined light energy is retained very stably in the sub-nm gap and it is thus possible to control the forbidden mode very precisely. Fortunately, I have confirmed that not only the sub-nanometer gap but also the plasmon modes were stable even after

exposure to air (data are not shown). As mentioned earlier, at the present stage, the control of the gap distance with atomic level resolution that allows the excitation of the quadrupole mode is quite difficult for the ordinary nanostructuring techniques under ambient conditions. It is also known that the quadrupole mode is a non-radiative mode, leading to a longer plasmon excitation lifetime than the pure dipolar modes. This fact improves the possibility for the application of the currently presented method to the various methods. In addition, according to the previous reports, with the excitation of the quadrupolar mode, a strong radiation pressure can be caused by the enormous spatial gradient that occurs at the structure.^{33,34} Therefore, I am sure that our proposed electrochemical method is both innovative and useful because it allows atomic scale structure tuning to be achieved easily with high reproducibility.

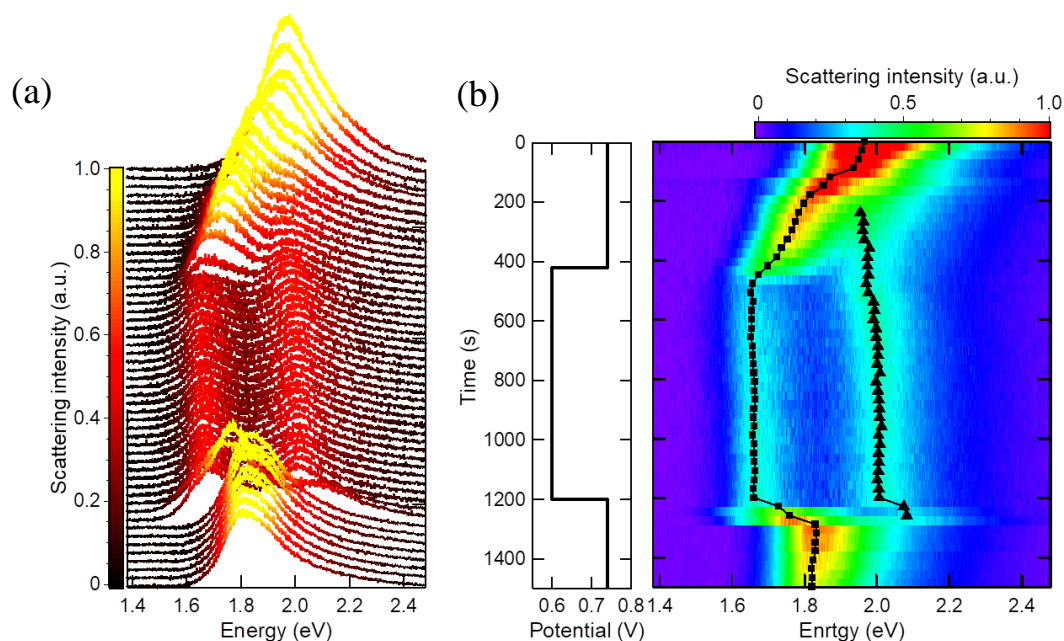


Figure 3-13. (a) Time series scattering spectra for bridged Au nanodisk arrays with a gap distance of -5 nm. The electrode potential was scanned from 0.74 to 0.6 V at 400 s and from 0.6 to 0.74 V at 1200 s. (b) Image plot of the scattering intensity as a function of the potential polarization time as estimated from figure 3-13(a).

3.3.6 Photoelectron Emission Microscopic (PEEM)

Measurement for Dissolved Au Nanodisk Array

The present method has made it possible to easily and stably control the Au nanodisk array in sub-nanometer scale. Here, for the first time, I experimentally prove that a much enhanced near-field is formed in a delicately tuned structure. Indirect observations of near-field were performed using a photoemission electron microscope (PEEM) shown in figure 3-14(a). When a strong excitation light source of 120 mW is irradiated and traced to the metal nanoparticles, the mode-dependent photoelectron image and intensity spectrum can be obtained since the plasmon electrons are emitted as photoelectrons. In this experiment, the PEEM trace range was set from 1.41 eV to 1.72 eV. In this experiment, BQP mode was not directly excited in this energy range. As shown in Figure 3-14(b), weak photoelectrons were observed from the structure with conductive path ($d = -5$ nm). On the other hand, strong photoelectrons were observed in the structure with narrow gap ($d = 5$ nm). As in previous reports, when the measured photoelectrons were plotted, the PEEM spectra were in good agreement with the scattering spectra shown in figure 3-14(c). This result indicates that the photons are scattered by the same scattering process via BDP or SBDP under the same condition. Surprisingly, the controlled structures with sub-nanometer gap distances showed different behaviors. The shapes of the photoelectron emission spectrum and the scattering spectrum are in good agreement, but the photoelectron intensity on the high energy side is strongly enhanced. In this trace range, not only the BDP but also the edge of BQP is excited, so it is expected that the photoelectron intensity will be amplified several times through the long-lived dark mode excitation. This finding is a new

phenomenon that has not been reported in previous studies for plasmonic dimers. For further detailed research, it is desirable to directly excite BQP and investigate its relaxation process by lifetime measurement. The near-field enhancement effect supported by photoelectrons of amplification due to the influence of BQP provides a bright future for the extreme localization of light.

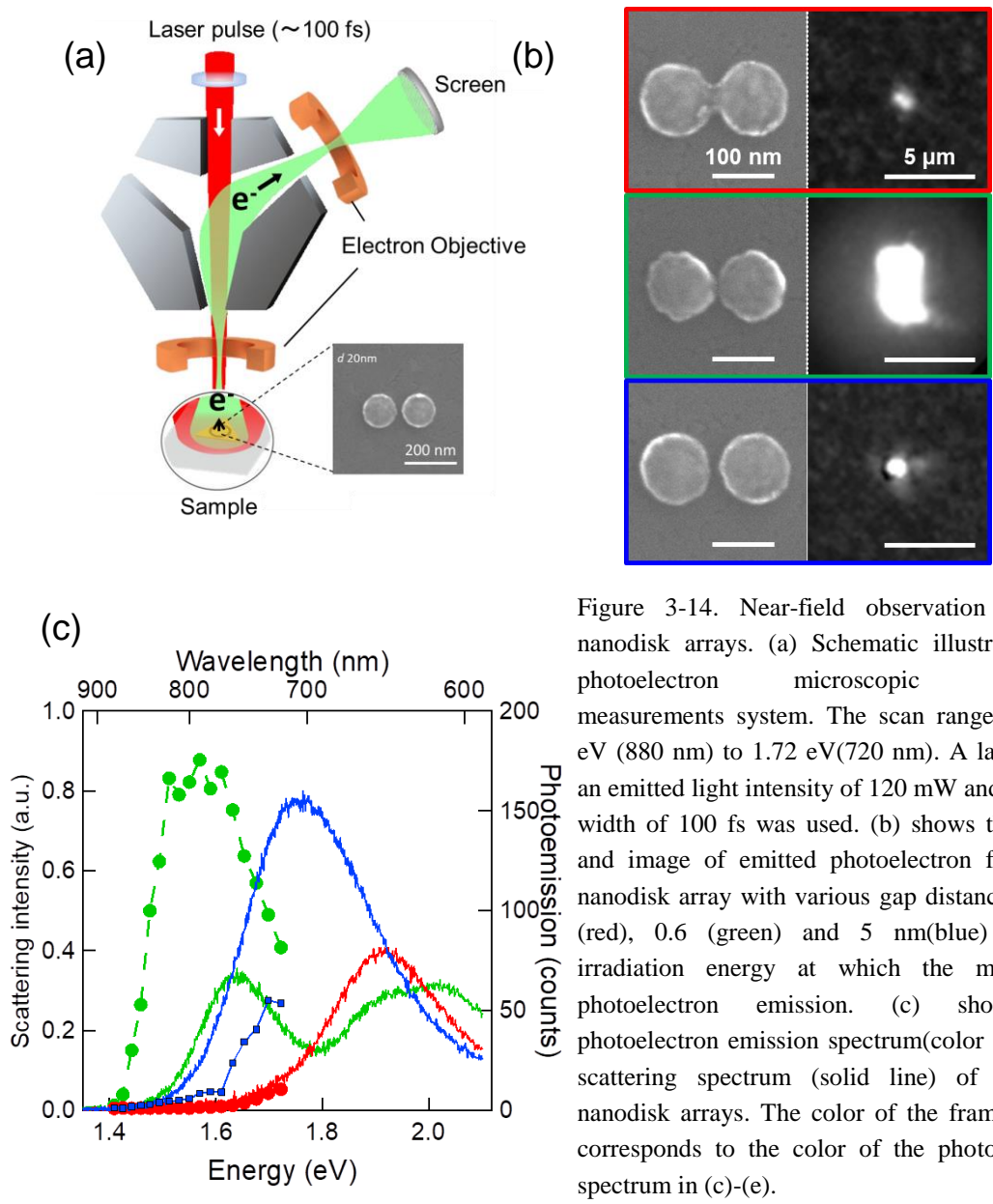


Figure 3-14. Near-field observation of Au nanodisk arrays. (a) Schematic illustration of photoelectron microscopic (PEEM) measurements system. The scan range is 1.41 eV (880 nm) to 1.72 eV(720 nm). A laser with an emitted light intensity of 120 mW and a pulse width of 100 fs was used. (b) shows the SEM and image of emitted photoelectron from Au nanodisk array with various gap distances of -5 (red), 0.6 (green) and 5 nm(blue) at the irradiation energy at which the maximum photoelectron emission. (c) show the photoelectron emission spectrum(color dot) and scattering spectrum (solid line) of the Au nanodisk arrays. The color of the frame in (b) corresponds to the color of the photoelectron spectrum in (c)-(e).

3.3.7 Monoatomic Control of Au nanodisk Arrays

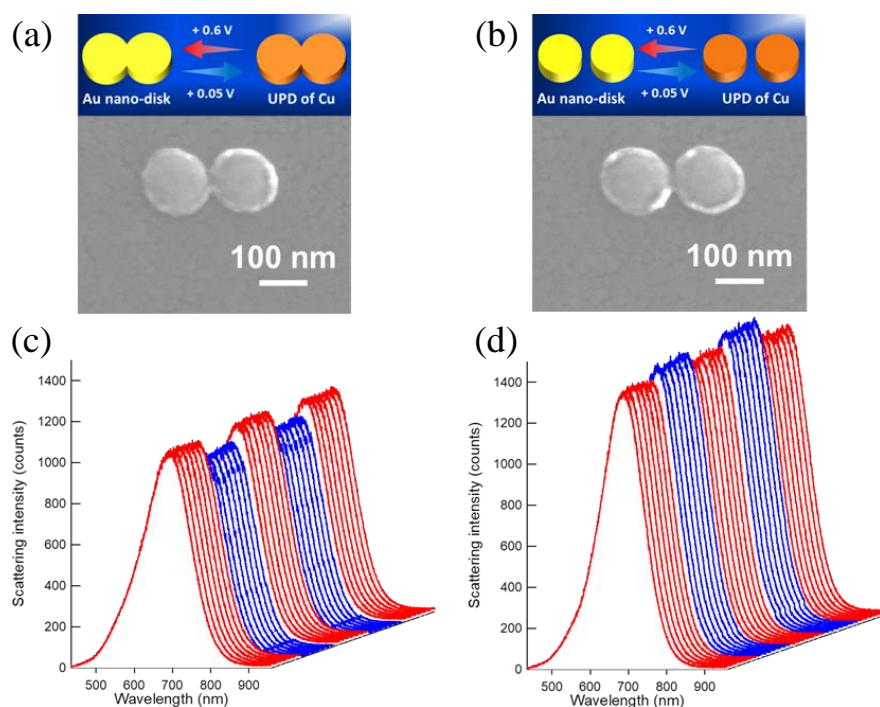


Figure 3-15. SEM images of Au nanodisk arrays with gap distance of (a) -5 nm and (b) 10 nm. The inserted schematic illustrations show the structural changes before and after the UPD. Scattering spectra obtained during Cu UPD process on Au nanodisk dimer with gap distance of (a) -5 nm and (b) 10 nm in 1 mM $\text{CuSO}_4 + \text{H}_2\text{SO}_4$ aq.

As for the additional structure control method, the reversible Cu monatomic layer modification is applied to the dimer with a conductive path and with a gap by controlling the Cu UPD reaction as shown in figure 3-15(a) and (b). In the case of the dimer with conductive path, a blue-shift of the plasmon resonance and a decrease of scattering intensity are expected because the conduction path will be covered with a Cu monatomic layer. On the other hand, in the dimer with a gap, a red shift of the plasmon resonance and an increase of scattering intensity are expected due to the decrease of the gap distance. Scattering spectra were acquired with the electrode potentials reversible switching between 0.6 (red line) and 0.05 V (blue line) on the dimer structure. As shown in Fig. 3-15 (c) and (d), no shift in resonance wavelength was observed on the bridged

structure showing CTP mode but only a decrease in scattering intensity was observed. On the other hand, on the structure with the gap, the red shift of the resonance wavelength and an increase in scattering intensity due to a decrease in the gap distance and an increase in volume were confirmed. Since the plasmon resonance shift and the change in scattering intensity can be reversibly controlled by repeatedly sweeping the electrode potential, it can be said that the reversible modulation of the dimer plasmon by the precipitation of the Cu monatomic layer was achieved. As I introduced in chapter 1, it is known that the bridged structure, the resonance wavelength shifts to the higher energy by increasing the electron conductivity between the particles. Further, it is known that the LSP resonance of a single metal particle shifts to the lower energy when the volume increases. Under Cu monatomic layer deposition, the above-mentioned conductivity and volume increase occur at the same time in the CTP structure. Therefore, in the CTP structure, the blue shift due to the increase in the conductivity and the red shift due to the increase in volume are antagonized, and as a result, CTP didn't show a plasmon shift. Consequently, I believe that the present method would contribute to reversible control of the optical properties of Au nano-bridged structures. In future, we may develop more structure-sensitive systems using various types of metal nanostructures to control the localization of electromagnetic field with high precision, especially for the optical measurements in the infrared wavelength region.

3.4 Conclusion

A new technique to control the nanoprism dimer structures within a few nanometers was achieved by combining an electrochemical approach with in situ optical measurements. The important advantage of our method is its ability to control the structure volume, leading to plasmon resonance wavelength shifts, simply by regulating the potential application time under appropriate electrochemical conditions. Furthermore, the change of the volume and gap distance can be numerically estimated from the electrochemical and optical measurements. The results obtained from both approaches correlated well with each other. This approach has been extended to sub-nanometer control of the gap. Notably, the sub-nanometer gap enabled the realization of characteristic light scattering suppression at a specific polarization time because of the excitation of the quadrupole mode. In addition, this quadrupole mode, which is only excited on structures with a gap distance of less than 1 nm, can be maintained for long periods by simply changing the applied potential. During light suppression, the light energy is highly localized at the gap, so various applications of this behavior, such as optical manipulation of molecules, can be expected. In addition, the structure and plasmon properties were reversibly controlled by using the Cu UPD method. Consequently, the proposed electrochemical method will have a major impact on the optical field and can be used in various ways to provide further improvements for specific spectral regions.

3.5 References

- (222) Atay T., Song J. and Nurmikko A. V., *Nano Lett.* **4**, 1627–1631 (2004).
- (223) Romero I., Aizpurua J., Bryant G. W. and Javier García de Abajo F. *Opt. Express*, **14**, 9988 (2006).
- (224) Lassiter J. B., Aizpurua J., Hernandez L. I., Brandl D. W., Romero I., Lal S., Hafner J. H., Nordlander P. and Halas N. J. *Nano Lett.*, **8**, 1212–1218 (2008).
- (225) Scholl J. A., García-Etxarri A., Koh A. L. and Dionne J. A. *Nano Lett.*, **13**, 564–569 (2013).
- (226) Savage K. J., Hawkeye M. M., Esteban R., Borisov A. G., Aizpurua J. and Baumberg J. *J. Nature*, **491**, 574–577 (2012).
- (227) Esteban R., Borisov A. G., Nordlander P. and Aizpurua J., *Nat. Commun.* **3**, 825 (2012).
- (228) Vieu C., Carcenac F., Pépin A., Chen Y., Mejias M., Lebib A., Manin-Ferlazzo L., Couraud L. and Launois H. *Appl. Surf. Sci.*, **164**, 111–117 (2000).
- (229) Ueno K., Takabatake S., Nishijima Y., Mizeikis V., Yokota Y. and Misawa H. *J. Phys. Chem. Lett.*, **1**, 657–662 (2010).
- (230) Yoon J. H., Selbach F., Langolf L. and Schlücker S. *Small*, **14**, 1702754 (2018).
- (231) Byers C. P., Hoener B. S., Chang W.-S., Yorulmaz M., Link S. and Landes C. F. *J. Phys. Chem. B*, **118**, 14047–14055 (2014).
- (232) Byers C. P., Zhang H., Swearer D. F., Yorulmaz M., Hoener B. S., Huang D., Hoggard A., Chang W.-S., Mulvaney P., Ringe E., Halas N. J., Nordlander P., Link S. and Landes C. *F. Sci. Adv.*, **1**, e1500988 (2015).
- (233) Herrera M. Z., Aizpurua J., Kazansky A. K. and Borisov A. G. *Langmuir*, **32**, 2829–2840 (2016).
- (234) Hoener B. S., Byers C. P., Heiderscheit T. S., De Silva Indrasekara A. S., Hoggard A., Chang W. S., Link S. and Landes C. F. *J. Phys. Chem. C*, **120**, 20604–20612 (2016).
- (235) Zhu H., Xie H., Yang Y., Wang K., Zhao F., Ye W. and Ni W., *Nano Lett.*, **20**, 2423–2431 (2020).
- (236) Minamimoto H., Oikawa S., Hayashi T., Shibazaki A., Li X. and Murakoshi K. *J. Phys. Chem. C*, **122**, 14162–14167 (2018).

- (237) Halas N. J., Lal S., Chang W S, Link S. and Nordlander P. *Chem. Rev.*, **111**, 3913–61 (2011)
- (238) Huang W., Qian W. and El-Sayed M. A. *J. Phys. Chem. B*, **109**, 18881–8 (2005)
- (239) Ikeda K, Takase M, Hayazawa N, Kawata S, Murakoshi K and Uosaki K *J. Am. Chem. Soc.* **135**, 11489–92 (2013)
- (240) Sawai Y, Takimoto B, Nabika H, Ajito K and Murakoshi K *J. Am. Chem. Soc.* **129**, 1658–62 (2007)
- (241) Nagasawa F, Takase M and Murakoshi K. *J. Phys. Chem. Lett.* **5**, 14–19 (2014)
- (242) Diaz M. A., Kelsall G. H. and Welham N. J. *J. Electroanal. Chem.* **316**, 25–38 (1993)
- (243) Willets K A and Van Duyne R P *Annu. Rev. Phys. Chem.* **58**, 267–297 (2007)
- (244) Kelly K L, Coronado E, Zhao L L and Schatz G C *J. Phys. Chem. B*. **107**, 668–677 (2003)
- (245) Mogensen K B and Kneipp K *J. Phys. Chem. C* **118**, 28075–28083 (2014)
- (246) van Dijk M A, Tchegbotareva A L, Orrit M, Lippitz M *Phys. Chem. Chem. Phys.* **8**, 3486 (2006)
- (247) Hashimoto S, Werner D and Uwada T *J. Photochem. Photobiol. C*. **13**, 28–54 (2012)
- (248) Hartland G V *Chem. Rev.* **111**, 3858–87 (2011)
- (249) Shimizu T, Teranishi T, Hasegawa S and Miyake J. *Phys. Chem. B* **107**, 2719-24 (2003)
- (250) Itoh T., Yamamoto Y. S. and Okamoto T., *Phys. Rev. B*, **99**, 235409 (2019).
- (251) Chen H., Sun Z., Ni W., Woo K. C., Lin H.-Q., Sun L., Yan C. and Wang J. *Small*, **5**, 2111–2119 (2009).
- (252) Templeton A. C., Pietron J. J., Murray R. W. and Mulvaney P. *J. Phys. Chem. B*, **104**, 564–570 (2000).
- (253) Tanaka Y., Sanada A. and Sasaki K. *Sci. Rep.*, **2**, 764 (2012).
- (254) Kuttge M., García de Abajo F. J. and Polman A. *Nano Lett.*, **10**, 1537–1541 (2010).
- (255) Chang Y. C., Wang S. M., Chung H. C., Tseng C. H. and Chang S. H. *ACS Nano*, **6**, 3390–3396 (2012).

Chapter 4

Enhanced Fluorescence via Bright and Dark SLR Modes

Supported by In- and Out-phase Coherent Coupling

4.1 Introduction

Localized surface plasmons excited on metal nanoparticles have extremely small mode volumes and high field enhancements, thus, they can be applied as the ideal platform nanoscale photochemical phenomena, i.g., strong coupling,^{1,2} photo lasing^{3,4} or photon condensation⁵. However, at visible frequencies, such applications are often limited due to the strong ohmic and radiative losses.⁶ Therefore, in order to open new prospects for light-matter interactions, it is required to reduce those losses with the strong near-field enhancement.

As I introduced in the general introduction, the periodic metal nanoparticles show coherent polariton modes called as the surface lattice resonance (SLR) mode. The SLR mode is the hybrid of localized surface plasmon resonances of nanoparticles with the diffracted scattering fields from each particle, resulting in the narrow linewidth.⁷⁻¹⁰ Several factors, such as the mode energies, losses, and optical density of states can be tuned by the lattice and particle geometry control. Recently, various interesting observations, e.g., the strong coupling with organic molecules^{2,11,12} and/or the infrared lasing on weak coupling^{13,14} have been reported. Recently, it has been reported that plasmonic lattices can also generate so-called dark SLR modes, whose subradiant character results in significantly higher Q-values as compared with their radiant (bright) counterparts.^{15,16} Thus, the plasmonic dark modes are promising candidates for realizing

lasing, single-emitter strong coupling, or the photon condensation at visible wavelengths. Although the extended lifetime and lasing behavior have already been observed in Ag lattices,^{15,16} the excitation mechanism and conditions of dark modes have not been investigated in detail, so it is necessary to reveal how to excite and couple out these subradiant modes.

In this section, I demonstrated the enhanced fluorescence using bright and dark SLR modes of Au nanodisk arrays combined with optically pumped dye molecules. The excitation of the dark SLR mode was achieved by a coherent out-coupling mechanism based on the Au arrays and dipole sources provided by high-concentration dye coverage. The examinations using the various lattice structures have revealed that dark plasmons were excited only when they overlap with the fluorescence spectrum of the dye molecules. Fluorescence via dark mode showed stimulated emission based on narrow line width, similar to bright mode. In addition, it was demonstrated that bright and dark SLR modes can support fluorescence enhancement even when weak light sources such as electrogenerated chemiluminescence (ECL) are used. By optimizing conditions such as dye and excitation wavelength, it was expected that a population inversion could be formed at low threshold. These results open a route to utilize Au plasmonic lattices for studies of strong light-matter interactions and photon condensation.

4.2 Experimental Method

4.2.1 Sample fabrication

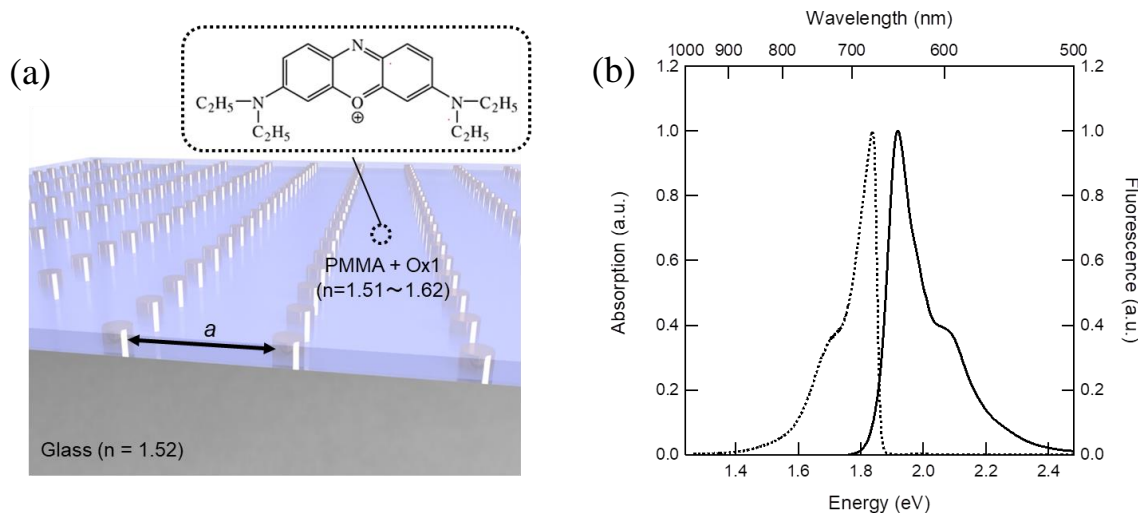


Figure 4-1. (a) Schematic illustration of dye film supported square lattice of Au nanodisk arrays with various lattice spacing of a on glass substrate. The diameter and height of the nanodisks are 100 nm and 75 nm, respectively. The molecular structure in the figure shows oxazine 1 (Ox1) used as a gain. A 100 nm thick mixed thin film of Ox1 and PMMA was spin coated to make the environment around the lattice uniform. In the dye concentration range used in the experiment, the refractive index of the thin film was modulated from 1.52 to 1.62. (b) shows the absorption (solid line) and fluorescence (dashed line) spectra of Ox1 in acetonitrile. In acetonitrile, the absorption maximum of Ox1 is observed at 1.92 eV (646 nm) and the fluorescence maximum is observed at 1.84 eV (675 nm).

Square lattices of Au nanodisk arrays with various lattice space (a) were fabricated on glass substrate by EBL method as I described in chapter 2. The diameter and height of the nanodisks for all cases were set to 100 and 75 nm, respectively. The a values were ranging between 400 to 500 nm. The surface of the gold nanodisk was covered with an aluminum oxide layer with the thickness of 5 nm by the atomic layer deposition (ALD) method (using Picosun SUNALE-R) to suppress the energy transfer between the dye molecule and the metal surface. For the increase of its Q-factors, all samples were pre-annealed at 200°C for 20 min (see chapter 2). The dye molecule of the oxazine 1 (Ox1) was dissolved in a dichloroethane solution containing 1.2 wt% PMMA

at the desired concentration. Then Ox1 thin film was formed by spin-coating at 1500 rpm for 60 s. From AFM observation, it was confirmed that a uniform thin film of 100 nm with a roughness of about 2 nm was formed. In the experiment, the Ox1 concentration was controlled from 1 to 50 mM and the index of refraction of the thin film was modulated from 1.52 to 1.62.

4.2.2 Angle-Resolved Extinction Measurement

LED light source (THORLABS MBB1L3) was collimated by three convex lenses and polarized with a linear polarizer. The collimated beam was focused on the surface of the sample with a spot size of 3 mm and NA of 0.08. The transmitted light was collected using a 60x objective lens using an inverted microscope (Olympus IX-71) and was sent to the entrance port of an imaging spectrometer (Teledyne Princeton Instruments IsoPlane sct320) equipped

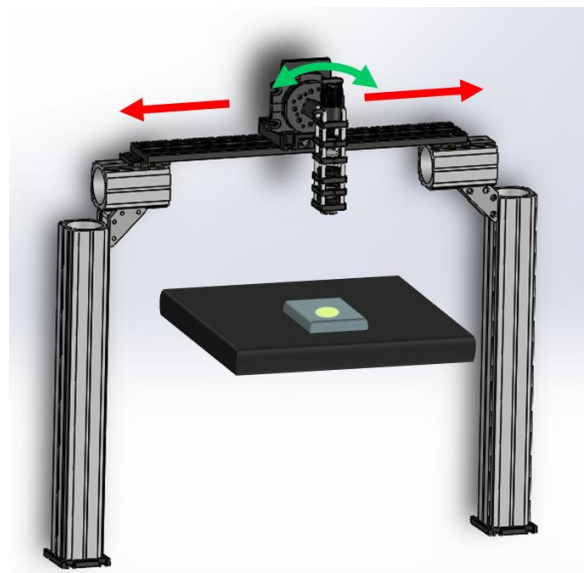


Figure 4-2. Schematic illustration of angle resolved extinction measurement set up. The LED light source was collimated by the lens. The spot diameter is 3 mm and the angle resolved range is 0 to 40 °. The transmitted light was collected by a 60x objective lens with NA of 0.7.

with a charge-coupled device (CCD) camera (Teledyne Princeton Instruments PIXIS100). Transmission spectra were measured using the bare substrate areas ($3 \times 3 \mu\text{m}^2$) of the sample as the background. The light source was adjusted so that the spot overlapped the pupil of the objective lens after fixing the angle. The extinction spectra

were calculated from the common logarithm ($\log T_0/T$) of the ratio of the transmittance on sample (T) to without the sample (T_0).

4.2.3 Fluorescence Measurement Set Up

Fluorescence measurement was performed by wavelength-variable laser. The output of an optical parametric amplifier (OPA) with 100 fs pulse width and 1 kHz repetition was directed through a pinhole and focused to the sample via a lens and a mirror. The pumping light was spatially filtered using an aperture diaphragm and irradiated to the sample using a 10x objective (NA 0.3). The fluorescence spectra were obtained by focusing the back focal plane of the imaging objective to the entrance slit of the spectrometer equipped with a two-dimensional CCD camera (Teledyne Princeton Instruments PIXIS100BR_Excelon). The excitation wavelength was set to 620 nm and the 532 nm short-pass filter and a 650 nm long-pass filter were used. The fluorescence signals were filtered by a 675 nm long pass filter to reduce the effect of the light source. The light source power was adjusted using a $\lambda/2$ plate and an ND filter.

4.2.4 FDTD simulations for SLR modes

Finite-difference time-domain (FDTD) simulations were conducted using Lumerical's FDTD Solutions software. The nanoparticle was modelled as a 75 nm tall cylinder with a diameter of 100 nm. Tabulated material parameters for Au were used according to the previous report.¹⁶ A plane wave was installed over the substrate as infinite expanded light source. For the field profile simulations, the mesh size was set to 0.6 nm over the volume of the nanoparticle. Field profiles were recorded after the

simulation had run for 700 fs. An infinite array was considered in the simulations by choosing the x and y boundary conditions to be either Bloch (for bright mode) or asymmetric and asymmetric (for dark mode), respectively. Reflection (R) and transmittance (T) were monitored by placing power balance monitors above the light source and below the board. The optical cross-sectional area of the lattice structure was calculated from the following formula.¹⁷

$$\sigma_{ext} = (1 - T) * (a^2 \times \cos\theta)$$

$$\sigma_{sct} = R * (a^2 \times \cos\theta)$$

$$\sigma_{abs} = (1 - T - R) * (a^2 \times \cos\theta)$$

where a is the lattice period and θ is the incident angle. In the simulation, I calculated the total transmittance and reflectance.

4.2.5 Electrogenerated Chemiluminescence (ECL) measurement

Electrogenerated Chemiluminescence (ECL) measurement was performed on Ox1 molecules immobilized on Au nanodisk arrays immersed in 10 mM KOH aq., using three-electrodes cell as same in chapter 3. Au nanodisk array with a of 500 nm was fabricated on ITO coated glass substrate, and used as working electrode. As a luminophore of ECL, 10 mM Ox1 dissolved in dichloroethane was spin coated directly onto the substrate and dried. Supported Ox1 molecules remain on the electrode surface when immersed in supporting electrolyte. ECL was generated with the oxidative-reductive coreactant 2-(dibutylamino)-ethanol (DBAE).^{18,19} DBAE was dissolved in 10 mM KOH aq. and adjusted to 20 mM. The emission spectra were collected with exposure time of 20 s in the same system as section 4.2.2.

4.3 Results and Discussion

4.3.1 Confirmation of Surface Lattice Resonance

By EBL and low temperature annealing methods, a highly homogeneous Au nanodisk arrays was fabricated on glass substrate as shown in figure 4-3(a). The surrounding environment was unified by supporting a PMMA, leading to the appearance of the sharp and broad plasmon peaks with a FWHM of 0.02 eV at 1.62 eV and 0.45 eV at 2.06 eV, respectively. For clarifying these plasmon modes, electric field simulation with the FDTD method was performed. Based on SEM and AFM images, the nanoparticle was modelled as a 75 nm tall cylinder with a diameter of 100 nm. In order to represent the infinite array structure, Bloch periodic boundary conditions were applied to the x and y planes in the array plane. As shown in Figure 4-3 (b), the spectrum observed in the experiment was well reproduced by FDTD calculation. The calculated electric field distributions support the appearance of two distinguished plasmon modes. The sharp mode observed at 1.62 eV is confirmed to be surface lattice resonance (SLR) because in-plane expanded electric field and LSP of a single particle and in the plane are induced as shown in figure 4-3(c). On the other hand, the broad peak appeared at 2.06 eV is assigned to a pure LSP mode because the electric field is not spread in plane (figure 4-3(d)). Since SLR has an about four times stronger electric field than that of single-particle LSP, it is expected that the light-molecular interaction will be enhanced mainly through SLR. According to previous reports,²⁰⁻²⁴ it was confirmed that SLR shows angle dependent property and has localized optical density at an incident angle of 0 ° (Γ point) shown in figure 4(e). In this system, the SLR band

didn't overlap with the absorption wavelength of Oxazine 1 (Ox1), so it was predicted that fluorescence was enhanced via only the SLR electric field.

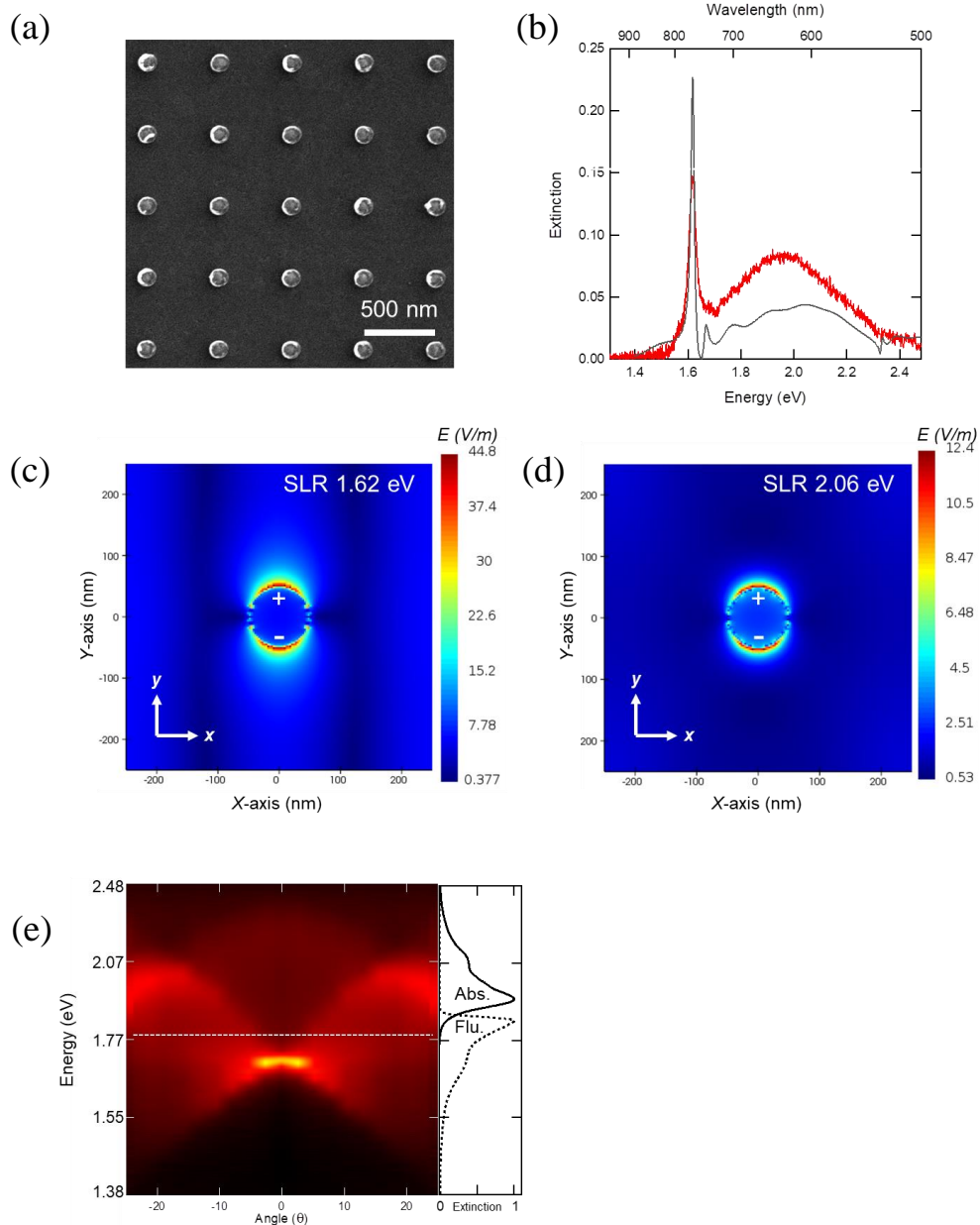


Figure 4-3. (a) SEM image of fabricated Au nanodisk arrays with lattice space of 500 nm by EBL. The diameter and height of the nanodisks are 100 nm and 75 nm, respectively. (b) Experimental (red curve) and calculated extinction spectra (black curve) of the Au nanodisk arrays in non-dye-doped PMMA thin film at incident angle 0° . The surrounding environment was unified to $n = 1.52$. (c) and (d) are simulated near-field distribution at 1.623 eV and 2.06 eV, respectively. (e) Angle-resolved extinction spectra of the structure. The absorption and fluorescence spectra of Ox1 are shown on the right on the same scale. The extinction spectrum of the structure only overlaps the fluorescence spectrum of the dye. The white dashed line in the figure indicates the absorption edge of the dye, which supports the SLR band and absorption not overlapping.

4.3.2 Fluorescence Behavior Depending on Dye Concentration

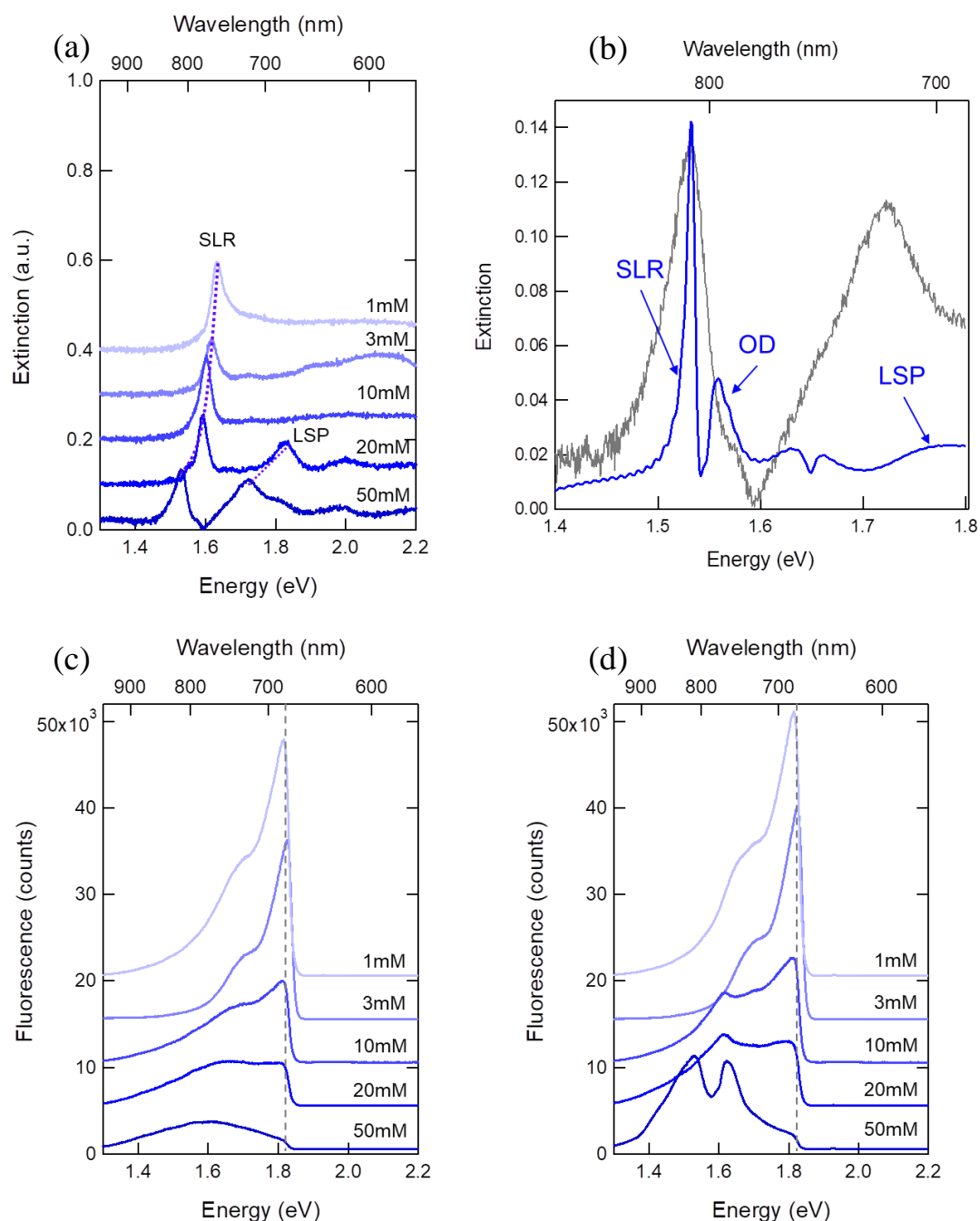


Figure 4-4 Extinction and fluorescence spectra depending on dye concentration. (a) Extinction spectra of Au nanodisk arrays with lattice space of 500 nm. (b) Simulated extinction spectra of Au nanodisk array with a of 500 nm. It was calculated with a refractive index of 1.62 and Bloch periodic boundary conditions. (c) and (d) are fluorescence spectra acquired from non- and structural areas, respectively. The supported dye concentration was controlled from 1 mM to 50 mM (from top to bottom in each figure). The sample was excited by a 620 nm 100 fs laser with a power of 5 mJ cm^{-2} . The gray dashed line shows the fluorescence of the S1 transition of Ox1.

Figure 4-4 (a) shows the extinction spectra of dye supported Au nanodisk array with a of 500 nm. The Ox1-doped PMMA thin film was supported on the structures. The dye concentration was changed from 1 to 50 mM. As can be seen in spectra, the SLR and LSP modes were red-shifted with increasing Ox1 concentration. It is predicted that this plasmon shift was caused by the refractive index change of the surrounding environment depending on the Ox1 concentrations. The FDTD calculation using the refractive index of 1.52 could not express the extinction spectrum of 50 mM. Instead, the calculation using the index of refraction of 1.62 confirmed that the peak positions matched at 1.523 eV, although there were differences in shape. Therefore, it was confirmed that the red-shift of plasmons is caused by the refractive index change (from 1.52 to 1.62) of the surrounding environment depending on the Ox1 concentration. In the experiment, the diffraction order (OD) and SLR could not be separated due to the resolution of the light source. Further, under high density conditions, the local refractive index over the metal may not be uniform due to the random placement of the mixed dyes. So it was considered that these experimental and environmental factors lead to spectral broaden in SLR. The extinction peak that appears at 1.75 eV at concentrations above 20 mM was considered to be LSP, although it is slightly red-shifted from the simulated results. It was predicted that shift shifts and intensity differences would depend on the local index of refraction, similar to SLR. The SLR shift and the surrounding environmental change were expected to significantly modulate the fluorescence characteristics of Au nanodisk arrays.

Fluorescence measurement for these samples was done using ultrafast laser ($\lambda_{\text{ex}} = 620 \text{ nm}$) with 100 fs pulse width. The laser power was set to 5 mJ cm^{-2} . It must be noted that, under these irradiation conditions, both structure and dye molecules are

physically stable during measurement. The fluorescence spectra collected from the Ox1 molecules at non-structural area showed a fluorescence intensity reduction with increasing dye concentration. Since the Stokes shift of the dye is small as shown in figure 4-1(b), it was considered that the fluorescence suppression are due to re-absorption between the dyes. On the other hands, the fluorescence spectra collected at structural area showed a decrease in fluorescence due to the S1 transition and a clearly enhanced fluorescence peak with red-shifting. The dramatic suppression of fluorescence via the S1 transition at 1.79 eV comes from the re-absorption of fluorescence between the dye molecules as same as figure 4-4(c). The red-shifting peak from 1.61 eV (for 10 mM) to 1.52 eV (50 mM) observed at concentrations above 10 mM coincides with the SLR position, so it was considered to be enhanced fluorescence via the SLR electric field. At low concentrations below 10 mM, no clear SLR-dependent peak shifts or enhancements were observed due to the high background fluorescence. Very interestingly, the sample with a dye concentration of 50 mM showed a new narrow fluorescence band around 1.61 eV in addition to the 1.52 eV fluorescence band corresponding to SLR. There is no plasmon peak around this energy band in the extinction spectrum (figure 4-4(a) and (b)). Therefore, this new enhanced fluorescence band might originated from the dark mode of SLR which were reported in the previous report.¹⁶

4.3.3 Periodic Dependence of Fluorescence via SLR

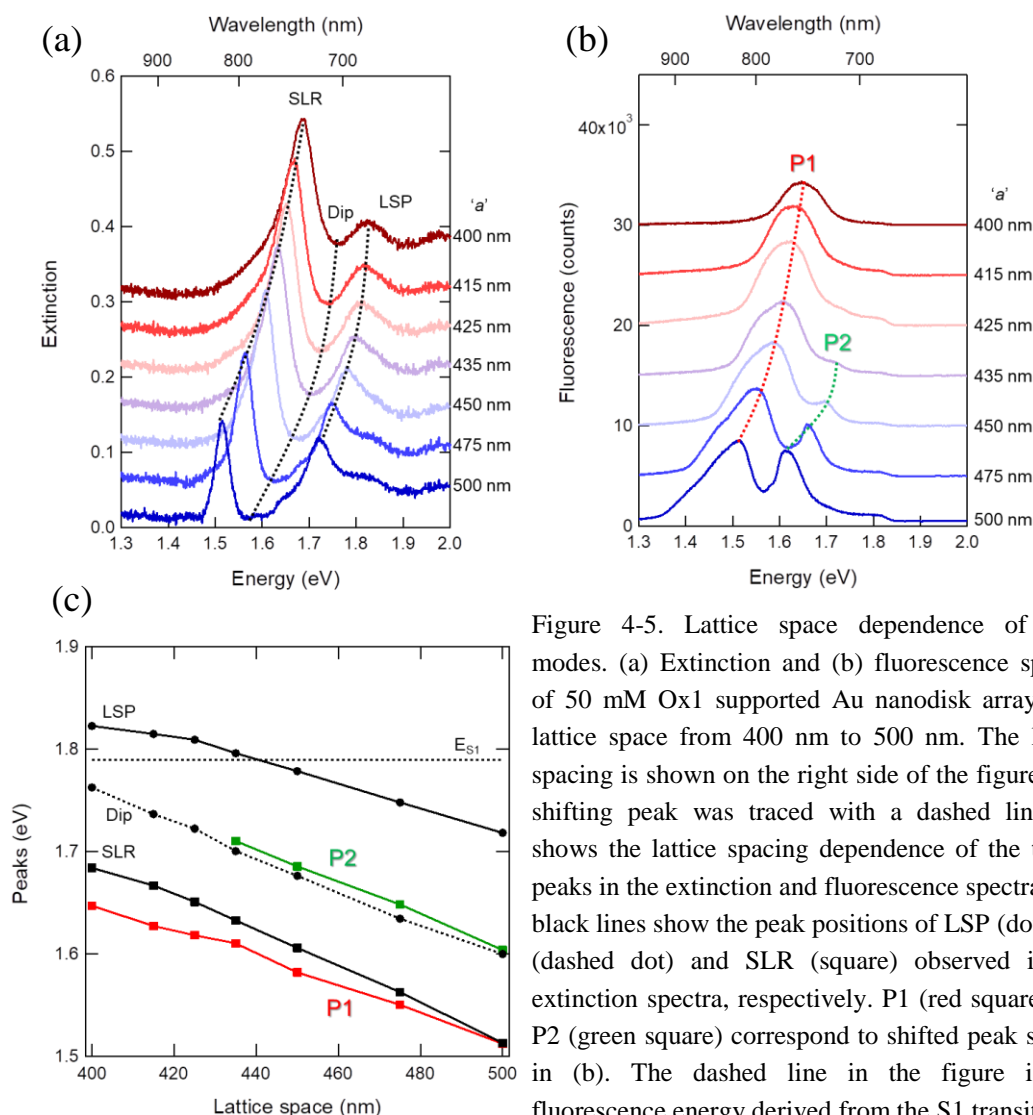


Figure 4-5. Lattice space dependence of SLR modes. (a) Extinction and (b) fluorescence spectra of 50 mM Ox1 supported Au nanodisk array with lattice space from 400 nm to 500 nm. The lattice spacing is shown on the right side of the figure. The shifting peak was traced with a dashed line. (c) shows the lattice spacing dependence of the traced peaks in the extinction and fluorescence spectra. The black lines show the peak positions of LSP (dot), dip (dashed dot) and SLR (square) observed in the extinction spectra, respectively. P1 (red square) and P2 (green square) correspond to shifted peak shown in (b). The dashed line in the figure is the fluorescence energy derived from the S1 transition.

Dark mode of SLR is excited by out-phase coherent coupling between scattered field and nanoparticles.¹⁶ Therefore, that mode can be modulated by tuning the lattice spacing, like as bright mode. In this experiment, the SLR was modulated by controlling the lattice spacing from 400 nm to 500 nm, but the supported dye concentration was fixed at 50 mM. As previously reported,⁶ the SLR, LSP, and the dip between them were red-shifted with increasing lattice spacing shown in figure 4-5(a). In the fluorescence spectrum of figure 4-5(b), two peaks with a red shift depending on the lattice spacing

were also observed. Since the energy position of the fluorescence peaks (P1) appearing at the low energy side overlap with the bright mode of SLR as shown in figure 4-5(c), the fluorescence was enhanced by the bright mode. On the other hand, the peaks named as P2 appearing at the high energy side overlap with the dip position of the extinction spectra, so it is considered that enhanced fluorescence induced via the dark SLR mode. However, curiously, P2 was not observed from Au nanodisk arrays with lattice spacing smaller than 435 nm. The LSP mode of the structure with lattice spacing of 435 nm just overlaps the S1 transition of the Ox1. Then, it is suggested that the LSP band of the structures with the lattice spacing smaller than 435 nm greatly overlap with the absorption band of Ox1. Since the dark mode of SLR slightly overlaps with the LSP band as shown in figure 4-6(a), it is expected that energy will be transferred via LSP mode to the dye absorption band, resulting in strongly energy suppression of dark SLR. Therefore, it was revealed that in order to achieve fluorescence enhancement via dark mode, not only the high concentration but also the SLR needs to be modulated so that the absorption band of the dye and the LSP mode do not overlap.

4.3.4 FDTD Simulation for Dark and Bright SLR Modes

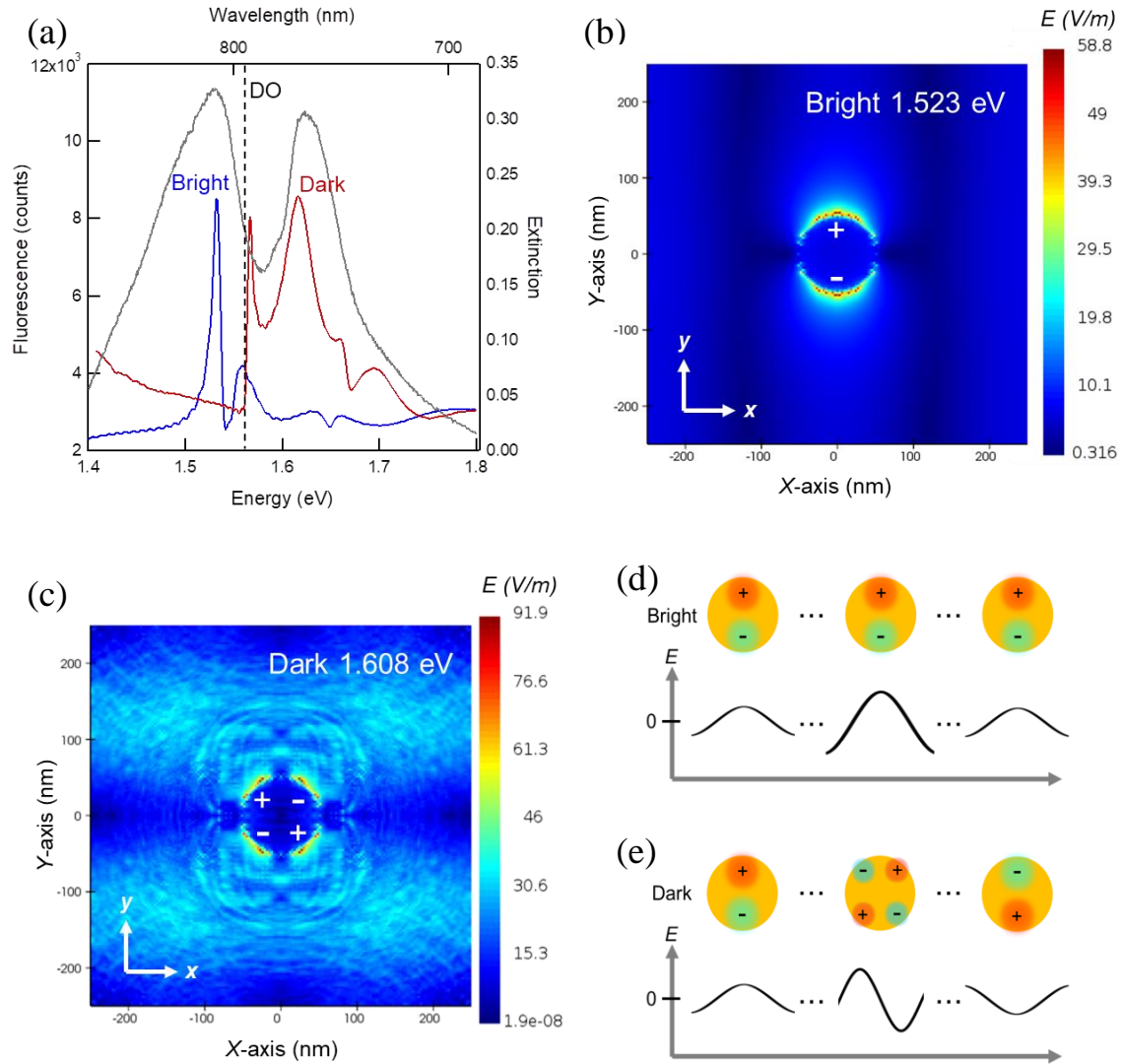


Figure 4-6 FDTD simulation of SLR modes. (a) Simulated extinction and scattering spectra of Au nanodisk array with lattice space of 500 nm. The diameter and height of the nanodisks are set as 100 nm and 75 nm, respectively. For bright extinction spectra, Bloch boundary conditions were used for the X and Y planes in the structural plane and plane wave was chosen as incident source. For dark scattering spectra, asymmetric boundary conditions were used for the X and Y planes in the structural plane and ten random dipoles were chosen as incident source. In order to attribute the mode, the scattering fields at a distance of 20 nm from the metal were monitored. The gray solid line in the figure is the fluorescence spectrum obtained in the experiment. (b) shows an electric field distribution of bright SLR mode appearing in the calculated extinction spectrum. (c) shows an electric field distribution of dark SLR mode appearing in the scattering spectrum. (d) and (e) indicates the excitation mechanism of bright and dark SLR modes. Bright SLR is supported by in-phase coherent interactions between particles. Dark SLRs, on the other hand, are supported by out-phase coherent interactions between particles.

The bright and dark modes of SLR were simulated using different approaches. The extinction spectrum of Au nanodisk arrays with lattice space of 500 nm under vertically irradiation of plane wave was calculated as I described in the experimental section. Bloch boundary conditions were used for the X and Y planes in the structural plane to consider the interaction between the diffractive scattering field and the LSPs. The peak position of calculated SLR (blue line in figure 4-6(a)) was in good agreement with the fluorescence (grey line) peak position on the low energy side. The electric field diagram showed bright SLR mode as expected as shown in figure 4-6(b).

As the next step, in order to prove the excitation of dark SLR mode, the periodic boundary conditions and light sources in FDTD calculation were changed. Generally, dark mode cannot be excited by a normal incidence because the dipole sum of the entire structure is close to zero. This is the reason why dark SLR modes is not observed in experimental set up. Under high concentration of dye molecules conditions, a large number of fluorophores are present over the metal surface. It is possible that these fluorophores act as a light source for exciting plasmons. The dark mode of SLR is formed by coherent interactions of opposite phase between adjacent particles. Therefore, these interactions were simulated by setting both the periodic boundary conditions of X-plane and Y-plane to asymmetric. A dipole derived from the dye molecules was chosen as the excitation light source. Ten dipole sources with random orientation, location, and phase excite the SLR modes with a 3.3 fs pulse at the beginning of the simulation. Field profiles were recorded after the simulation had run for 700 fs to filter out the excitation pulse. In this system, it is difficult to clearly separate absorption and scattering, so the plasmon mode was identified by monitoring the scattering field. The red line in figure 4-6(a) indicates the scattering spectrum simulated under the

asymmetric periodic boundary conditions with random dipole sources. The scattering spectrum showed two distinct peaks. One overlaps the spectrum of OD calculated under Bloch boundary conditions and corresponds to the OD due to lattice. The peak appearing at 1.608 eV was confirmed to be dark SLR mode of quadrupole type by the electric field distribution shown in figure 4-6(c). The calculated dark SLR mode scatter peaks match the fluorescence spectrum on the high energy side very well, providing the presence of a fluorescence enhancement process via the dark SLR. In addition, it was found that this dark mode was located at the dip (at 1.61 eV) of the extinction spectrum collected under normal incident condition.

The characteristics of the two modes are considered as follows. For a bright mode in figure 4-6(d), the phase across the array remains constant due to constructive interference of the counter-propagating radiation fields at each particle location. The amplitude at the edge, however, will be reduced to one half as there are no particles and, therefore, no radiation incident from the other side. For a dark mode in figure 4-6(e), particles in the array are driven by left- and right-propagating radiation fields, which destructively interfere at the particle locations, resulting in the creation of a standing wave node and a quadrupole excitation. As one moves away from the center, however, the destructive interference becomes gradually less complete due to unequal number of particles contributing to left- and right-propagating waves. This results in a buildup of dipole moments whose relative weight compared to the quadrupoles gradually increases when moving away from the center of the array. Importantly, for the dark mode the dipoles induced by the left- and right-propagating radiation fields are out of phase by π ; see figure 4-6(e). Thus, the dark mode in a finite lattice is different from the one in an infinite lattice: it features dipole moments and can, thus, be viewed as a hybrid mode

with characteristics of both the bright and dark modes of an infinite lattice. Surprisingly, the dark mode showed about twice stronger electric field than that of bright mode. Therefore, it is expected that the dark mode of SLR can dramatically improve the light-molecule interaction. This suggests that the dark mode can be used as various applications that assist photon condensation such as BEC. Au nanodisk structures with two SLR modes having narrow line width and strongly localized field may have laser characteristics. Thus, the excitation power dependence was measured for investigating the mechanism of enhanced fluorescence.

4.3.5 Stimulated Fluorescence via Dark and Bright SLR Modes

Figure 4-7(a) shows the excitation power dependence on the fluorescence spectra. From spectra, an intense and narrow fluorescence peaks at 1.61 and 1.52 eV, respectively, were observed with increasing excitation power. For both peaks, characteristic signatures of stimulated emission, such as rapid nonlinear increase of emission intensity and reduction of linewidth, were observed as increasing pump power (figure 4-7(b) and (c)). Since the line width of the bright mode is larger than that of extinction spectra ($= 0.1$) shown in figure 4-6(c) and the amount of decrease is small, it is considered that lasing has not occurred from this mode. On the other hand, the dark mode line width is below the calculated value, suggesting the possibility for lasing phenomena. This difference provides the intuition that dark mode can efficiently excite fluorescent molecules due to a larger mode volume than bright mode. Two possible reasons are considered for the lack of lasing in bright mode. One is the mismatch between the excitation wavelength and the maximum dye absorption. Detuning the excitation wavelength would suppress the efficient formation of population inversion of

dye molecules. The second is the influence of the surrounding environment. The non-uniform index of refractive index makes the SLR broader. However, since the dye concentration and the refractive index are in a trade-off relationship, so it is necessary to search for the optimum dye concentration condition for the system to be used. The results obtained here will be an important design guideline for the development of plasmonic lasers.

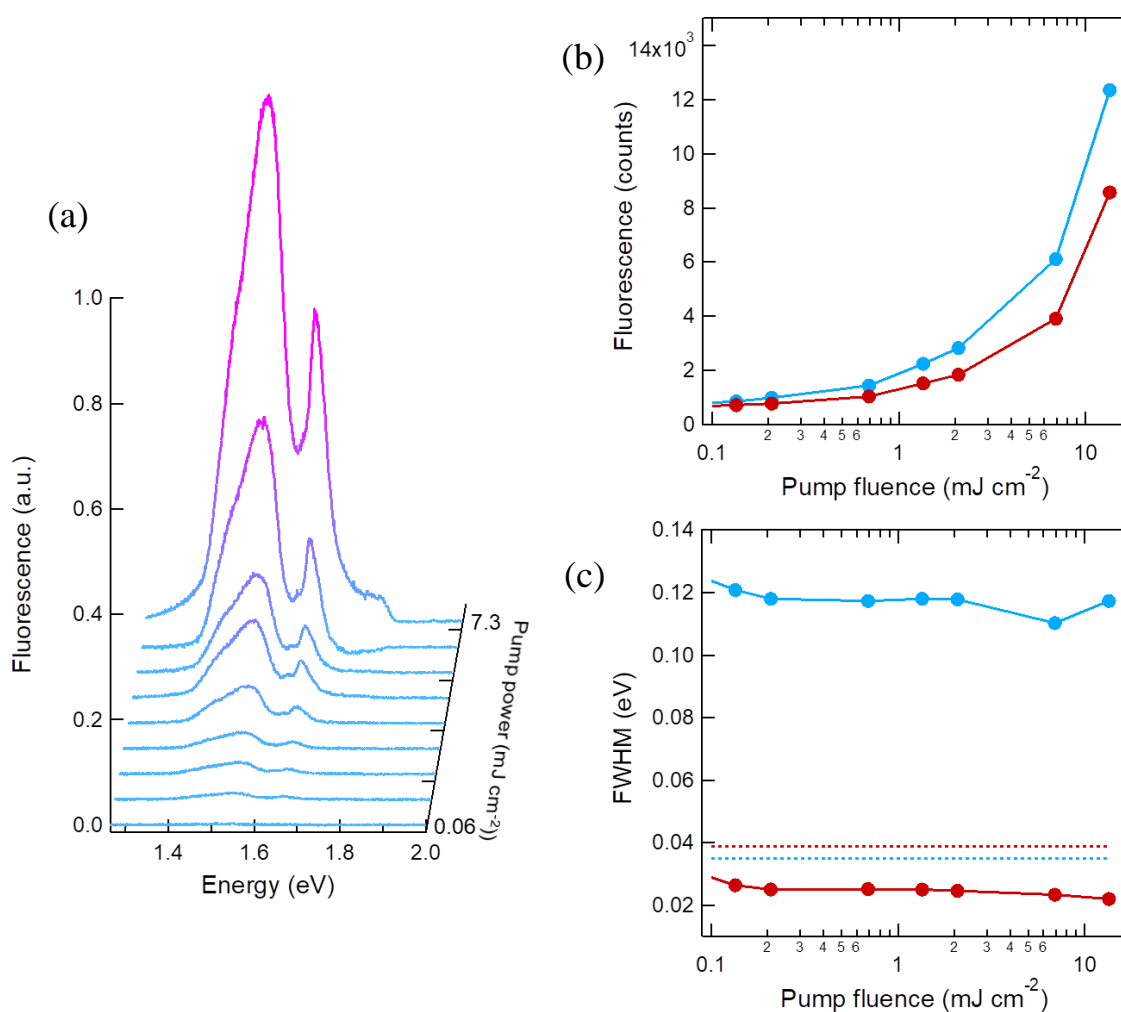


Figure 4-7. Stimulated emission below and above the threshold. (a) Fluorescence spectra, (b) the output powers and (c) the FWHM of the bright (blue dot) and dark (red dot) modes as a function of pump fluence. The blue and red dashed lines indicate the ideal line widths for bright and dark modes, respectively.

4.3.6 ECL through Dark and Bright SLR Modes

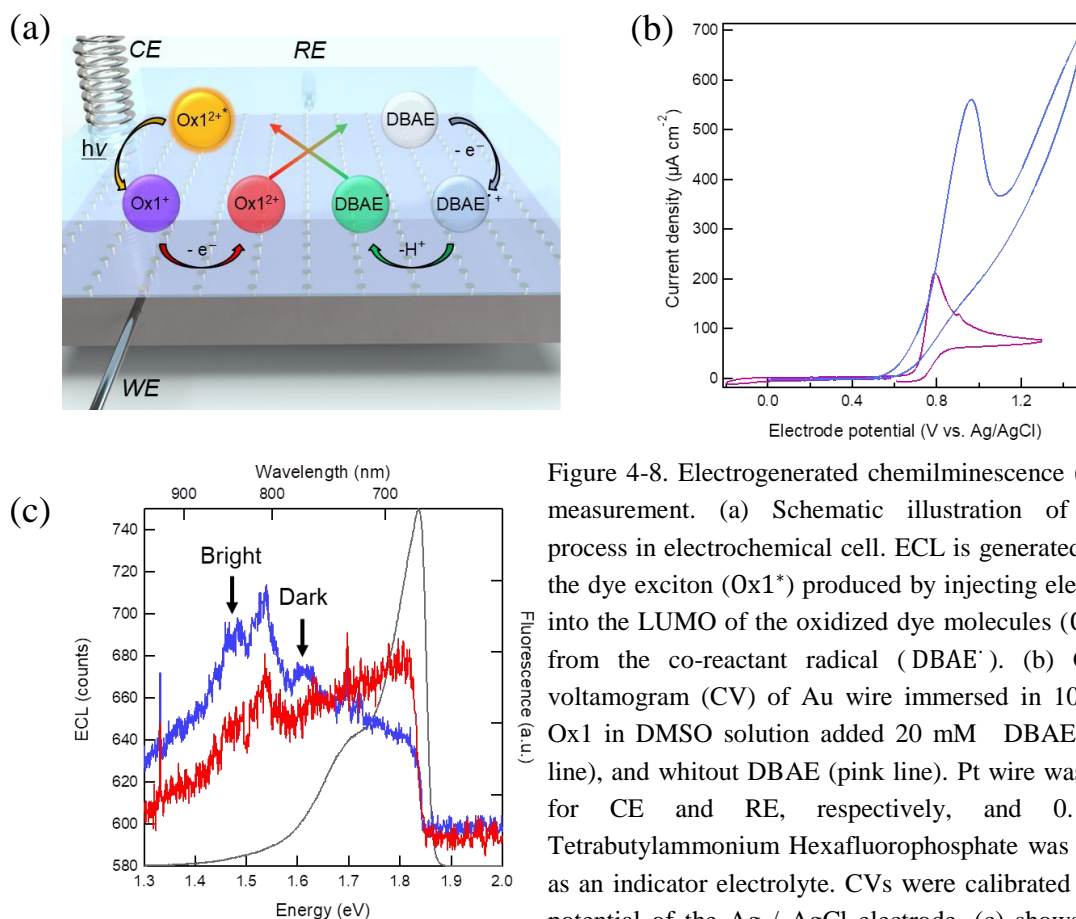
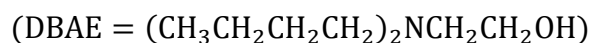
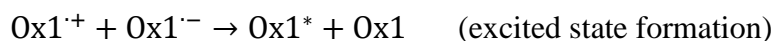
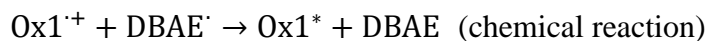
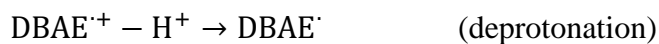
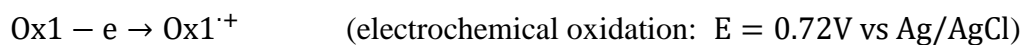
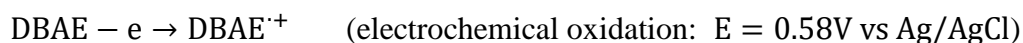


Figure 4-8. Electrogenerated chemiluminescence (ECL) measurement. (a) Schematic illustration of ECL process in electrochemical cell. ECL is generated from the dye exciton (Ox1^{2+*}) produced by injecting electrons into the LUMO of the oxidized dye molecules (Ox1^{+}) from the co-reactant radical (DBAE^{\cdot}). (b) Cyclic voltammogram (CV) of Au wire immersed in 100 μM Ox1 in DMSO solution added 20 mM DBAE (blue line), and without DBAE (pink line). Pt wire was used for CE and RE, respectively, and 0.1 M Tetrabutylammonium Hexafluorophosphate was added as an indicator electrolyte. CVs were calibrated to the potential of the Ag / AgCl electrode. (c) shows ECL spectra collected on Au nanodisk array (blue) and on no structure deposited area (red.).

Finally, I have attempted to apply the dark mode for the efficient electrochemical reactions. Here, the electrogenerated chemiluminescence (ECL) of an Ox1 supported Au nanodisk array with lattice space of 500 nm was demonstrated. The electrochemical cell was filled with 0.01 M KNO_3 aqueous solution containing 20 mM DBAE and 10 mM NaClO_4 . In general ECL systems, Tripropylamine (TrPA) is often used as a co-reactant. However, DBAE is much preferred from the point of view of its low toxicity and high redox potential of DBAE^{\cdot} free radical (-2.0 V vs Ag/AgCl).^{18,19} It is well known that ECL is produced by following the reaction pathway;



From the cyclic voltammogram (CV) in DMSO solution, Ox1 has a redox wave of Ox1⁺ at about 0.72 V vs. Ag / AgCl and that of Ox1⁻ at about -0.78 V vs. Ag / AgCl. Both redox potentials are lower than those for DBAE (figure 4-8(b)). Therefore, ECL emission in positive potential sweeps was expected. Note that the CV shown in figure 4-8(b) was obtained in DMSO solution, however the CV in the figure 4-8(b) is calibrated to the potential of the Ag / AgCl electrode. Since the dye was broken as soon as it was oxidized, it was directly fixed to the substrate by the spin coating method instead of being dispersed in the liquid. ECL measurements were performed in aqueous solution to suppress the dissolution of Ox1. The ECL spectrum was collected with an exposure time of 20 sec during a cycle sweep of the structural potential from 0.4 V to 1.2 V with a rate of 100 mV sec⁻¹. Figure 4-8 (c) shows the ECL spectra collected with and without nanodisk during the potential sweep. Broad ECL spectrum was observed from no-Au nanodisk site as shown in red line of figure 4-8(c). The concentration of

Ox1 was so high that the S1 transition is strongly suppressed by energy transfer between Ox1 molecules, such as the fluorescence measurement in 50 mM condition. Although the light intensity provided by ECL is very weak, it is considered to be the emission of Ox1 excitons through the same process as the light excitation process because it is well consistent with the fluorescence spectrum of Ox1 in the DMSO solution shown in gray line of figure 4-8(c). Interestingly, the ECL collected on Au nanodisk arrays showed enhanced ECL emission due to the bright and dark SLR modes shown as the blue line of figure 4-8(c). This result would support the fact that the bright and dark modes of SLR may access to modulation of chemical reactions. If the absorption band of the dye molecules is adjusted to these SLR modes, it is expected that the energy level will be modulated via strong coupling. Since this phenomenon leads to modulation of the enhanced region, it is considered that the chemical reaction characteristics are dramatically controlled through SLR modes. Furthermore, it is expected to develop a highly sensitive ECL sensor by changing the dye for weak coupling to a specific dye having a stable oxidant in the solution. The two coherent modes of SLR would not only offer the wonderful possibilities mentioned above but also open new doors for the ultimate light condensation using nonlinear optics such as polariton lasers and BEC.

4.4 Conclusion

In this section, detailed investigation of the bright and dark SLR excitation conditions induced in the square lattice of Au nanodisk arrays was carried out. The Au nanodisk array, controlled by EBL and low temperature annealing, supported SLR with a high Q-factor by using a PMMA thin film layer to homogenize the surrounding environment. From the angle-resolved extinction measurement, it was predicted that the Ox1 dye-doped system would exhibit enhanced fluorescence only via the plasmon electric field. The extinction and fluorescence measurements using various concentrations of dye molecules clearly show that dark SLR modes emerge under high concentration conditions above 50 mM and then the dark mode can access the fluorescence enhancement process. Dark SLR was defined by FDTD calculations using dipole sources and anti-symmetric periodic boundary conditions. From calculated results, the dark mode of SLR was found to be a excitation of the quadrupole mode through the coherent interactions of opposite phase between particles. And also, it was found that the high concentration is also important factor for such mode. The calculated results support the experimental results. Bright mode and dark mode provide stimulated emission and are expected to be applied to the development of plasmon lasers. Furthermore, it was found that these modes are strongly dependent on the lattice spacing, and enhanced fluorescence is emitted via the dark mode in the region where the LSP does not overlap the absorption band of the fluorescent dye. These detailed studies of the dark mode excitation conditions will greatly improve the range of applications for dark mode. As demonstrated finally, ECL emissions via both modes will open new doors for the ultimate light condensation using nonlinear optics such as polariton lasers and BEC.

4.5 References

- (256) Hummer, T., Garcia-Vidal, F. J., Martin-Moreno, L. and Zueco, D. *Phys. Rev. B*, **87**, 115419 (2013).
- (257) Torma, P. and Barnes, W. L. *Rep. Prog. Phys.*, **78**, 013901 (2015).
- (258) Chikkaraddy, R. *et al. Nature*, **535**, 127–130 (2016).
- (259) Santhosh, K., Bitton, O., Chuntunov, L. and Haran, G. *Nat. Commun.*, **7**, 11823 (2016).
- (260) Martikainen, J. P., Heikkinen, M. O. J. & Torma, P. *Phys. Rev. A*, **90**, 053604 (2014).
- (261) Khurgin, J. B. *Faraday Discuss*, **178**, 109–122 (2015).
- (262) Zou, S., Janel, N. and Schatz, G. C. *J. Chem. Phys.*, **120**, 10871–10875 (2004).
- (263) Garcia de Abajo, F. J. *Rev. Mod. Phys.*, **79**, 1267–1290 (2007).
- (264) Kravets, V. G., Schedin, F. and Grigorenko, A. N. *Phys. Rev. Lett.*, **101**, 087403 (2008).
- (265) Auguie, B. and Barnes, W. L. *Phys. Rev. Lett.*, **101**, 143902 (2008).
- (266) Vakevainen, A. I. *et al. Nano Lett.*, **14**, 1721–1727 (2014).
- (267) Shi, L. *et al. Phys. Rev. Lett.*, **112**, 153002 (2014).
- (268) Zhou, W. *et al. Nat. Nanotechnol.*, **8**, 506–511 (2013).
- (269) Yang, A. *et al. Nat. Commun.*, **6**, 6939 (2015).
- (270) Hakala, T. K. *et al. Nat Commun.*, **3**, 13687 (2017).
- (271) Palik, E. D. (ed.) in *Handbook of Optical Constants of Solids* vol. 1–3 (Academic Press Inc, 1991).
- (272) Zhou W. and Odom W. T. *Nat. Nanotechnol.*, **6**, 423–427 (2011)
- (273) Miao, W. *Chem. Rev.* **108**, 2506 (2008).
- (274) Walker K. E., Vanden Bout D. A. and Stevenson J. K. *J. Phys. Chem. C*, **115**, 2470–2475 (2011)
- (275) Zhou, W., Dridi, M., Suh, J. Y., Kim, C. H., Co, D. T., Wasielewski, M. R., Schatz, G. C., Odom, T. W. *Nat. Nanotechnol.*, **8**, 506–511 (2013).
- (276) Figotin, A., Vitebskiy, Waves in Random and Complex Media 2006, 16, 293–382 (2006).
- (277) Krauss, T. F. *Nat. Photonics*, **2**, 448–450 (2008).

- (278) Han, D., Lai, Y., Zi, J., Zhang, Z. Q., Chan, C. T. *Phys. Rev. Lett.*, **102**, 123904 (2009).
- (279) Weick, G., Woollacott, C., Barnes, W. L., Hess, O., Mariani, E. *Phys. Rev. Lett.*, **110**, 106801 (2013).

Chapter 5

Creation of Ultra-strong Light-Matter Coupling Regime of Cyanine Dye Supported Plasmonic Crystal

5.1 Introduction

The interaction between light and quantum emitters such as excitons depends on the local density of electromagnetic (EM) modes as I introduced in chapter 1. Increasing the density of EM modes, e.g., by using optical cavities, can facilitate faster energy transfer between the electronic material-excitations and the EM fields, leading to a variety of interesting physical phenomena such as the Purcell enhancement¹ where the lifetime of excited states is reduced, leading to brighter light emission. When the rate of energy exchange between the excitons and the local EM modes becomes higher than their individual decay and decoherence rates, hybrid light–exciton states called as the strong coupling emerge with new and exciting mixed properties of light and matter.^{2,3} Unlike photons, these hybrid light–matter states can collide and scatter through polariton–polariton and polariton–exciton interactions.⁴ Therefore, hybridization leads to population-dependent nonlinearities which can result in extreme photon condensation and macroscopic coherence of the hybrid states and of the emitted light.² In addition to the photon condensation, these unique optical characteristics can provide noble applications, such as the generation of low threshold coherent emission at room temperature without the need for population inversion,^{5,6} parametric amplification of optical signals,⁷ and ultrafast switching.^{8,9} In the field of plasmonics, strong coupling systems have been actively studied toward light condensation into nanospace. Since the

strong coupling strength strongly depends on the mode volume of photon, single metal nanoparticles or near-field coupled nanoparticle assemblies has been often used as light sources.¹⁰⁻¹⁶ Because these structures have a potential ohmic-loss due to the permittivity,¹⁷ the Q-factor and coherency are reduced and the coupling constant is limited. On the other hand, the SLR induced in plasmonic crystals has large Q-factor, high coherence and enhanced electric field, so the coupling strength can be significantly improved when the SLR is applied to strong coupling system.¹⁸⁻²⁰

In this chapter, the optical properties of a strong coupling system consisted of SLR and cyanine dye molecules were investigated. The coupling constant was improved up to 495 meV and the coupling state was modulated to the ultra-strong coupling region. These results will be important structural design guidelines for optical aggregation, which will be introduced in the next chapter.

5.2 Experimental Method

Preparation and Optical Analysis of Strong Coupling Regime

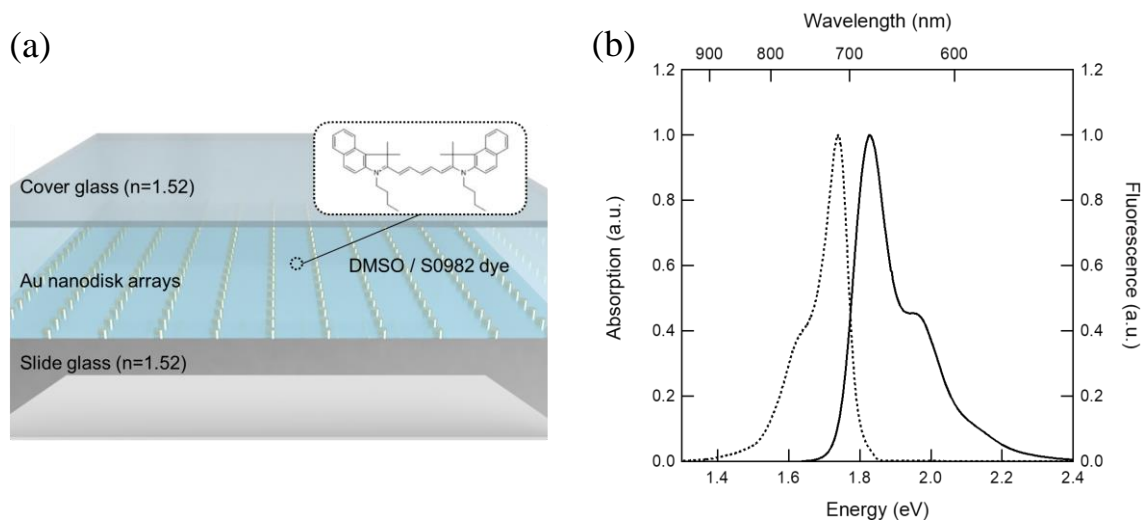


Figure 5-1. (a) Schematic illustration of cyanine dye-supporting Au lattice structures. In order to create the uniform environment, 5 μL of S0982/DMSO solution was dropped on the square lattice of Au nanodisk arrays shown in chapter 2 and 4. The solution was covered with a cover glass to prevent from evaporating the solution. (b) shows the absorption (solid line) and fluorescence (dashed line) spectra of S0982 cyanine dye molecule in acetonitrile. In acetonitrile, the absorption maximum of S0982 is observed at 1.83 eV (678 nm) and the fluorescence maximum is observed at 1.74 eV (713 nm).

Strong coupling regime was prepared by drop casting of a 5 μL of S0982/DMSO solution on the square lattice of Au nanodisk arrays as used in chapter 2 and 4. The substrate was covered with a cover glass to avoid the evaporation of the solution. The refractive index of the environment in the system was unified to 1.52 shown in figure 5-1(a). The formation of strong coupling states was confirmed by the angle-resolved extinction measurements and fluorescence measurements. In fluorescence measurements, The excitation wavelength was changed to 640 nm and filtered using a 532 nm short-pass filter and a 650 nm long-pass filter. The fluorescence spectrum was filtered by a 715 nm long pass filter to reduce the effect of the light source. The light source power was adjusted using a $\lambda/2$ plate and an ND filter.

5.3 Results and Discussion

5.3.1 Establishment of Strong Coupling Regime

Figure 5-2 (a) shows the extinction spectra of Au nanodisk arrays prepared on a glass substrate. The structure has a bright mode of SLR with a large Q-factor (see chapter 4). When a 5 mM S0982 cyanine dye molecule was dropped on the structures, they showed clear spectral splitting was observed at the maximum absorption energy as shown in figure 5-2(b). Mathematical analysis using anti-cross plots helps to understand strong coupling state. To confirm the formation of strong coupling states, the split positions observed after dye supporting were plotted against the SLR peak positions which were observed in DMSO solution without dye. As shown in Figure 5-2 (c), the split peaks showed anti-crossing behavior at the intersection of the dye absorption maximum and the SLR of the structure with lattice space of 400 nm. From the intersection of the anti-cross plot, the splitting energy was estimated to be 131 meV. Since this splitting energy is larger than the average value of FWHM of SLR and dye, it can be said that a strong coupling was formed between S0982 and lattice structures using the judgment conditions of Jaynes–Cummings.²³

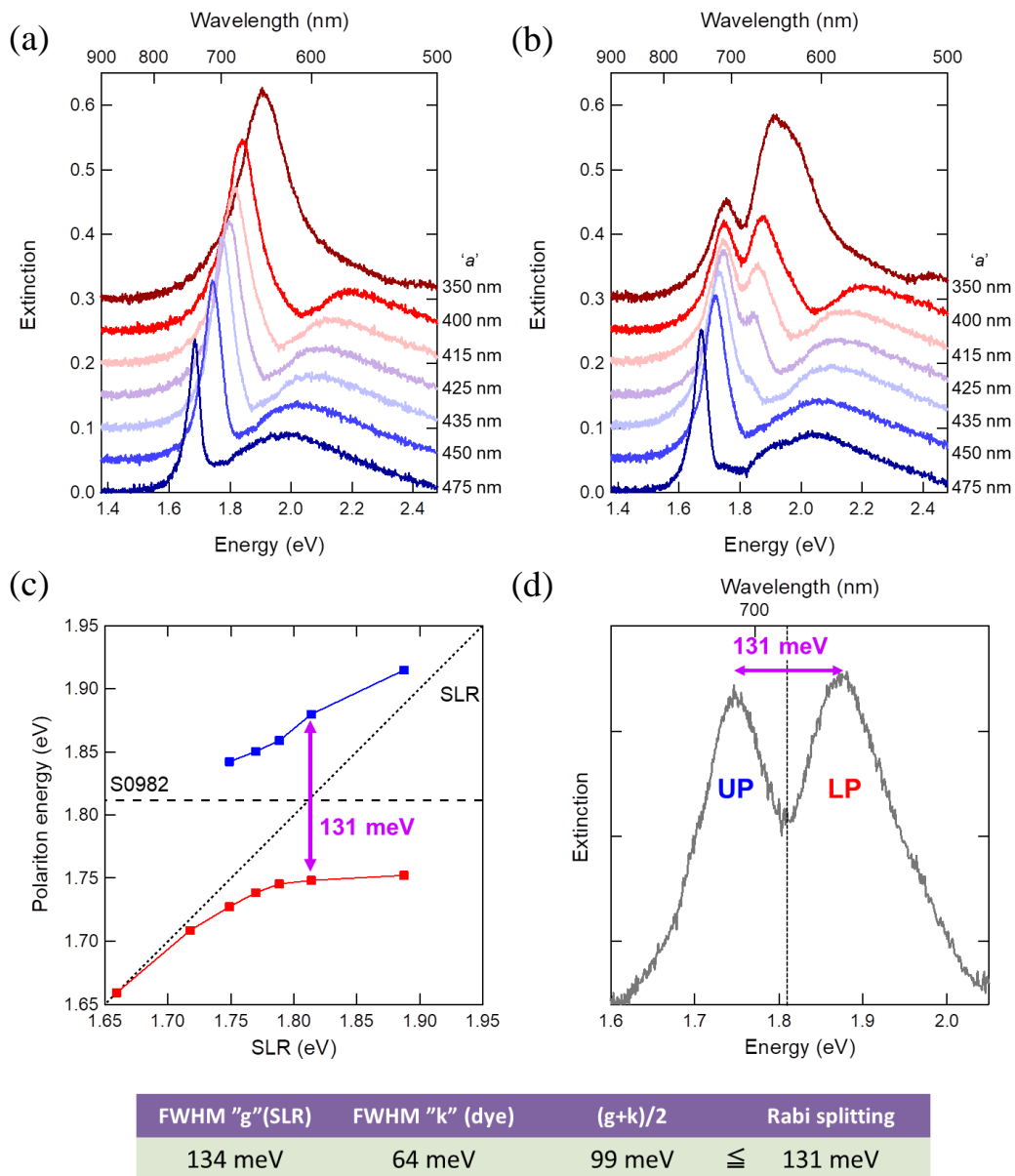


Figure 5-2. Extinction spectra of (a) DMSO and (b) 5mM S0982/DMSO coated Au lattice structures under normal incidence with incident angle of 0° . (c) Anti-crossing plot of dye-supported substrate shown in (b). The broken line in the figure is the maximum absorption position of the S0982 dye monomer, and the solid line shows the SLR position. Rabi splitting of 131 meV was clearly observed at the crossover point. (d) Extinction spectra of Au nanodisk arrays with lattice spacing of 400 nm. Since the division width is larger than the average FWHM of SLR and dye, it can be said that it is a true Rabi splitting.

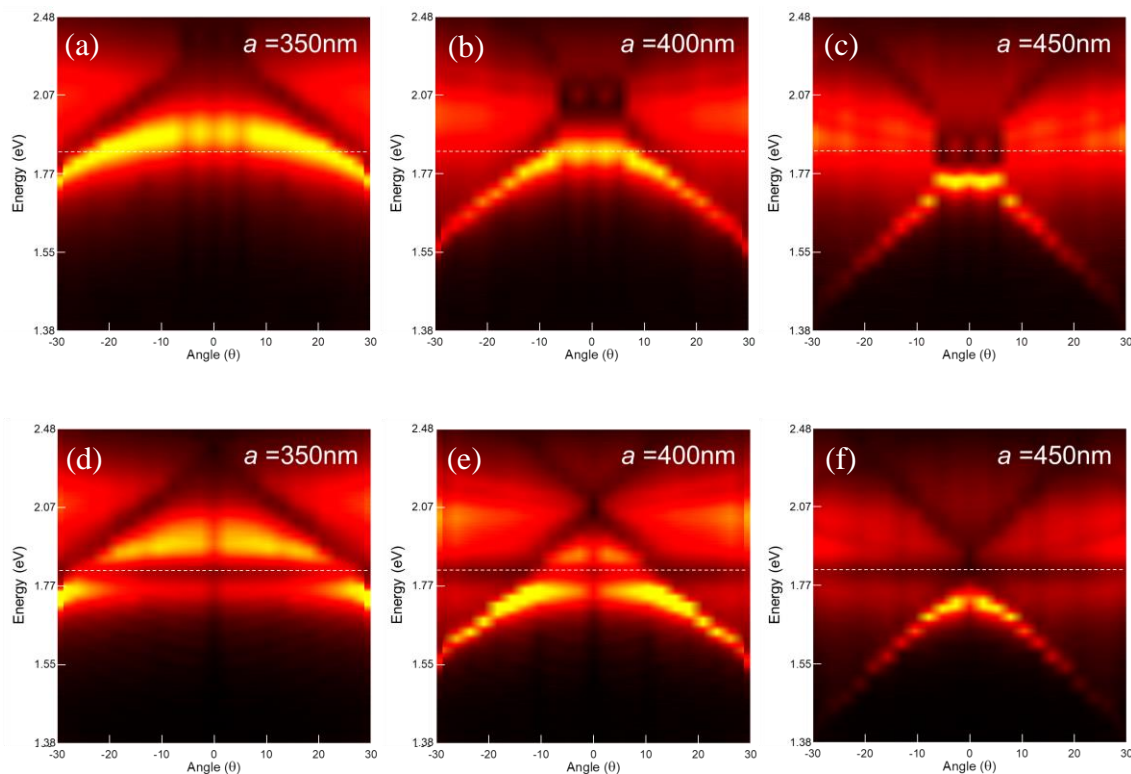


Figure 5-3. Angle resolved extinction spectra of (a-c) DMSO and (d-f) 5mM S0982/DMSO coated Au lattice structures. The lattice spacing are shown in the upper right of each graph.

SLR have a photonic band via coupling diffracted light and LSPs as I described in chapter 1, so it should be mentioned that the new hybridized modes also depends on the incident momentum. The incident moment dependence on the strong coupling states was confirmed by angle-resolved extinction measurement. As shown in Figure 5-3 (a)-(c), Au nanodisk arrays show a unique SLR angular dependence characterized by the lattice spacing. After depositing a dye solution, it was confirmed that the angular dispersion was maintained and, when it intersected with the absorption maximum of the dye, led to energy splitting due to the formation of strong coupling states (as shown in figure 5-3(d)-(f)). Since the relative mass of excitons in a strongly coupled dye molecule depends on the coupling strength, observed behaviors provide that these values can be significantly changed by modulating the incident angle. These phenomena not only change the energy level of the molecule, but can also modulate the unique de Broglie wavelength.

5.3.2 Ultra-Strong Coupling with Plamonic Lattice Structure

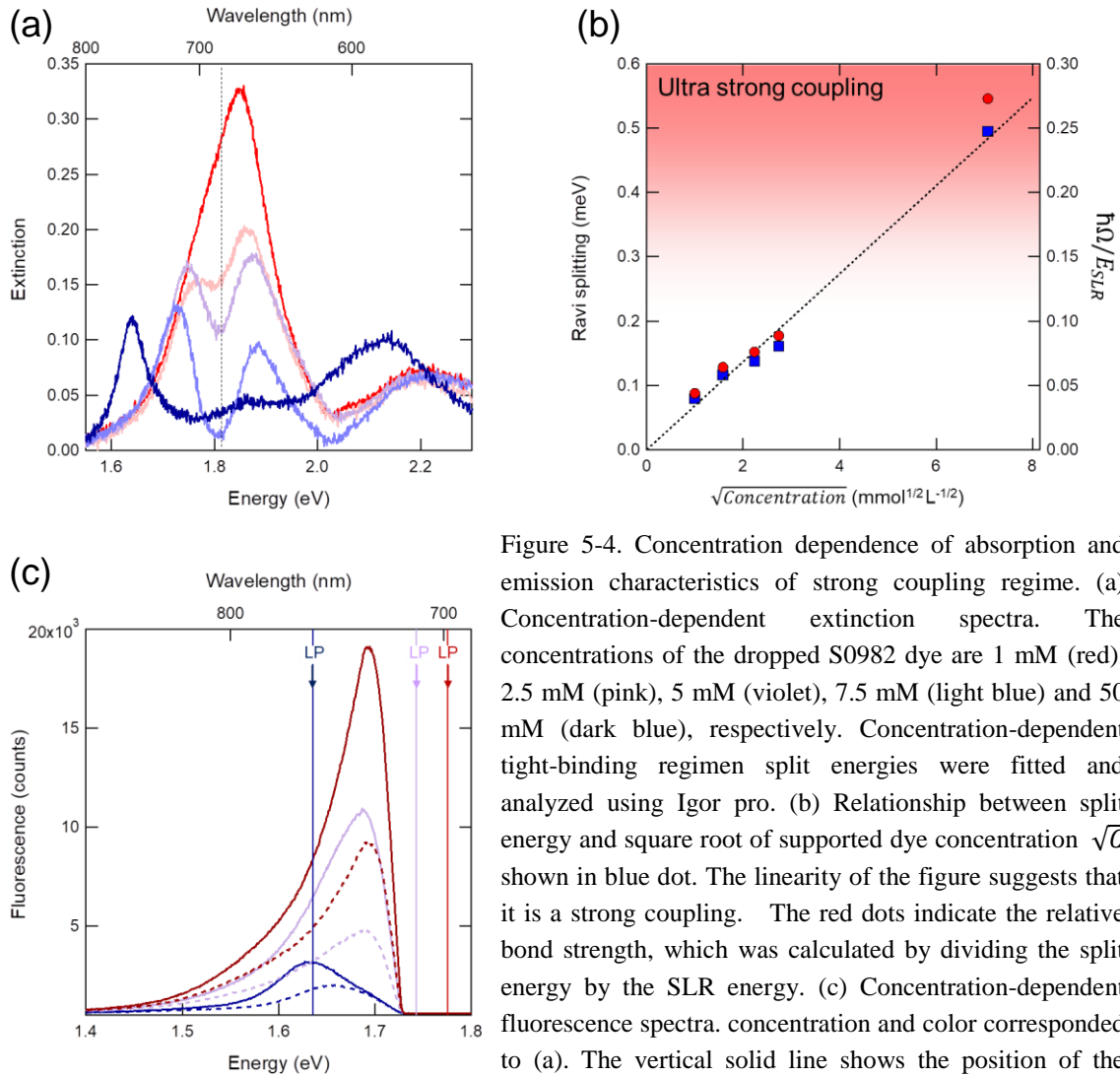


Figure 5-4. Concentration dependence of absorption and emission characteristics of strong coupling regime. (a) Concentration-dependent extinction spectra. The concentrations of the dropped S0982 dye are 1 mM (red), 2.5 mM (pink), 5 mM (violet), 7.5 mM (light blue) and 50 mM (dark blue), respectively. Concentration-dependent tight-binding regimen split energies were fitted and analyzed using Igor pro. (b) Relationship between split energy and square root of supported dye concentration \sqrt{C} shown in blue dot. The linearity of the figure suggests that it is a strong coupling. The red dots indicate the relative bond strength, which was calculated by dividing the split energy by the SLR energy. (c) Concentration-dependent fluorescence spectra. concentration and color corresponded to (a). The vertical solid line shows the position of the lower polariton.

Next, the dye concentration dependence of the system was investigated. In order to reduce the angular dispersion originated from the incident light, the incident angle was fixed at 0° . Under these measurement conditions, the structure with a lattice spacing of 400 nm was considered to be appropriate for the strongest coupling formation. Figure 5-4 (a) shows the extinction spectra of Au nanodisk array with lattice spacing of 400 nm depending on the dye concentration. The dye concentration was changed from 1 to 50 mM. As the concentration increased, the system showed a

suppression of extinction intensity and increase of splitting energy. In the strong coupling regime, the split energy was proportional to the square root of the number of dye molecules (C) in the mode volume.²³ As shown in figure 5-4(b), splitting energy was linearly changed up to 495 meV against \sqrt{C} . When the relative coupling strength was calculated, which can be measured by the ratio between the energy of the cavity and the Rabi splitting energy, that value was 0.27. If coupling strength ratio was larger than 0.1 to 0.2, the system was recognized as the ultra-strong coupling (USC) regime.²⁰ The USC regime can provide new phenomena such as photon blockades,^{24,25} superradiance²⁶ and ground state modifications.^{27,28} Based on the results in figure 5-4, it can be said that the present system can control from the strong coupling to USC regime. It is predicted that the sample prepared in this experiment also possesses unique optical characteristics. The fluorescence of these systems was measured using a 100 fs laser with an excitation wavelength of 640 nm. Amplified fluorescence spectra were observed at 1 and 5 mM concentrations due to enhanced S1 transition of the dye. Unlike the stimulated emission which was observed in chapter 4, the spectral shape did not change because the strong coupling level and the fluorescence spectrum of the dye were not overlapped. On the other hand, a clear shift in the fluorescence spectrum was observed under the USC condition. The maximum position of the shifted fluorescence with the position of the lower polariton of the USC was coincident. This means that the strong binding level was switched to the main process of fluorescence. Since USC has a large number of dark exciton reservoirs, low threshold lasers are expected.

The emission characteristics of USC were investigated by changing the excitation power intensity. As shown in Figure 5-5, USC showed a non-linear increase of fluorescence with the low threshold of 0.4 mJ cm^{-2} and decrease of FWHM. From

this, it was suggested that the luminescence process transitioned from spontaneous emission to laser. There are two possible reasons for the low threshold laser transition. One is that energy transfer to dye molecules was suppressed. The USC lower polariton is located on the lower energy side of the absorption band of the unbound dye. Light energy is carried from the majority of dark exciton reservoirs to the lower polariton with low loss via strong coupling. It was thought that it was easy to form a population inversion. Secondly, the influence of SLR can be considered. SLR provides a large coherent wave. The coupled dye molecules with SLR also retain its coherent properties, making it easier to activate stimulated emission. The results obtained in the experiment are expected to enable the development of low-threshold polariton lasers and to develop the process of photon condensation via coherent coupling.

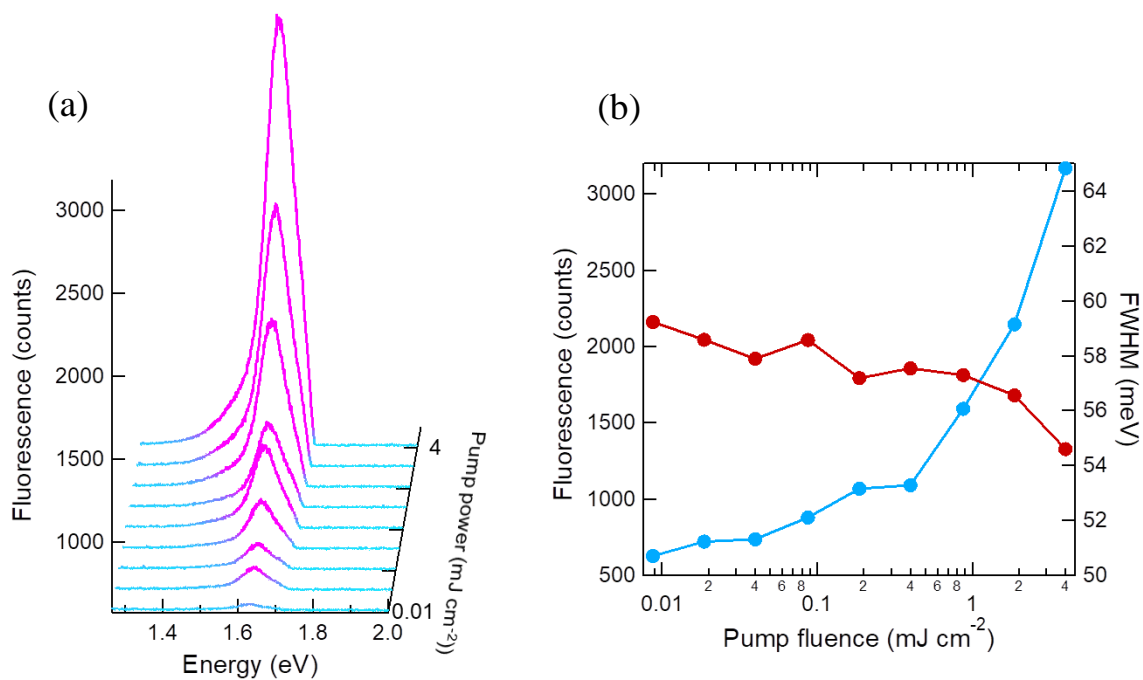


Figure 5-5. Stimulated emission below and above the threshold. (a) Fluorescence spectra from lower polariton state in the ultra-strong coupling (USC) system between S0982 and Au nanodisk array with lattice space of 400 nm. (b) The output powers (blue dot) and the FWHM (red dot) of the fluorescence from USC regime as a function of pump fluence.

5.4 Conclusion

In this chapter, the formation of the strong coupling state between SLR mode of plasmonic crystals with high Q factor and S0982 cyanine dye was demonstrated. The strong coupling regime was easily prepared by the simple coat of dye molecules on the structure-supported substrate. In the system, the formation of new hybrid levels showing anti-crossing behavior was observed. Using the Jaynes-Cummings model, these splits have been proven to be distinct Rabi splitting due to strong coupling formation. Furthermore, the angle-resolved extinction measurements confirmed that the newly formed polariton state had an angular variance, proving that it was a hybrid mode with SLR. The concentration dependence of the optical properties was investigated for the system using Au nanodisk array with lattice space of 400 nm, which shows the strongest coupling with S0982 under the incident angle of 0° . The Rabi splitting energy of this system was linearly modulated depending on the square root of the dropped dye concentration. In addition, the calculated relative coupling strength provided me that the system transitioned from strong coupling state to the USC with a dye concentration of 50 mM. The USC showed clear luminescence from the polariton level as the shift amount at the Lower polariton level exceeded the absorption band of the dye. It was observed that the emission from the polariton level showed a non-linear response at a low threshold value at the incident power of 0.4 mJcm^{-2} . The USC with a mode of two-dimensional propagating light such as SLR would provide supercondensation of photons through coherent interactions like BEC. In addition, these results suggest that the strong coupling is very effective as a photon reservoir. if it can be combined with the defect level of plasmonic crystals, it may be possible to confine light via a new approach.

5.5 References

- (280) Goy, P. Raimond, J. M. Gross, M. Haroche, S. *Phys. Rev. Lett.*, **50**, 1903–1906 (1983).
- (281) Deng, H. Haug, H. Yamamoto, Y. *Rev. Mod. Phys.*, **82**, 1489–1537 (2010).
- (282) Törmä, P. Barnes, W. L. *Rep. Prog. Phys.*, **78**, 13901 (2015).
- (283) Tassone, F. Yamamoto, Y. *Phys. Rev. B: Condens. Matter Mater. Phys.*, **59**, 10830–10842 (1999).
- (284) Daskalakis, K. S. Maier, S. A. Murray, R. Kéna-Cohen, S. *Nat. Mater.*, **13**, 271–278 (2014).
- (285) Plumhof, J. D. Stöferle, T. Mai, L. Scherf, U. Mahrt, R. F. *Nat. Mater.*, **13**, 247–252 (2014).
- (286) Saba, M. Ciuti, C. Bloch, J. Thierry-Mieg, V. André, R. Dang le, S. Kundermann, S. Mura, A. Bongiovanni, G. Staehli, J. L.; *et al. Nature*, **414**, 731–735 (2001).
- (287) Vasa, P. Pomraenke, R. Cirmi, G. De Re, E. Wang, W. Schwieger, S. Leipold, D. Runge, E. Cerullo, G. Lienau, C. *ACS Nano*, **4**, 7559–7565 (2014).
- (288) Vasa, P. Wang, W. Pomraenke, R. Lammers, M. Maiuri, M. Manzoni, C. Cerullo, G. Lienau, C. *Nat. Photonics*, **7**, 128–132 (2013).
- (289) Bellessa, J. Symonds, C. Vynck, K. Lemaitre, A. Brioude, A.; Beaur, L.; Plenet, J.; Viste, P.; Felbacq, D. Cambril, E. *et al. Phys. Rev. B: Condens. Matter Mater. Phys.*, **80**, 033303 (2009).
- (290) Zengin, G. Johansson, G. Johansson, P. Antosiewicz, T. J. Käll, M. Shegai, T. *Sci. Rep.*, **3**, 3074 (2013).
- (291) Chantharasupawong, P. Tetard, L. Thomas, J. *J. Phys. Chem. C*, **118**, 23954–23962 (2014).
- (292) Zengin, G. Wersäll, M. Nilsson, S. Antosiewicz, T. J. Käll, M. Shegai, T. *Phys. Rev. Lett.*, **114**, 157401 (2015).
- (293) Sugawara, Y. Kelf, T. Baumberg, J. Abdelsalam, M. Bartlett, P. *Phys. Rev. Lett.*, **97**, 266808 (2006).
- (294) Fofang, N. T. Park, T.-H. Neumann, O. Mirin, N. A. Nordlander, P. Halas, N. J. *Nano Lett.*, **8**, 3481–3487 (2008).

- (295) Schlather, A. E.; Large, N. Urban, A. S. Nordlander, P. Halas, N. J. *Nano Lett.*, **13**, 3281–3286 (2013).
- (296) Wang, F., Shen, Y. R. *Phys. Rev. Lett.*, **97**, 206806 (2006).
- (297) Väkeväinen, A. I. Moerland, R. J. Rekola, H. T. Eskelinen, A.- P. Martikainen, J.-P. Kim, D.-H. Törmä, P. *Nano Lett.*, **14**, 1721–1727 (2014).
- (298) Rodriguez, S. R. K.; Feist, J.; Verschuuren, M. A.; Garcia Vidal, F. J.; Gómez Rivas, J. *Phys. Rev. Lett.*, **111**, 166802 (2013).
- (299) Carusotto I. and Ciuti C. *Rev. Mod. Phys.*, **85**, 299–366 (2013).
- (300) Deng H., Weihs G., Snoke D., Bloch J. and Yamamoto Y. *Proc. Natl. Acad. Sci. U. S. A.*, **100**, 15318 (2003).
- (301) Wang J., Da P., Zhang Z., Luo S., Liao L., Sun Z., Shen X., Wu S., Zheng G. and Chen Z. *Nanoscale*, **10**, 10371–10376 (2018).
- (302) Jaynes E. T. and Cummings F. W. *Proc. IEEE*, **51**, 89–109 (1963).
- (303) Ridolfo A., Leib M., Savasta S. and Hartmann M. J. *Phys. Rev. Lett.*, **109**, 193602 (2012).
- (304) Hamsen C., Tolazzi K. N., Wilk T. and Rempe G. *Phys. Rev. Lett.*, **118**, 133604 (2017).
- (305) Vasanelli A., Todorov Y. and Sirtori C. *C. R. Phys.*, **17**, 861–873 (2016).
- (306) Jaako T., Xiang Z. L., Garcia-Ripoll J. J. and Rabl P. *Phys. Rev. A: At., Mol., Opt. Phys.*, **94**, 033850 (2016).
- (307) Martí'nez L. A., Ribeiro R. F., Campos G. A. J. and Yuen-Zhou J. *ACS Photonics*, **5**, 167–176 (2018).

Chapter 6

Energy Condensation into Defect Sites in Plasmonic Arrays for Efficient Light Utilization

6.1 Introduction

As introduced in chapters 1, plasmonic crystals have the relatively higher Q-factor¹⁻³ with two dimensionally scattered fields.^{4,5} From this fact, it can be expected that its character would lead to the specific light-matter interaction, such as weak- or strong-coupling regime over the entire two-dimensional space, resulting in the arbitrary tuning of the optical properties of materials, i.g. exciton energy level,^{6,7} emission rate,⁸⁻¹⁰ or energy transfer¹¹⁻¹³ etc. Therefore, precise control of such crystal would provide the development of low-threshold polariton lasers^{14,15} and modulation of photochemical reaction.^{16,17} Moreover, if the energy propagation property and/or the electric field gradient were able to be added into this coherent characteristic, it might open the door for a noble application, e.g., molecular trapping or the establishment of new photochemical reaction systems.

Both photonic crystals and plasmonic crystals have distinct optical properties, i.e., optical band, high Q-factor and high coherent.^{18,19} It is well known that, when a line or point defects are introduced into a photonic crystal, the defect level trigger the formation of the forbidden band at the bandgap shown in figure 6-1.^{18,19} Photon can transfer from the upper band edge to the defect level, but energy outflow from the forbidden band to upper or lower band edges cannot happen. Thus, as they can transfer or confine a single-mode light in the photonic crystal, line defects are often used as a

wave guide while point defects are applied as a Q-switch laser.^{18,19} On the other hand, regarding to the plasmonic crystals, there are only few papers which report about the introduction of defect sites for the light propagation and condensation.^{20,21} Because, unlike photonic crystals, light energy transfer from upper band to defect level will not occur in a plasmonic crystal because its upper band is dark at the Γ point (see chapter 1). In order to condense light into a specific site using plasmonic crystals, a new approach needs to be introduced into the system.

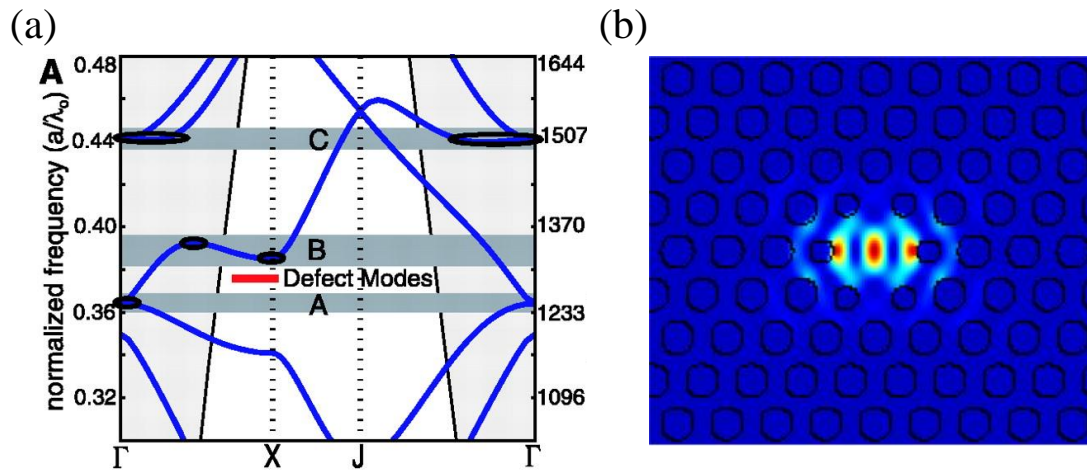


Figure 6-1. (a) Calculated 2D in-plane TM band structure of photonic crystal microcavity constructed from hexagonal-shaped Au-Ti array holes. The flat-band regions (A, B, and C) are indicated by dark gray horizontal bands. For devices with a central defect, the position of the highly localized defect modes is indicated by the thick red line. (b) Computed optical field magnitude superimposed on the microcavity.

Recent studies have reported that the strong coupling regime forms dark exciton states which play role as the photon reservoir in the polariton band,²²⁻²⁶ which significantly contributes to the decay of the lower polariton.²³ It is expected that this dark exciton will replace the upper band of plasmonic crystals. In this chapter, I introduce a new method to propagate and condense light energy into specific defect sites such as line or point introduced in plasmonic crystals. By the EBL method, line or point defects with the same size as the SLR wavelength λ_{SLR} (or $3/4$, $7/8$ and $9/8 \lambda_{\text{SLR}}$) were accurately prepared in the Au nanodisk arrays. The defect-doped Au nanodisk

array was structurally controlled to tune the S1 transition energy of dye to form the strong coupling with well-defined Rabi splitting. By exciting the system with a collimated laser and performing fluorescence measurements, the light propagation and condensation into controlled defects was observed simultaneously. The present new approach and phenomena described here will be useful technique for the fabrication guideline of plasmonic structures with the ultimate light confinement.

6.2 Experimental Method

The square lattice of the Au nanodisk array was fabricated on glass substrate by the EBL method. The width of line defect (w) was prepared in the center of the square lattice (see figure 6-2 (a)). The w values were matched with the SLR wavelength of each Au nanodisks arrays. FRET between the metal and the dye molecules was suppressed by supporting a 5 nm aluminum oxide layer on the surface of the metal with the ALD method. Then, the 1,2-dichloroethane containing 3 mM S0982 cyanine dye was spin-coated on the substrate to prepare a strong coupling regime. The collimated laser (λ : 642 nm) with spot size of $100 \mu\text{m}^2$ was illuminated at the edge site of the lattice structure with $50 \times 100 \mu\text{m}^2$ and fluorescence spectra were collected at a distance independent of the light source as shown in figure 6-2(b). Light propagation and condensation were evaluated by collecting the fluorescence from defective sites far from the excited position using the same inverted microscopic system shown in section 4.2.5. All fluorescence measurements were performed in water to tune the surrounding environment. By tuning the defect size with the SLR, the defect size can be seen as a confined mode of light.

6.3 Results and Discussion

6.3.1 Fluorescence on Au Nanodisk Arrays with Line Defects

Figure 6-2 (a) shows the precise controlled square lattices of Au nanodisk array with a line defect supported on the glass substrate. The w values were matched to the SLR wavelength of each structure with lattice space (a), where w were 629, 690, 713 nm for $a = 350, 400, 450$ nm, respectively. As in chapter 5, specific strong coupling states depending on the excitation angle were formed by supporting the S0982 dye ($\lambda_{\text{abs}} 690$ nm) on the structures (see figure6-2 (c)-(e)). In this system, the width w was varied as the lower, the same, and the higher length with respect to the maximum absorption wavelength of the dye. The exact design of this defect size allows us to understand the effect of line defects on the strong coupling states. From the fluorescence measurement set up, the qualitative information on the propagation and condensation of light energy can be obtained via the fluorescence intensity flow. Figure 6-2 (f)-(h) shows the fluorescence intensity flow of each structure. It is found that there was a clear difference depending on the lattice spacing. In the structure with $a = 350$ nm, a monotonous fluorescence intensity flow was observed from the left side to the right. Interestingly, the structure with $a = 400$ nm showed an enhanced fluorescence at the line defects while the structure with a of 450 nm showed a fluorescence suppression at the line defect after fluorescence intensity flow. These unique features provide us an important hypothesis about the effect of strong coupling on defects. In the structure with a lattice spacing of 350 nm, because the dye absorption and SLR are mismatched, the band near the Γ point is not modulated by the strong bond formation. Therefore, it is considered that the line defect functioned as a part of SLR and showed a monotonous fluorescence flow. On the

other hand, in the structure with lattice spacing of 400 and 450 nm, the absorption maximum of the dye and the SLR band overlap, leading to the specific modulation of optical characteristics due to the strong coupling formation. It has been reported that when the upper polariton is excited in the strong coupling regime, fluorescence is generated from the lower polaritons via a dark exciton reservoir with high optical density.²²⁻²⁶ If a defect level that was close to or overlaps with the dark exciton reservoir level was doped on the lattice structure, the energy flow to that level could be highly expected. Contrary, in the case for the defect level in the forbidden band of SLR mismatching to the energy level of the reservoir, it is predicted that no energy flow will occur because it cannot interact through the strong coupling state or SLR. The structure with a 400 nm was considered to benefit from the dark exciton reservoir because the defect level coincides with the maximum absorption of the dye. Whereas, the structure with a of 450 nm has a defect mismatched with the dye, so energy flow from the hybridized states cannot not be expected. From these reasons, it is suggested that the former showed enhanced fluorescence at defect sites due to light energy condensation and the latter showed fluorescence suppression at defective sites. If the light was trapped in a defect site, it could be expected to be a standing wave, like a photon in any other cavity. Therefore, it is necessary to investigate the effect of phase on whether the enhanced fluorescence from defects found in structures with a of 400 nm is derived from the defect mode.

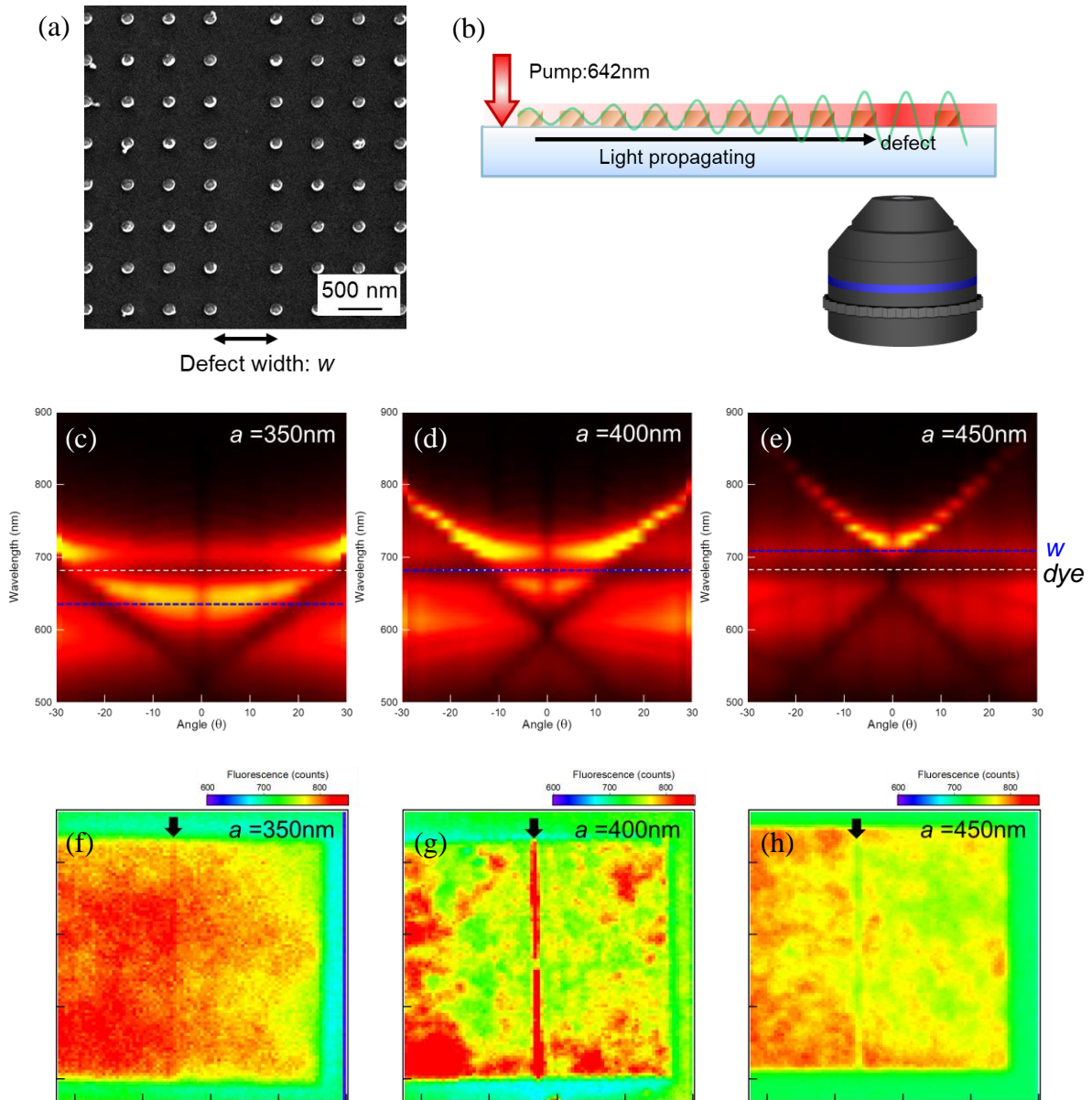


Figure 6-2. Fluorescence measurement of square lattice of Au nanodisk arrays with line defects. Structural properties of Au nanoprism arrays before and after annealing. (a) The SEM image of square arranged Au nanodisk array with lattice space (defined as a) of 400 nm. Fixed vacant line with width of w was introduced in the structure as a line defect. (b) Schematic illustration of fluorescent measurement system. The end of the structure was excited by a collimated 642 nm red-laser, and fluorescence at a position independent of the light source was captured by a 60x objective (NA 0.7). (c)-(e) represent the angle-resolved extinction spectra of S0982 cyanine dye supported Au nanodisk arrays. The white dashed line and blue dashed line in the figure indicate the maximum absorption position of the dye and the defect width w , respectively. (f)-(h) show the fluorescence image of line defect doped Au nanodisk array with various lattice spaces. $w = 629$ nm for $a = 350$ nm, $w = 690$ nm for $a = 400$ nm and $w = 713$ nm for $a = 450$ nm. The arrow at the top indicates the location of the defect.

6.3.2 Emission Behavior Depending on Defects Size

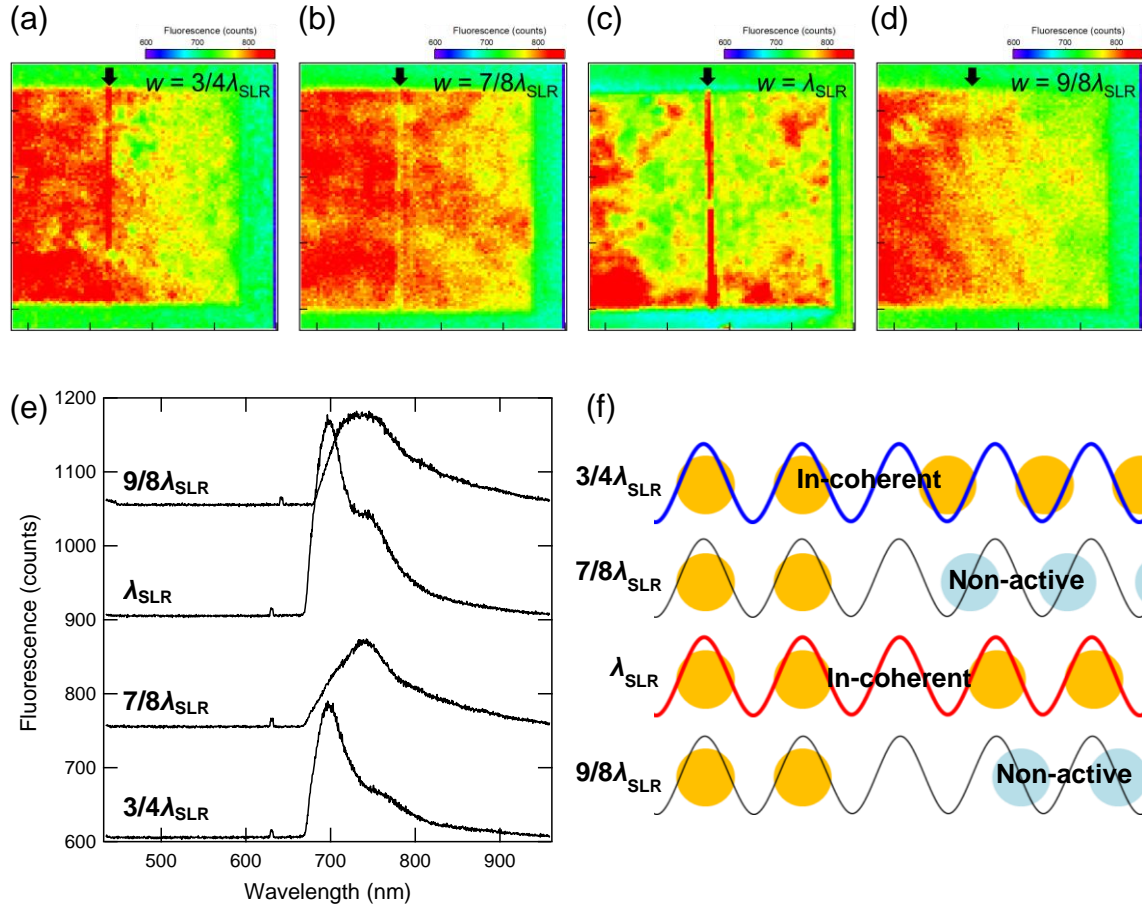


Figure 6-3. Defect width dependence of fluorescence spectrum induced in line defects. (a)-(d) show the fluorescence images of dye supported square lattice of Au nanodisk arrays with lattice space of 400 nm and a various defects width. Line defects width were controlled $3/4$, $7/8$, 1 and $9/8$ times of the SLR wavelength. The arrow at the top indicates the location of the defect. (e) indicates the fluorescence spectra from line defects. (f) is schematic illustration of enhancement and suppression mechanism of fluorescence at defects. If the defect width is a multiple of $1/4\lambda$, then all gold nanodisks are located in the SLR amplitude. Therefore, the coherence of the entire particle is maintained and a defect level is formed along the optical band. On the other hand, in the case of other line widths, the particles are randomly arranged with respect to the SLR, so that the particles are in a decoherent state and the defect mode is not formed.

The phase dependence of the defect mode was investigated by the change in the w of Au nanodisk array with lattice space of 400 nm to $3/4$, $7/8$, 1 and $9/8$ times of the SLR wavelength as shown in figure 6-3(a)-(d). The emission intensity from the defect was clearly dependent on the defect width, and enhancement was observed when

the defect width was a multiple of $1/4\lambda_{\text{SLR}}$ such as in (a) and (c), but not observed in (b) and (d). These results indicate that the matching of SLR phase and defect size is a very important factor for the light confinement effect. When the fluorescence spectra were taken from the defects, the enhanced spontaneous emissions due to the S1 transition of the dye ($\lambda_{\text{flu}} = 700 \text{ nm}$) were observed, indicating the light confinement. However, the structure having no confinement showed the broad and weak luminescence. From the fluorescence energy matching between the weak and strong coupling states, it can be considered that the weak emission comes from the lower polariton state. The difference in fluorescence spectra observed in each defect confirms that a fluorescence enhancement process originated from the defect mode. The major difference of fluorescence spectra is expected to attribute to the coherent interaction between the interparticles next to the defect. As shown in figure 6-3(f), it was found that Au nanodisk arrays form coherent waves in or out of phase across defects when the defect width was a multiple of $1/4 \lambda_{\text{SLR}}$. Since this interaction can support pure SLR, an optical band containing defect levels will be formed. Since the defect mode matches with the absorption maximum wavelength of the dye molecules, the light condensation into the defect can be produced an enhanced spontaneous emission. However, if the defect width deviates by $1/8 \lambda_{\text{SLR}}$, it is expected that the Au nanodisk array across the defect will not form a band throughout the system because it is located at the node of SLR polariton wave. Therefore, it is considered that only decoherent SLR was induced in these structures, leading to weak fluorescence from lower polariton and no light condensation. These important results are the first phenomena observed in the study of plasmonic crystals, and are important design guidelines for constructing a new system that can freely propagates and condensates light.

6.3.3 Light Condensation into Void Defects

Based on the results, I have demonstrated the two-dimensional light propagation and light confinement into the specific area. When a hexagonal lattice is used for the plasmonic crystal, two-dimensional light propagation can be realized. As shown in Figure 6-4 (a), a hexagonal lattice of Au nanodisk arrays with a lattice spacing of 425 nm was fabricated on the glass substrate. Both the disk diameter and the film thickness were designed to be 100 nm. As a defect, point voids comparable to the SLR wavelength were accurately placed in the center of the structure as shown in figure 6-4(b). Similar to the previous experiment, strong coupling states having 128 meV of Rabi-splitting were formed by supporting the S0982 dye on the lattice structure. In addition, in order to suppress the energy propagation due to the interaction of the dye itself, the supported dye amount was 1/3 of the previous experiment. Figure 6-4 (d) is a fluorescence image acquired with the optical system as described above. Apparently, it can be confirmed that the light energy was transferred two-dimensionally from the excited site (left side of the image) and concentrated at the defective site. Since there was no significant difference in emission intensity between the excited position and the defect position, it was expected that the light energy was propagated to the defect site with low loss. However, it should be mentioned that the propagation path did not go the entire surface of the plasmonic structure. This is due to external factors such as dye support and structural non-uniformity. These results support that plasmonic crystals are a very effective material as a system that propagates light with low loss and aggregates it at a specific site. These results are important design guidelines for the ultimate aggregation of light energy.

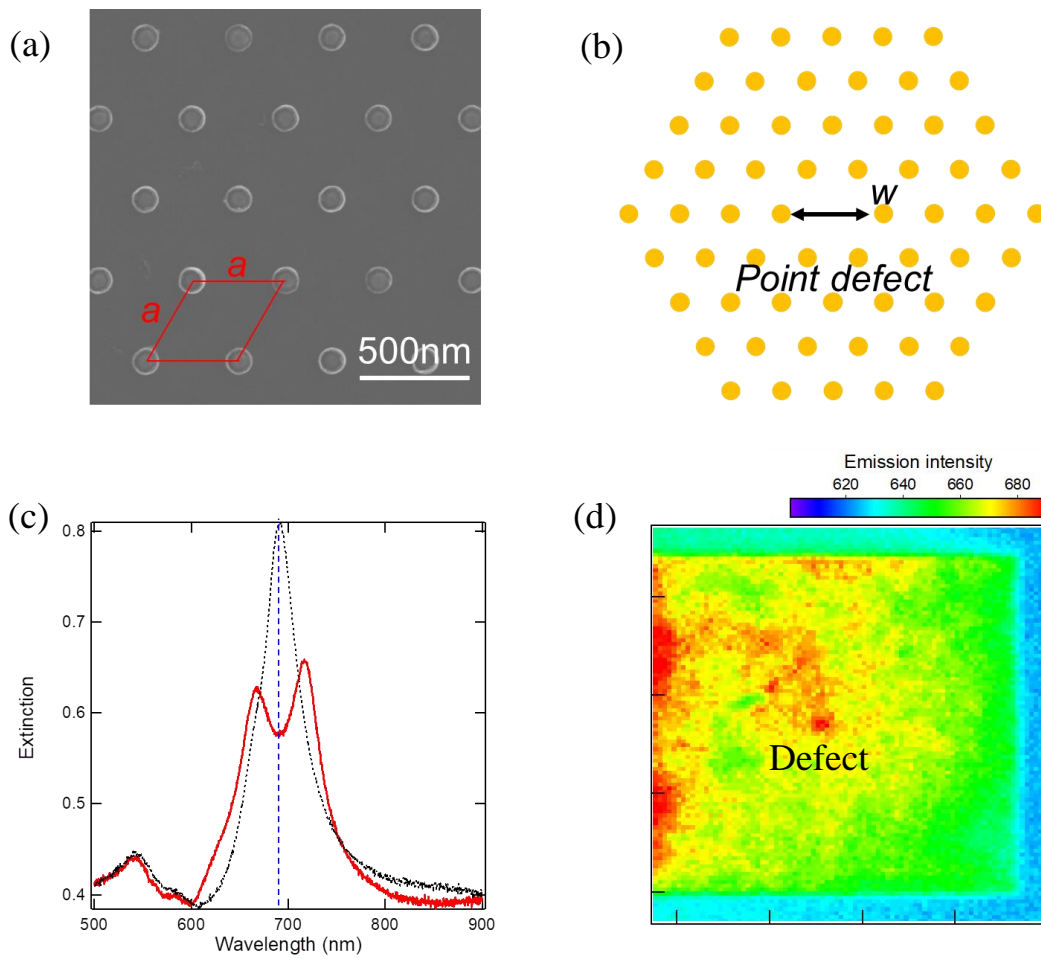


Figure 6-4. Light condensation into point defects using a hexagonal lattice structure. (a) SEM image of hexagonal Au nanodisk array with a lattice space of 425 nm. Both disk diameter and height are 100nm, respectively. In order to construct a strong coupling state, 1 mM of S0982 cyanine dye dissolved in 1,2-dichloroethane was spin-coated on the array structure. (b) As a defect, point voids with width of 690 nm which is matched to the SLR wavelength were accurately placed in the center of the structure. (c) Extinction spectra of non- and dye supported hex-Au nanodisk array. The black dashed line indicates the spectrum of bare, and blue dashed line is the absorption maximum of S0982 monomer. 128 meV of Rabi-splitting was observed in this system. (d) shows the fluorescence image of strong coupling regime.

6.4 Conclusion

For the first time, two-dimensional light propagation and effective condensation of the light energy at a defect mode were observed using plasmonic crystals. These results were achieved by the formation of the strong coupling system between dye molecules and plasmonic crystals with some defects. It has been suggested that the flow of light energy into the defect mode was achieved through a dark exciton reservoir formed by strong coupling. It has been clarified that the light trapped in the defect was likely to be a standing wave. And also, it has been confirmed that the light energy can be flowed to the defect site when a coherent wave was formed over the lattice structure when the defect width was modulated a multiple of $1/4 \lambda_{\text{SLR}}$. Since the light trapped in the defect can be stayed without decaying to lower polariton, it is possible to amplify the spontaneous emission of the S1 transition of the dye without energy modulation in high concentration. This leads to development of high-sensitivity plasmonic sensors. Furthermore, by using the hexagonal Au nanodisk arrays instead of square lattice, it was found that two-dimensional low-loss light propagation and condensation into the point defect has been successfully achieved. These results serve as design guidelines for opening the door to new photochemistry such as BEC and low-threshold polariton lasers.

6.5 References

- (308) Kravets, V. G., Schedin, F., Grigorenko, A. N. *Phys. Rev. Lett.*, **101**, 087403 (2008).
- (309) Auguié, B., Barnes, W. L. *Phys. Rev. Lett.*, **101**, 143902 (2008).
- (310) Auguié, B., Barnes, W. L. *Opt. Lett.*, **34**, 401–403 (2009).
- (311) Chu, Y., Schonbrun, E., Yang, T., Crozier, K. B. *Appl. Phys. Lett.*, **93**, 181108 (2008).
- (312) Nikitin, A. G., Kabashin, A. V., Dallaporta, H. *Opt. Express*, **20**, 27941–27952 (2012).
- (313) Vakevainen, A. I., Moerland R. J., Rekola H. T., Eskelinen A. P., Martikainen J. P, Kim D. H. and Torma P. *Nano Lett.*, **14**, 4, 1721-1727 (2014).
- (314) Lin Q. Y. and Mirkin C. A. *et al. Nano Lett.*, **15**, 7, 4699-4703 (2015).
- (315) Tsai Y. C., Lin C. F. and Chang J. W. *Opt. Rev.*, **16**, 347–350 (2009).
- (316) Mertens H., Koenderink A. F. and Polman A. *Phys. Rev. B: Condens. Matter Mater. Phys.*, **76**, 115123 (2007).
- (317) Khurgin J. B. and Sun G., *J. Opt. Soc. Am. B*, **26**, B83–B95 (2009).
- (318) Coles D. M., Somaschi N., Michetti P., Clark C., Lagoudakis P. G., Savvidis P. G. and Lidzey D. G. *Nat. Mater.*, **13**, 712–719 (2014).
- (319) Zhong X., Chervy T., Zhang L., Thomas A., George J., Genet C., James H. A. and Ebbesen T. W. *Angew. Chem.*, **129**, 9162–9166 (2017).
- (320) Georgiou K., Michetti P., Gai L., Cavazzini M., Shen Z. and Lidzey D. G. *ACS Photonics*, **5**, 258–266 (2018).
- (321) Zhou, W., Dridi, M., Suh, J. Y., Kim, C. H., Co, D. T., Wasielewski, M. R., Schatz, G. C., Odom, T. W. *Nat. Nanotechnol.*, **8**, 506–511 (2013).
- (322) Yang A., Hoang T. B., Dridi M., Deeb C., Mikkelsen M. H., Schatz G. C., Odom T. W. *Nat. Commun.*, **6**, 6939 (2015).
- (323) Zou S., Janel N., Schatz G. C. *J. Chem. Phys.*, **120**, 10871–10875 (2004).
- (324) Hutchison J. A., Schwartz T., Genet C., Devaux E. and Ebbesen T. W. *Angew. Chem., Int. Ed.*, **51**, 1592–1596 (2012).
- (325) Colombelli R., Srinivasan K., Troccoli M., Painter O., Gmachl C. F. and Tennant D. M. *Science*, **302**, 5649, 1374-1377 (2003)
- (326) Baghdouche L. K. and Cassan E. *Opt. & Quant. Elect.*, **52**, 2787 (2020)

- (327) Wang D., Wang W., Hua Y., Schaller R. D., Yang A., Schatz G. C., Odom T. W. *Nat. Nanotechnol.*, **12**, 889-894 (2017)
- (328) Cheng P. J., Huang Z. T., Li J. H., Chou B. T., Chou Y. H., Lo W. C. and Chen K. P. *ACS Photonics*, **5**, 7, 2638-2644 (2018)
- (329) Coles D.M., Michetti P., Clark C., Adawi A. M. and Lidzey D. G. *Phys. Rev. B: Condens. Matter Mater. Phys.*, **84**, 205214 (2011).
- (330) Deng H., Haug H. and Yamamoto Y. *Rev. Mod. Phys.*, **82**, 1489–1537 (2010).
- (331) Lidzey D. G., Fox A. M., Rahn M. D., Skolnick M. S., Agranovich V. M. and Walker S. *Phys. Rev. B: Condens. Matter Mater. Phys.*, **65**, 10 (2002).
- (332) Coles D. M., Michetti P., Clark C., Tsoi W. C., Adawi A. M., Kim J. S. and Lidzey D. G. *Adv. Funct. Mater.*, **21**, 3691–3696 (2011).
- (333) Yuen-Zhou J., Saikin S. K. and Menon V. M. *J. Phys. Chem. Lett.*, **9**, 6511–6516 (2018).

General Conclusions

In this paper, the noble method of light energy condensation into a very small space using the Au nanodimer structure has been achieved. In addition, the new approach enabling high efficient light propagation and concentration on the gold lattice structure were demonstrated for the first time.

In chapter 2, a facile process to improve the Q-factors of Au nanostructures fabricated by top-down lithography process was proposed. By annealing the Au nanostructures at the relatively lower temperature (i.e. lower than 200°C), it became possible to dramatically improve the Q-factor to a value equivalent to the simulated result without changing structural shape. XRD and electrochemical Cu UPD approaches revealed that small amorphous crystal islands having high-angle grain boundaries on the surface are reconstructed into low-angle grain boundaries (such as (100) and (111) planes) by annealing, resulting in improving the Q-factor due to reduced ohmic loss. Since SLR with a large Q factor provides high coherent light and a strong localized field, this method was applied to plasmonic crystals for creating a weak or strong coupling.

In chapter 3, a noble technique to control the nanoprism dimer structures within a few nanometers was achieved by combining an electrochemical approach with in situ optical measurements. The important advantage of our method is its ability to control the structure volume, leading to plasmon resonance wavelength shifts, simply by regulating the potential application time under appropriate electrochemical conditions. Furthermore, the change of the volume and gap distance can be numerically estimated from the electrochemical and optical measurements. The results obtained from both approaches correlated well with each other. This approach has been extended to sub-nanometer control of the gap. Notably, the sub-nanometer gap enabled the

realization of characteristic light scattering suppression at a specific polarization time because of the excitation of the quadrupole mode. This result supports the achievement of the ultimate light confinement that was never possible with other techniques. Since this method can maintain the quadrupole for a long time, it can be expected to have various applications of this operation such as optical manipulation of molecules.

In chapter 4, detailed investigation of the bright and dark SLR excitation conditions induced in the square lattice of Au nanodisk arrays was carried out. The Au nanodisk array, controlled by EBL and low temperature annealing, supported SLR with a high Q-factor by using a PMMA thin film layer to homogenize the surrounding environment. Variable-concentration extinction and fluorescence measurements clearly showed that dark SLR modes emerge under high concentration conditions above 50 mM and then the dark mode can access the fluorescence enhancement process. Bright mode and dark mode provide stimulated emission and were expected to be applied to the development of plasmon lasers. Furthermore, it was found that these modes are strongly dependent on the lattice spacing, and enhanced fluorescence is emitted via the dark mode in the region where the LSP does not overlap the absorption band of the fluorescent dye. These detailed studies of the dark mode excitation conditions will greatly improve the range of applications for dark mode.

In chapter 5, the formation of the strong coupling state between SLR mode of plasmonic crystals with high Q factor and S0982 cyanine dye was demonstrated. This system was modulated from strong coupling to ultra-strong coupling (USC) regime by tuning the dye concentration. The USC showed clear luminescence from the polariton level and stimulated emission at a low threshold value at the incident power of 0.4 mJcm^{-2} . The USC with a mode of two-dimensional propagating light such as SLR

would provide a large photon reservoir. The exciton reservoir in this system could transfer light energy to lattice defects. This system was applied to plasmonic crystal with defect for achieving the high efficient light concentration.

In chapter 6, two-dimensional light propagation and effective condensation of the light energy at a defect mode were observed using plasmonic crystals for the first time. The light energy flow into the defect mode was achieved through a dark exciton reservoir formed by strong coupling. This energy flow could be modulated by controlling the defect width. Furthermore, by using the hexagonal Au nanodisk arrays instead of square lattice, it was found that two-dimensional low-loss light propagation and condensation into the point defect has been successfully achieved. These results serve as design guidelines for opening the door to new photochemistry such as BEC and low-threshold polariton lasers.

From the above, I provide a novel application for light condensation. These systems can be combined, and if, for example, dimers can be introduced into defects and interacted with, it is highly expected that extreme aggregation of light will be possible. In addition, these results are important design guidelines for the development of technologies that effectively utilize light energy for the formation of strong coupling. The methodology of this research will lead to the super- photochemical reactions in the future, leading to the emergence of new optical phenomena such as energy condensation beyond the limit of the classical methods. From the results obtained in this thesis, I have proposed a unified design guideline for highly efficient collection, propagation, and use of light energy to be stored in materials.

Acknowledgement

I would like to express my sincere gratitude to Prof. Kei Murakoshi for his continuous encouragement and discussion throughout my work and student life.

I also would like to express deep acknowledgment to Prof. Tetsuya Taketsugu, Prof. Hiroki Hbazaki and Prof. Kosei Ueno for their valuable discussion and helpful suggestions.

Many thanks to Assistant Prof. Hiro Minamimoto and Assistant Prof. Tomohiro Fukushima for their lots of help and enthusiastic guidance. I want to express my deep gratitude to Assistant Prof. Keisuke Imaeda. He has been very supportive for my measurements by fluorescence measurement until late at night, without which chapter 4 and 5 could be impossible.

I would like to express my deep gratitude to Atsuyori Onuki who is a pioneer of my research. The experience, knowledge and patience provided from him has been guided my research. This study would not have been accomplished without him. I am also grateful to Alice Shibazaki and Takahiro Hayashi. My research was done with them. Thanks to their help and advice, experimental system and my work were improved. am grateful to Rumi Akiyama, Mariko Yonezawa and Junko Hattori who are secretaries in my Lab. for their lots of dedicated support. I am also grateful to all the colleagues of the Laboratory of Material Chemistry and the Laboratory of Physical Chemistry, Department of Chemistry, Graduate School of Science, Hokkaido University, for their indispensable comments and for giving me cheerful and productive life in the Lab.

Finally, I would like to express my greatest gratitude to my parents, my sisters and my wife for their hearty support and encouragement throughout these years, without which I would not be able to achieve this work.